NEGATIVE ENRICHMENT OF CIRCULATING TUMOR CELLS VIA 3D PRINTED MICROFLUIDIC DEVICE

A Dissertation
Presented to
The Academic Faculty

by

Chia-Heng Chu

In Partial Fulfillment
of the Requirements for the Degree
Ph. D. in the
School of Electrical and Computer Engineering

Georgia Institute of Technology
August 2021

NEGATIVE ENRICHMENT OF CIRCULATING TUMOR CELLS VIA 3D PRINTED MICROFLUIDIC DEVICE

Approved by:

Dr. A. Fatih Sarioglu, Advisor
School of Electrical and Computer Engineering
Georgia Institute of Technology

Dr. John F. McDonald
School of Biological Sciences
Georgia Institute of Technology

Dr. Albert B. Frazier
School of Electrical and Computer Engineering
Georgia Institute of Technology

Dr. F. Levent Degertekin
School of Electrical and Computer Engineering
Georgia Institute of Technology

Dr. Stanislav Emelianov
School of Electrical and Computer Engineering
Georgia Institute of Technology

Date Approved: [July 13, 2021]

To me

&

my beloved family

ACKNOWLEDGEMENTS

Throughout my Ph. D. journey, I have encountered many people who supported me during my ups and downs and inspired me in many different ways. I would like to thank them for helping me succeed in my Ph. D. journey.

First, I would like to thank my advisor, Prof. A. Fatih Sarioglu, for his guidance and support. He never doubted my ability to complete the projects and fought with me through all the challenges that I faced. I treasure these life lessons that I have learned from him.

Second, I would like to thank all my colleagues and friends for all the fun we have had together, and for all the nights we spent in the lab. Their continuous mento-support allowed me to fight through hard times and kept me moving forward in my journey.

Lastly, I would like to thank my family for their full supports and their encouragement throughout my Ph. D. Their love is what gave me the strength to continue moving forward and finishing my Ph. D. journey.

TABLE OF CONTENTS

LIST OF TABLES

LIST OF FIGURES

LIST OF SYMBOLS AND ABBREVIATIONS

CAD	Computer-aided design
CBC	Complete blood count
CEA	Contraction-expansion array
CK	Cytokeratin
CTC	Circulating tumor cell
CTM	Circulating tumor microemboli
DAPI	4,6-diamidino-2-phenylindole
DI	Deionized
DLD	Deterministic lateral displacement
DMEM	Dulbecco's Modified Eagle's medium
DMSO	Dimethyl sulfoxide
DRIE	Deep reactive-ion etching
EDTA	Ethylenediaminetetraacetic acid
EGFR	Epidermal growth factor receptor
EMT	Epithelial-mesenchymal transition
EpCAM	Epithelial cell adhesion molecule
FBS	Fetal bovine serum
FDA	U.S. Food and Drug Administration
FITC	Fluorescein isothiocyanate
FTIR	Fourier-transform infrared spectroscopy
GMBS	N-y-maleimidobutyryloxy succinimide ester
HB	Herringbone

HTMSU	High-throughput micro sampling unit
IDT	Interdigitated transducer
IRB	Institutional Review Board
MACS	Magnetic activated cell sorting
MPTMS	3-mercaptopropyl-trimethoxysilane
PBS	Phosphate buffered saline
PDMS	Polydimethylsiloxane
PFA	Paraformaldehyde
RBC	Red blood cell
RIE	Reactive ion etching
SEM	Scanning electron microscope
STL	Stereolithography
taSSAW	Tilted-angle standing surface acoustic wave
WBC	White blood cell
XPS	X-ray photoelectron spectroscopy

SUMMARY

Circulating tumor cells (CTCs) are cells that detach from the primary tumor inside the cancer patient's body to circulate in the bloodstream and cause the metastasis of the cancer. Routine and reliable isolation of CTCs from peripheral blood would both allow effective monitoring of the disease burden and guide the development of personalized treatments for cancer patients. Negative enrichment of CTCs by depleting normal blood cells from patient samples not only ensures against a biased selection of a subpopulation but also allows the assay to be used on patients with different tumor types. In my doctoral thesis, I developed an additively manufactured microfluidic device that can negatively enrich viable CTCs from clinically-relevant volumes of unmanipulated whole blood samples. The microfluidic device depletes nucleated blood cells based on their surface antigens and the smaller anucleated cells based on their size contrast with the tumor cells. Also, enriched CTCs are made available off the device in a suspension making our technique compatible with standard immunocytochemical, molecular and functional assays. The densely micropatterned 3D device could deplete >99.5% of white blood cells from 10 mL of unmanipulated whole blood while recovering >90% of spiked tumor cells. I also demonstrated the clinical utility of the device by isolating CTCs from blood samples collected from patients with prostate and pancreatic cancers. This creates a universal CTC assay that can differentiate tumor cells from normal blood cells with the specificity of clinically established membrane antigens yet with no labels on the sample offers the potential to enable routine screening of blood samples for tumor load at the point-of-care.

CHAPTER 1. INTRODUCTION

Cancer, one of the leading causes of death worldwide, has been a persistent major health problem in our society [1]. According to the American Cancer Society, there will be more than 1.8 million new cases of cancer throughout 2021 in the United States, out of which an estimated 600,000 are expected to die as a result [2]. A major factor that makes cancer so deadly is metastasis, which accounts for more than 90% of cancer-related deaths [3]. Cancer first develops when the body fails to kill old or abnormal cells inside the body, which are then allowed to divide and grow uncontrollably, resulting in the development of a tumor [4]. Metastasis occurs when cancerous cells break away from the primary tumor and circulate in the body via the bloodstream or lymph to form new tumors in other parts of the body. These cells that leave the primary tumor and eventually cause the formation of secondary distal tumors are known as the circulating tumor cells [5].

1.1 Circulating Tumor Cells

Circulating tumor cells (CTCs) are tumor cells that depart from a primary tumor lesion in a cancer patient's body and travel through the bloodstream to a secondary part of the body, where they are then seeded and continue growing. This 'seed and soil' concept of metastases was first observed by Thomas Ashworth [6] back in 1869. He first observed CTCs in the blood sample of a metastatic cancer patient. At the time of his observation, he found cancer cells similar to the cancer tumor from the patient in the blood sample, which led him to hypothesize and conclude that multiple tumors can exist in the patient's body. He also noted that if CTCs in the blood came from the primary tumor in the patient's body, they must have passed through the essential components of the human cardiovascular

system to arrest at the internal saphenous vein. This theory was later studied by Paget [7] and recently revisited and reconfirmed by Fidler [8]. Today, CTCs are believed to provide valuable information in cancer biology [9], [10], such as cancer diagnosis and prognosis [11], stages of the diseases [12], and treatment effectiveness evaluation [13]. Reliable isolation and analysis of circulating tumor cells (CTCs) from blood samples of cancer patients present an opportunity not only for clinical management of the disease [14], [15] but also for understanding the biology of the metastatic process at the cellular and molecular level [5]. While CTCs hold the promise for non-surgical, minimally invasive tumor biopsies as well as personalized drug therapies optimized on patients' tumor cells [16]-[18], their practical isolation from peripheral blood remains a challenge.

1.2 Challenges in CTC Isolation

1.2.1 Rarity of CTCs

One of the main challenges in the isolation of CTC from blood samples is the scarcity of CTCs [19]. Typically, in a 1 mL volume of blood sample, there are millions of white blood cells (WBCs), billions of red blood cells (RBCs), but only 1 to 10 CTCs [20], [21]. This makes the identification and the isolation of CTCs from blood samples very difficult. Various laboratory techniques, including size-based separation [22], [23], density gradient centrifugation [24], scanning cytometry [25], and magnetophoretic separation [26], have been applied to differentiate CTCs from hematological cells based on the contrast in their physical and chemical properties. In fact, the U.S. Food and Drug Administration (FDA) approved the clinical use of CellSearch®, which employs immunomagnetic labeling of CTCs against the epithelial cell adhesion molecule

(EpCAM), an epithelial marker that is not expressed by normal blood cells [27]. While these batch processes typically utilize existing laboratory instrumentation and involve commonplace sample preparation protocols, they may not be ideally suited for the detection of CTCs because of the fact that they inherently rely on stochastic processes for CTC detection and use multi-step protocols, which reduces the sensitivity required to detect rare CTCs [28].

In order to increase the sensitivity and the specificity of the detection, microfabrication techniques that have been used in the past decades for the development of computer chips with micro and nanoscale precision were implemented to fabricate microchannels and microfeatures for the deterministic screening of the cells [29]. These devices are known as microfluidic devices. Microfluidic devices are often fabricated by first using conventional photolithography techniques to create the desired microchannel structures, then using soft lithography molding to transfer the structure into a polymer that is later bonded with a glass slide to create the final device [30]. This fabrication process allows easy iteration and optimization of the device. The microchannel template created by the photolithography technique can also be reused many times for the fast reproduction of the device. Microfluidic CTC isolation techniques offer distinct advantages over batch processes as they do not reply on stochastic processes for CTC detection and can be engineered to deterministically screen a blood sample in a controlled microenvironment with higher sensitivity and specificity [31]. In addition, the ability of microfluidic platforms to utilize various modalities for cell discrimination allows biophysical [32]-[34] or biochemical [35], [36] isolation strategies, some of which do not have macroscale analogs.

Recently, 3D-printing that converts computer-aided model designs directly into physical objects using a large selection of materials with a simple click-and-print process has also become a popular method for the fabrication of microfluidic devices [37]. Current state-of-the-art commercial 3D-printers are capable of producing features in the micrometer range, making them suitable for the rapid development of 3D microchips [38]. The use of 3D-printing technology in microfluidics not only provides a fabless alternative to creating 2D master templates, but also allows effortless realization of 2.5D templates to be used for creating microfluidic channels of varying height profiles with soft lithography [39], [40]. Furthermore, 3D-printing can also be used to directly print microfluidic devices [41]. Although the minimum feature size that could currently be achieved with 3D-printing cannot yet match that of photolithography [42], 3D-printed microfluidic devices hold several advantages over conventional microfluidic devices fabricated with soft lithography [43]. First, 3D-printing microfluidic devices allow the creation of channels and structures with geometries more complex than those possible using conventional soft-lithography [44]. Second, available materials with which to manufacture the device include a wide range of photocurable polymers. Third, the single-step fabrication process offers rapid prototyping of microfluidic devices, which accelerates iterations to optimize the device for desired functionality. Although 3D-printed microfluidic devices have many advantages over conventional microfluidic devices, the need to remove the sacrificial materials that were printed in place of the microchannels as a place holder during the printing process prevents the device to be used directly. An efficient method for the removal of sacrificial materials needs to be developed in order to develop 3D-printed microfluidic devices for the enrichment of CTCs.

1.2.2 Heterogeneity of CTCs

Among the strategies used in microfluidic devices for the detection of CTCs, immunoaffinity-based discrimination of CTCs [45], [46] is the most common and arguably the most relevant in terms of clinical assessment of tumor cells. Microfluidic platforms are routinely used to isolate EpCAM-positive CTCs either through functionalized surfaces [47], [48] or through immunomagnetic labeling [49]. While the combination of the sensitivity of microfluidics with the specificity of antigen-antibody interaction is highly effective, antigen-dependent capture of CTCs leads to a biased population and fails to accommodate heterogeneity among tumor cells and dynamic cell expression due to epithelial to mesenchymal transition [50], [51].

A more inclusive approach for enriching CTCs from blood samples is to target the normal blood cells, which are well characterized and, more importantly, show more consistent traits among different samples or subjects. This enrichment approach is known as the negative enrichment method and it is advantageous not only because it leads to an unbiased detection of CTCs but also produces intact tumor cells free of attached immuno-agents, eliminating potential artifacts in downstream studies [52]-[55]. In this process, WBCs are typically immunolabeled with antibody-functionalized magnetic beads and pulled away from the sample in downstream under a magnetic field gradient [35], [36], [56], [57]. This not only requires pre-labeling of the blood sample but is also prone to introducing unwanted magnetic beads in the enriched product. The other approach is to capture WBCs out of the sample through immunoaffinity in a device functionalized with antibodies against WBC markers [58], [59]. While it potentially offers label-free capturing of WBCs, this approach suffers from several technological hurdles. First, label-free

microfluidic devices for leukocyte depletion are currently not practical for processing clinical samples because the limited surface area of a typical antibody-functionalized microfluidic device is quickly saturated by captured leukocytes. Second, sample preparation such as pre-lysing of the red blood cells (RBCs) is typically required to remove the RBCs from the collected blood sample, but this process drastically increases the sample volume through dilution and is also prone to losing valuable tumor cells during sample manipulation [60].

1.3 Thesis Contributions

In my doctoral research, I addressed the difficulties in fabricating monolithic 3D-printed microfluidic devices as well as the aforementioned shortcomings of immunoaffinity-based negative enrichment of CTCs by developing an effective method to remove the sacrificial materials from the fully enclosed 3D-printed microchannels and creating a 3D microfluidic device that can process clinically relevant volumes of unmanipulated whole blood directly for the label-free enrichment of CTCs from cancer patients' blood samples. There are three major contributions of my thesis:

First, in order to fabricate monolithic 3D-printed microfluidic devices, I developed the centrifugal sacrificial material removal method to efficiently and effectively remove the sacrificial materials from the 3D-printed microfluidic devices. I have demonstrated the applicability of this approach on devices fabricated using different printing techniques as well as demonstrated its advantages over the already developed injection-based sacrificial material removal method. By using the method that I have developed, I was able to fabricate the 3D-printed microfluidic device for the enrichment of the CTCs.

Second, with the centrifugal sacrificial material removal method, I developed a hybrid monolithic 3D-printed microfluidic device with stacked layers of immunodepletion channels followed by a microfiltration section to deplete pre-labeled WBCs from whole blood and retrieve the tumor cells, respectively. The immunodepletion channels provide sufficient area for the depletion of WBCs from clinically relevant volumes of whole blood. To eliminate the need for the sample preparation step for lysing RBCs, the device is integrated with a membrane micropore filter downstream of the immunodepletion stage. The membrane filter is used to retain all nucleated cells (tumor cells and potential WBCs that eluded immunocapture) in the immunodepleted sample and dispose of RBCs and platelets. I also demonstrated the clinical feasibility of this device by isolating prostate cancer CTCs directly from a 10 mL patient blood sample.

Finally, to achieve label-free enrichment of the CTCs, I labeled the 3D-printed device with WBC specific antibody for the capturing of WBCs directly from unmanipulated whole blood samples. Also, to increase the capturing of WBCs, I introduced a second-stage depletion of WBC by using an immuno-enhanced membrane filter. The filter selectively retains the uncaptured WBCs that escaped the immunodepletion channels chemically on its surface and allows for the mechanically held CTCs to be released and negatively enriched under a reverse flow. The enriched viable and label-free CTCs were recollected in a liquid suspension which is suitable for further downstream assays. To demonstrate the feasibility of the device for clinical studies, I processed multiple prostate and pancreatic patient samples and was able to observe enriched CTCs in the final product.

CHAPTER 2. LITERATURE REVIEW

Circulating tumor cells are believed to hold valuable information related to the cancer tumor inside the cancer patient's body [9], [10], such as cancer prognosis [11], stages of the diseases [12], and treatment effectiveness evaluation [13]. The development of new technologies with high sensitivity, specificity, and purity for CTC enrichment and isolation from the blood sample allows scientists to perform direct analysis on the pure population of CTCs. CTC enrichment methods with high purity allow the downstream analysis of the CTC to obtain noise-free results. The enrichment of CTC also permits for either DNA and RNA extraction [61] or live cell analysis and diagnosis [62] of the CTCs. These can provide valuable data and information to not only better understand the cancer progression in the patient's body and improve prediction and pharmacodynamics of the tumor reaction to the treatment but also develop specialized treatment and personalized therapy for each cancer patient [63].

Currently, there exist several technological challenges in the detection of CTCs from clinical samples. CTCs usually are mixed with normal blood cells in a blood sample. The technologies design for CTC detection and isolation need to differentiate the CTC from the other peripheral blood cells that exist in the blood sample while being compatible with the downstream assays. Due to the heterogeneity of CTCs, it is difficult to target the CTCs directly since there does not exist a single surface marker that allows the researchers to universally identify the CTCs from a patient's blood sample [64]. Also, studies have found that even within the same cancer patient, the biomarkers express on the CTCs can be very different from one another [65]. These mark the importance of designing CTC enrichment technology with high specificity to avoid impurity in the enriched product as well as false detection of CTCs. Another challenge faced by the CTC enrichment technologies is the rarity of the CTCs present in the blood sample. There are millions and

billions of WBCs and RBCs in each milliliter of blood, but only approximately 1-10 CTCs [66], [67]. Due to this reason, CTC enrichment technologies are required to have high sensitivity for reliable enrichment. This is even more important for CTC enrichment technologies that are designed for early-stage cancer detection since even fewer CTCs are presented in the blood sample [68]. Therefore, CTC enrichment technologies with high specificity and sensitivity are required to overcome these technological challenges.

2.1 Batch Enrichment Approaches

Despite the technological challenges faced by the development of CTC enrichment technology, the benefit and potential of the CTCs lead to active research that focuses on the detection of CTCs from clinical samples [69]. In the early 1950s and 1960s, scientists had first tried to attack these challenges by utilizing the technique of density gradient centrifugation, where the cells are separated by centrifugal forces. Under centrifugation, cells will be divided into different layers based on their sedimentation coefficient, which is related to the size and density of the cell according to the Stokes law of sedimentation. Since each type of cell expresses similar physical properties, they will result in similar vertical positions in the medium after the centrifugation. Fawcett et al. [70] were the first to demonstrate this centrifugal batch enrichment process by using albumin as the medium to separate malignant tumor cells from the erythrocytes and leukocytes. However, this method was not widely used by others due to the cost and complexity of preparation for albumin. Later, Seal [71] utilized the silicon blending oil as the medium and was able to observe CTCs in 53% (25 out of 47) of the gastrointestinal tract cancer patients tested. Although the percentage of detection is not in favor of clinical usage, these studies open up the great possibilities of centrifugation technique which eventually lead to the development of Percoll and Ficoll-Paque density centrifugation media. These media are commonly used in the clinical process and research to isolate mononuclear cells in biological research labs and hospitals today [72], [73], but the low sensitivity and purity of

the enriched CTCs still prevent this batch process from being used wildly for direct researches and studies of the CTC.

2.2 Microfluidic Approaches

With the advancement of micro and nanofabrication techniques, microfluidic systems became the leading technology for CTC enrichment due to their low cost and portability over conventional batch techniques [74]. In addition, microfluidic CTC detection approaches allow deterministic interrogation of individual blood cells through precisely manufactured features and can often utilize localized force fields to achieve higher sensitivity and specificity [75], [76]. Many groups have successfully developed numerous technologies to obtain a high CTC enrichment ratio and purity with high throughput directly from clinical blood samples. These groups designed microfluidic devices that discriminate CTCs from blood cells by exploiting the biophysical and biochemical contrast between tumor and normal blood cells. Some simultaneously utilized a combination of physical and chemical modalities for discrimination [77]-[82]. In the following sections, numerous CTC enrichment technologies will be divided into subcategories and discussed in detail. In the biophysical-based isolation, microfiltration, hydrodynamic, acoustophoresis, dielectrophoresis-based techniques, and devices that are explicitly targeting CTC clusters will be discussed. In the biochemical-based enrichment methods, immunoaffinity approaches will be discussed as well as methods using aptamer and peptides. Lastly, technologies that incorporate the use of a combination of the techniques listed above will also be addressed.

2.2.1 Biophysical Based Approaches

The biophysical differentiations between normal blood cells and CTCs are useful biomarkers for identifying CTCs in a blood sample. Their innate contrasts between cell

size, density, deformability, and other biophysical properties have led to the development of many different label-free CTC enrichment technologies.

2.2.1.1 Microfiltration-Based Enrichment Techniques

Out of all the biophysical-based methods, the filtration-based technique has been the most common way to differentiate CTCs from the residual blood cells. ISET® (Isolation by Size of Epithelial Tumor cells) (Rarecell, Paris, France), a commercially available product, uses track-etched polycarbonate membranes for the enrichment of fixed CTCs based on their cell size [22]. It utilizes 8 μm diameter pores to directly process 10 mL of blood sample diluted with a ratio of 1:10 without any clogging. Based on its operational pressure, it has demonstrated the feasibility of enriching intact CTCs, but its low specificity prevents it from being used for clinical practices. ScreenCell® filtration device (ScreenCell, Paris, France), which is another system similar to ISET®, uses track-etched membranes with smaller pore size than ISET®, specifically 6.5 and 7.5 μm, for the enrichment of both live and fixed tumor cells [83]. There are three different types of devices: ScreenCell® Cyto, ScreenCell® CC, and ScreenCell® MB. ScreenCell® Cyto is specifically designed for the use of isolating fixed cells for cytological studies, while ScreenCell® CC and ScreenCell® MB are used for isolating live cells for either cell culturing or molecular biology studies, respectively. The advantages of the ScreenCell® systems include low-cost and simple to operate, and it has been demonstrated to enrich CTCs from lung cancer patients [84]. This proved its potential for the use of lung cancer diagnostic testing, but similar to ISET®, it suffers from low purity and specificity, leading to high background noise from the peripheral blood cells.

Aside from the track-etched membrane filters that have pores randomly distributed over the surface, microfabricated membrane filters with periodic pores have also been developed. CellSieve™ (Creatv MicroTech) [85], a 9 mm diameter micropatterned membrane filter that contains periodic and uniformly distributed 7 μm diameter pores with more than 100,000 pores, was used in comparison to the track-etched membrane filter for the enrichment of CTCs. Adams et al. prepared simulated blood samples by spiking known amounts of MCF-7 breast cancer cells into 7.5 mL whole blood for the testing. The results showed that the CellSieve™ membrane filter had a better performance than the track-etched membrane filters. Both fixed and unfixed cells were tested, and the CellSieve™ membrane filter was able to achieve 25-35% higher capture efficiencies than the commercial track-etched membrane filter while improving the purity of the enrichment by approximately ten-fold, which significantly reduces the background contamination.

Disregarding the low-cost and disposable membrane filters made available commercially; researchers are actively developing specialized membrane filters for the enrichment of CTCs from blood samples. In order to fabricate membrane filters with high pore size accuracy, uniform pore density, and great biocompatibility, a parylene membrane with pores etched by the reactive ion etching (RIE) system was developed by Zheng et al. [86]. The parylene membrane filter was designed in a square shape with dimensions of 1 cm by 1 cm. The pores were 10 μm in diameter with 33% duty cycles. Based on the reported results, the parylene membrane filter was able to positively identify CTCs from 51 out of the 57 patient samples tested with recovery rates greater than 90%. Zheng et al. also compared the results with the only Food and Drug Administration (FDA) approved system for monitoring CTCs in metastatic patients, CellSearch® [87]. Although the results showed

that the parylene membrane filters have a higher sensitivity in detecting CTCs than the CellSearch® system, several technical challenges prevented it from being used for clinical applications. The autofluorescence from the parylene material made the identification of the CTCs very difficult under the microscope [88], and the need for fixation of the cells makes the enriched CTCs incompatible with further downstream analysis. They overcame some of these challenges in 2014 by developing a 3D membrane microfilter that enriched viable CTCs [89]. The design includes two parylene filters, a top layer with 40 μm pores that aligns with the 8 μm pores on the bottom layer. The enriched cells are held in the 10 μm gap between these two filters. This design significantly reduces the mechanical stress expressed on the cells during the filtration process and allows viable cells to be captured. MCF-7 and MDA-MB-231 breast cancer cell lines were used to test the capture efficiency of the 3D membrane filter, and as a result, 83% and 78% of the spiked cancer cells were captured, respectively. Furthermore, greater than 70% of cell viability was reported for the spiked cancer cells after the filtration.

Apart from the standard membrane filtration systems used with commercial filter holders, micropore filters embedded in microfluidic devices have also been developed for the enrichment of CTCs. Such as the crescent-shaped arrays device designed by Tan et al. that can achieve more than 80% recovery rate of the spiked cancer cells with no pre-labeling of the cells [90]. The device is fabricated with the standard soft lithography process to form the microchannels and microfeatures on the polydimethylsiloxane (PDMS) [91], a commonly used material for microfluidic device fabrication with excellent biocompatibility and transparency, and later bonded with a glass slide using oxygen plasma to seal the channels. The mechanism of the device is based on the size and deformability

differences between the CTCs and normal blood cells to capture the CTCs on the crescent-shaped arrays. The captured CTCs can then be released from the microtraps with a reverse flow. Under the optimized operational conditions for the device, it was able to recover 95-97% of the spiked cancer cells while having minimal effect on their viabilities. More importantly, the device achieved more than 80% purity of the isolated CTCs, which was a major challenge faced by filtration-based technologies. Another challenge faced by filtration-based technology was clogging the filter or the device by a large number of cells present in the blood sample. This was addressed by Yoon et al. with the clog-free CTC isolation microfluidic chip [92]. The device utilized a piezoelectric actuator to introduce continuous fluid oscillation for displacing the cells trapped on the filter. This allows smaller cells trapped on the filter to pass through and eliminates the clogging of the filter. After processing the blood sample, a reverse flow can be applied to release the captured CTCs. They first tested the device using microbeads with 20 μm and 5 μm to represent the CTCs and red blood cells. The results showed that they were able to separate the mixed particles with 100% efficiency and 100% purity. They then demonstrated the workability of the device with blood sample by using simulated blood sample with spiked MDA-MB-231 and showed the filter was free of clogging issue.

Microfiltration techniques have been an attractive choice for CTC enrichment due to their low-cost, simple to use, simple processing, and high-throughput advantages, but the lack of specificity due to size-overlap between CTCs and normal blood cells, specifically WBCs, commonly resulting in high contamination in the enriched product by the normal blood cells [93], [94]. Furthermore, due to the large number of cells presenting

in a clinically relevant volume of blood sample, clogging of the device often occurred during the processing of the sample [95], [96].

2.2.1.2 Hydrodynamic Force-Based Enrichment Techniques

Apart from microfiltration-based enrichment techniques, another technique that utilized the differences of the biophysical properties between CTCs and normal blood cells is the hydrodynamic force-based enrichment technique. Since microchannels are in the scale of micrometers, their flow lies within the laminar flow region with low Reynold's number and steady streamlines that flow parallel to one another without mixing [97]. With this unique property, microfluidic devices such as deterministic lateral displacement (DLD) devices can be employed to separate cells based on their sizes [98]-[100]. DLD devices utilize periodic micropillar arrays that shift from row to row and direct cells larger than the critical diameter to one side while letting the smaller cells to flow through undeflected. The continuous flow process of DLD and the relatively large gaps between the pillars prevent cells from clogging the devices [92]. Loutherback et al. developed a DLD device that could discriminate CTCs from the other blood cells [101]. The device was designed with a critical diameter of 15 μm [102] which is larger than most of the peripheral blood cells and was able to successfully isolate CTCs that are larger than 15 μm. DLD has also been used to isolate of suspended particles that range from the nanometer to the micrometer scales with high isolation efficiency [103], [104]. This demonstrated that the DLD technique offers high precision and effectiveness in isolating particles or cells of different sizes. Furthermore, Loutherback et al. investigated the effect of the geometry of the pillars on the isolation efficiency and found that triangular pillars are more effective in CTC isolation [105]. The results showed that the device was able to recover 86% of the

spiked cancer cells from the diluted blood sample with an operational flow rate of 10 mL/min [102]. Although the advantage of being able to process samples under high throughput while being able to discriminate cells based on their sizes precisely make DLD a promising technique for clinical studies of CTCs, similar to the microfiltration techniques, DLD is prone to losing CTCs with cell sizes identical to that of the normal blood cells.

Another method that enriches CTCs based on the biophysical properties of cells is called the inertial focusing technique. In the 1960s, Segre and Silberberg first observed the inertial focusing effect from the 1 mm diameter particles suspended in a 1 cm diameter tube. They found that while the particles flow through the tube, they would move toward the sidewall of the tube and form into a ring [106], [107]. This effect was later known as the inertial effects [108], [109]. Based on this effect, the contraction-expansion array (CEA) microfluidic device was developed by Lee et al. for the separation of CTCs from the normal blood cells. The device is designed with contraction and expansion regions to utilize both inertial lift force and Dean drag force for the separation of the cells [110]-[112]. The balancing position of these two forces on a cell in a microfluidic channel is greatly dependent on the size of the cell. Cells with larger diameters are more affected by the inertial lift force, pushing them to move toward the inner sidewall. On the other hand, cells with smaller diameters are more affected by the Dean drag force and are pushed toward the outer sidewalls. Therefore, cells with different sizes would result in different lateral positions in a microchannel and be separated from one another [113]. Another important parameter that critically affects the balancing of these two forces is the operational flow rate. Inertial forces are negligible under low flow rates and dominate over Dean drag forces

under high flow rates, making it critical to perform the cell separation with proper flow rate to achieve the optimal separation results. With an optimized flow rate of ~1×10^8 cells/min, Lee et al. demonstrated the device was able to enrich CTCs directly from whole blood samples with an average recovery rate of 99.1% while rejecting 88.8% of the normal blood cells at the same time [112]. To further improve the rejection rate of normal blood cells, it was shown that by connecting two CEA chips in series, the rejection rate of the normal blood cells can be increased to 97.4%.

Vortex trapping is another biophysical-based enrichment technique that exploits the hydrodynamic effects in the enrichment of CTCs [114]. The devices are designed with specific geometries that form microvortices within the microchannels to trap the target cells. Sollier et al. introduced the Vortex Chip that consists of multiple expansion regions to generate microvortices in those regions for the trapping of CTCs [115], where Moffatt et al. also provided the theoretical formulas related to the generation of these microvortices [116], [117]. Before introducing cells to the expansion regions, the Vortex Chip focuses the cells with different sizes into their equilibrium lateral positions by designing a long channel in between the inlet and the expansion regions. In the long channel, the cells experience two different forces, the shear-gradient lift force that pushes the cells toward the sidewall of the microchannel and the wall effect lift force that drives the cells toward the center of the microfluidic channel [118]. These two forces will determine the lateral position of the cell in the channel, with larger cells closer to the sidewall and smaller cells in the centerline. Since most of the CTCs are larger than the normal blood cells, the CTCs will be directed toward the sidewalls in the long channel while the normal blood cells will be pushed to the centerline. When the cells arrive at the expansion regions, the CTCs are

trapped by the microvortices in the expansion regions. At the same time, the normal blood cells stay on the centerline of the channel and flow pass the expansion regions. After rinsing the device with PBS to remove the residual blood cells in the channel, the trapped CTCs can then be retrieved from the device by reducing the flow rate. By processing diluted blood samples with spiked cancer cells, Sollier et al. demonstrated that the Vortex Chip was able to recover 20.7% of the spiked cancer cells while achieving 89% purity with minimal effect on cell viability. Furthermore, cancer patients' blood samples were also tested, and the Vortex Chip was able to successfully recover CTCs from the tested samples with purity ranging from 57% to 95%.

Although hydrodynamic-based enrichment techniques overcome the clogging issue faced by the microfiltration techniques while preserving high-throughput and label-free advantages, size overlaps between CTCs and normal blood cells can still introduce impurity in the enriched product. Also, hydrodynamic-based enrichment techniques require iteration and optimization of the device geometry and precision control over the sample flow rate for the effective enrichment of CTCs.

2.2.1.3 Acoustophoresis-Based Enrichment Techniques

Acoustophoresis-based CTC enrichment is another hydrodynamic-based enrichment method. It utilizes acoustic waves for the separation of CTCs from normal blood cells without the need of pre-labeling and maintains cell viability at the same time. In acoustophoresis-based enrichment devices, transducers are used to generate the acoustic pressure waves that separate the cells [119]. The nodes and anti-nodes of a standing acoustic wave act as the minimum and maximum pressure oscillations in the microfluidic

channel. These pressure oscillations then induce forces on cells proportional to their size and generate movements where the direction of the movement is determined by the density and compressibility of the cells compared to the medium. For cells with positive contrast factors, the force will direct them toward the nodes of the standing acoustic wave. On the other hand, cells that have negative contrast factors will be directed toward the anti-nodes of the standing acoustic wave. Therefore, when enriching CTCs using the acoustophoresis method, cells can be separated by either the direction or pace of the movement.

To demonstrate the effectiveness of separating CTCs from normal blood cells using the acoustophoresis-based enrichment method, Antfolk et al. developed a microfluidic device based on this principle [120]. The device consists of two separate channels, and each of them is operated by an individual piezoelectric transducer. For the pre-alignment channel, 4.530 MHZ acoustic pressure waves are used to focus the cells to the sidewalls of the channel so that cells are in the same lateral position in the channel before entering the second channel, the cell separation channel. In the second channel, 2.001 MHz acoustic pressure waves laterally shift the CTCs from the other blood cells, separating and moving them toward the center pressure node. By processing an RBC-lysed spiked blood sample, Antfolk et al. reported a recovery rate of 86.5% of the spiked prostate cancer cells with 1.1% impurity. Antfolk et al. also reported that the recovery rate of the spiked cancer cells could be further improved to 94.8% by increasing the intensity of the acoustic field, but it also results in a higher impurity rate of 2.2%.

Although many other groups have also demonstrated the feasibility of enriching CTCs from normal blood cells using the acoustophoresis method [120]-[122], this technique faces the challenges of low throughput and fluctuation under long-term

operation, which prevent it from being used for clinical studies. To overcome these barriers, the tilted-angle standing surface acoustic waves (taSSAW) device was introduced by Li et al. in 2015 [123], where they successfully demonstrated the used of the acoustophoresis method to enrich CTCs from breast cancer patients' blood samples. In the taSSAW device, nodes and anti-nodes from the acoustic pressure waves are generated diagonally by the tilted interdigitated transducers (IDTs) implemented on the device, which helps move the cells laterally in the microchannel. The reported results showed that by processing RBC-lysed spiked blood samples through the device, they achieved recovery rates ranging from 83-87% across different cancer cell lines under the operational flow rate of 1.2 mL/h, which is comparable to the flow rates of other microfluidic enrichment techniques. Moreover, they were able to recover 59, 8, and 1 CTCs from the three breast cancer patients' blood samples tested, demonstrating the feasibility of using the taSSAW device under clinical settings.

Although acoustophoresis-based CTC enrichment techniques have the advantages of label-free isolation and cell viability preservation, the low throughput of the techniques place a barrier in using the devices to process clinically relevant volume of blood samples.

2.2.1.4 CTC-Cluster Enrichment Techniques

Circulating tumor cells can also circulate and metastasize in the form of clusters known as the circulating tumor cell clusters or circulating tumor microemboli (CTM). Only about 2-5% of all CTCs circulating in the bloodstreams of a cancer patient are CTC-clusters, making them very scarce, but at the same time, they exhibit 23 to 50 times greater metastatic propensity than single CTCs [124], [125]. This shows that CTC-clusters can be

used as another indicator for monitoring the disease as well as the effectiveness of the cancer treatment [126], [127]. Although some of the CTC enrichment technologies have reported the finding of CTC-clusters using their devices, the lack of the specific design for CTC-clusters enrichment yield a low sensitivity and specificity for using those devices to enrich CTC-clusters [128]-[130]. Furthermore, dissociation of the CTC-clusters can occur in the devices with high shear forces; therefore, it is essential to develop devices that specifically target the CTC-clusters to enrich intact CTC-clusters effectively and efficiently.

Sarioglu et al. developed the first CTC-clusters enrichment device, Cluster-Chip, that was able to enrich label-free CTC clusters based on their unique biophysical properties directly from whole blood samples [34]. The chip captures the CTC-clusters based on their geometries and cell-to-cell junction strength, allowing the device to be used for the enrichment of CTC-clusters from all types of metastatic cancer. The capture mechanism of the device consists of a group of three triangular micropillars, where two of the triangular pillars create a funnel shape that focuses the CTC-cluster into a precisely designed 12 μm gap in between those pillars and the third triangular pillar bifurcates the gap in the middle that creates two equivalent laminar flow paths along its sides. The two laminar flow paths allow normal blood cells and single CTCs to pass through while capturing the CTC-clusters with the dynamic force balances resulted from the flow paths. To eliminate the possibility of CTC-cluster dissociation, the device is designed to operate at sub-physiological flow rates to reduce the shear stress acting on the cells during the operation. The flow rate is much less than that of the other microfiltration or hydrodynamic-based enrichment techniques, which eliminated the need for cell fixation and is able to enrich viable CTC-

clusters. The continuous flow process and the specific microfeature designs that capture only the CTC-clusters prevent clogging of the device and allow the device to process large volumes of blood samples. Sarioglu et al. reported that when tested with the spiked blood sample under a flow rate of 2.5mL/h, the device is able to capture 41% of the two-cell clusters, 70% of the three-cell clusters, and 99% of the clusters that are formed by four or more cells. After rinsing the device with PBS, the captured CTC-clusters can be released from the device with a reverse flow, where he demonstrated the successful release of viable CTC-clusters with a release rate of 80%. An important note is that during the release of the CTC-clusters, the device was placed on a 4°C cold plate to reduce the non-specific adhesion of the cells to the device. A clinical study with a total of 60 melanoma, breast, and prostate cancer patients' samples was performed, and the Cluster-Chip was able to discover CTC-clusters in 24 of the samples tested. The ability of the device to release viable CTC-clusters from the Cluster-Chip enables further RNA sequencing to be performed on these clusters to obtain valuable information about the tumors. Furthermore, the Cluster Chip also allowed direct study of the enriched CTC-clusters and resulted in an important finding on how the CTC-clusters were able to pass through narrow capillaries and circulate inside the human body [131].

Another device that was developed to isolate viable CTC-clusters was introduced by Au et al. [132]. The device consists of a two-stage continuous-flow design where in the first stage, a modified version of the DLD arrays [133], [134] was used to separate the larger CTC-clusters from the rest of the cells, and in the second stage, the device utilizes the asymmetrical properties of the smaller CTC-clusters and designed specific pillar arrays for the discrimination. The height of the channel is designed to be 30 μm to ensure the

asymmetricity of the CTC-clusters are aligned in the XY-plane. Furthermore, to ensure the shear stress expressed on the cells is less than that of the shear stress in the peripheral capillaries [135], a flow rate of 0.5 mL/h was used which results in shear stress less than 4.8 Pa. With this flow rate, 99.3% of the large CTC-clusters and 79% of the small CTC-clusters were able to be recovered by the device when testing with spiked cancer cells in the buffer. However, these recovery rates decreased when testing with the spiked cells in whole blood samples where only 98.7 and 65.5% of the large and small CTC-clusters could be recovered, respectively.

The importance of CTC-clusters and their clinical utility can only be realized with advancement in the development of specific technologies that focus on the enrichment of CTC-clusters. With higher specificity and sensitivity in the enrichment of CTC-clusters, their physiological role in cancer metastasis can then be revealed through systematic clinical research.

2.2.2 Biochemical Based Approaches

Although biophysical-based CTC enrichment techniques have many attractive advantages such as label-free isolation, high-throughput, and high cell viability preservation, they often face the challenge of low purity due to the similar biophysical properties of CTCs and WBCs, resulting in high background noise of the enriched product [136], [137]. Unlike biophysical-based approaches, biochemical-based approaches that enrich CTCs based on the chemical interactions of the specific antigens or aptamers greatly increases the specificity of the isolation. In most cases, devices that enrich the CTCs based on the biochemical interaction utilize magnetic beads or direct capture to achieve high

purity and efficient enrichment [138], [139]. For example, epithelial cell adhesion molecule (EpCAM) or epidermal growth factor receptor 2 (HER2) are all common biomarkers used by the immunoaffinity devices to capture CTCs from various epithelial cancers including breast, prostate, lung, or colon cancers [140], [141].

2.2.2.1 Antibody-Based CTC Enrichment

The immunoaffinity-based CTC enrichment techniques often utilize the differences in cell antigens expressed on the cell membrane surfaces between CTCs and normal blood cells for the specific capture of the cells [142]. Through magnetic beads or direct antibody conjugation of the device surfaces [143], EpCAM [144]-[146] and CD45 [147], [148] are the two most common biomarkers for the depletion of epithelial CTCs and WBCs, respectively.

The use of antibody-labeled magnetic beads to bind to the target cells for the enrichment of the CTCs under a magnetic field is a very common approach in immunoaffinity enrichment techniques. For example, the CellSearch® system [149], [150] utilizes EpCAM-conjugated ferrofluid magnetic particles to separate the EpCAM-positive CTCs from the rest of the blood cells. The system then applied fluorescent staining to the isolated cells where anti-cytokeratin was used to stain the CTCs, anti-CD45 antibody was used to stain the WBCs, and DAPI was used to nuclei of the nucleated cells. After scanning the fluorescently labeled cells with the fluorescent microscope, only cells that are cytokeratin and DAPI positive but CD45 negative are considered CTCs. To this note, CellSearch® system can only detect CTCs that are EpCAM positive. Furthermore, it has been reported that CTCs with low EpCAM expression due to epithelial-mesenchymal transition (EMT) are not guaranteed to be detected, yielding a false negative result [151].

Another well know system that uses EpCAM labeled ferromagnetic beads for the enrichment of EpCAM positive CTCs is called the magnetic activated cell sorting (MACS) system. This system pre-labeled the EpCAM positive CTCs with the anti-EpCAM antibody conjugated ferromagnetic beads in the blood sample and separate them by processing the blood sample through a column with a strong magnetic field [152]. The ferromagnetic beads labeled cells are then trapped inside the column and are later released by terminating the applied magnetic field. The MACS system is able to achieve more than 100-fold enrichment of the CTCs while preserving more than 90% viability of the enriched cells. It has also been reported that the system can process billions of cells in under just 15 minutes. Another similar system to MACS is the Dynabeads magnetic separation technology [153]. Although the system can discriminate the magnetically labeled cells without the removal of the magnetic field, unlike the MACS system, the inconsistent cell recovery rates prevent it from being used for clinical studies [154].

Aside from the benchtop technologies, Nagrath et al. developed the first immunoaffinity-based microfluidic device, CTC-chip, for the enrichment of CTCs [155]. The device was able to process whole blood directly while detecting CTCs with high sensitivity and specificity. To fabricate the CTC-chip, deep reactive-ion etching (DRIE) was used to manufacture the channels as well as 100 μm tall micropillar arrays on the silicon substrate. The device was then functionalized with anti-EpCAM antibody to capture epithelial CTCs in the device. The micropillar arrays are designed to increase the interaction between EpCAM positive CTCs and the functionalized surfaces for better capture efficiency. The CTC-chip was able to detect more than 79 CTCs/mL in 115 out of the 116 cancer patients tested, from the reported results. A controlled experiment was also performed where no CTCs were observed in the healthy donor's blood sample. With this successful pioneer device, alternate versions of the immunoaffinity-based microfluidic devices were developed by various research groups [156]-[166]. One of which was the

Herringbone (HB) chip [167]. HB chip has very similar capture mechanism as the CTC-chip. The major difference between the two is that instead of implementing micropillar arrays to increase the cell to surface contact frequency, the HB chip uses herringbone grooves to disturb the laminar flow in the microchannel, which introduce turbulent mixing and microvortices within the herringbone regions for increasing the interactions between cells and functionalized surfaces [145]. Compared to the CTC-chip, under a flow rate of 1 mL/h, HB chip was able to achieve more than 90% capture efficiency, while CTC-chip was only able to achieve a capture efficiency of ~68%. Clinical samples were also tested using the HB chip, where out of the 15 prostate cancer patients tested, 14 of them were identified as positive with CTCs. Another similar device is the NanoVelcro CTC chip which nanopillars are implanted on the channel surface to increase the cell to surface contact frequency between the CTCs and the anti-EpCAM antibodies coated surfaces and thus, increase capture efficiency of the CTC [168]. Cell lines such as LNCaP, PC3, and C4-2 spiked in PBS buffer or blood were tested with the NanoVelcro CTC chip, and the device was able to obtain more than 80% capture efficiency in all of the simulated samples. High-throughput micro sampling unit (HTMSU) designed with 51 identical channels that are coated with anti-EpCAM antibodies was able to obtain a recovery rate of 97% of the CTCs from whole blood [169]. Not to mention the recent development of the 3D scaffold microchip was able to isolate both CTC single cells and CTC-clusters from the whole blood samples. The 3D scaffold device is able to process whole blood sample at a higher flow rate compared to other immunoaffinity devices and still maintain a high level of capture efficiency due to its unique 3D macropore structures. They greatly increased the cell to surface contact frequency and allowed EpCAM positive CTCs to be captured by the functionalized surfaces [170]. The device was able to identify CTCs in all of the 14 cancer patients' blood samples tested. Furthermore, when operated under a high flow rate of 100 μL/min, CTCs were detected in 5 of the 14 cancer patients, demonstrating the potential of the device for fast screening of the CTCs. The ability to sort CTCs with high or low

EpCAM expression is also another popular research area. This was demonstrated by Besant and Poudineh et al., where they developed a microfluidic device that utilizes flow rate and magnetic field strength to separate magnetic nanoparticle labeled CTCs with high and low EpCAM expressions. The device was designed with X-shaped microfeatures to discriminate CTCs based on their expression levels. Using this device, they were able to achieve more than a 90% recovery rate of the CTCs [171].

The high specificity provided by the immunoaffinity-based enrichment method overcomes the technical challenge faced by the biophysical-based enrichment method, but the difficulties in releasing the capture CTCs from the devices hinder the use of these devices for further downstream analysis of the CTCs [172].

2.2.2.2 Aptamer-Based CTC Enrichment

Apart from the biological antibodies, high specificity chemical antibodies known as the aptamers have also been used for the enrichment of CTCs [172]-[174]. Aptamers are short single-stranded DNA or RNA that takes the form of helices and single-stranded loops and can specifically bind to proteins, peptides, cells, etc. [175]. The selection of the aptamers for a specific target is usually made through the process of SELEX, which stands for Sequential Evolution of Ligands by Exponential Enrichment [176]. The process involves binding a large number of different oligonucleotides to the target and amplify only the ones that were able to bind to the target. To find the optimal aptamers for the CTC enrichment, a recent study demonstrated a tissue slide-based SELEX method to select aptamers for the lung cancer patient's tumor cells. This method allows specific aptamers to be selected for each patient [177].

Compared to the biological antibodies, aptamers exhibit many great advantages such as high affinity, reproducibility, and long shelf life, but one major advantage of aptamers over the antibodies is the ability to release the intact CTCs from the devices after

capturing [178]-[182]. Also, unlike the antibodies that only a few of them have been used for the enrichment of CTCs, a great number of different aptamers have been generated to bind to CTCs with high specificity [183], [184]. More importantly, the aptamers can be generated such that they cover the heterogeneous surface antigen expressed by the CTCs, thereby yielding a high capture efficiency [185], [186]. Furthermore, once the CTCs are captured by the microfluidic devices, nuclease enzymes or complementary oligonucleotides can be employed to release the captured CTCs while preserving their viability at the same time, which is compatible for further live analysis [187], [188].

Incorporating the use of an aptamer-nanoparticle in a lateral flow device, Liu et al. have demonstrated the use of aptamer for the identification of Ramos cells [189]. Two different aptamers, thiolated aptamer TD05 and biotinylated aptamer TE02, were selected for the enrichment of Ramos cells through the SELEX process and were immobilized on both the gold nanoparticles and the nitrocellulose membrane in the test zone of the device. When the Ramos cells enter the device, they bind to the aptamer labeled gold nanoparticles and the nitrocellulose membrane, which causes a red band to occur. However, when tested with the blood sample, it was found that RBCs were non-specifically binding to the nitrocellulose membrane, which prevented its use for cell identification in blood samples. Another system that utilizes 20-40 μm diameter pores graphene oxide membrane coated with RNA aptamer was developed by Viraka Nellore et al. [190]. The membrane was able to process blood samples and identify different types of cancer cells through the fluorescent labeled aptamers. The results demonstrated that the aptamer labeled membrane was able to capture SKBR3, LNCaP, and SW-948 cells with more than 95% recovery rates.

The combination of aptamers in microfluidic devices has also enabled the enrichment of CTCs from clinical samples [191]. Such as the aptamer-modified microfluidic device developed by Phillips et al. [192], which was able to achieve a 135-fold enrichment of the target cells with a purity of 97% [193]. Another example is the

multivalent DNA aptamer-based microfluidic device developed by Zhao et al. for the capturing of lymphoblast CCRF-CEM cells [194]. The herringbone design in the device allowed the DNA aptamers to form a 3D network and created multiple binding sites. It was shown that this multivalent DNA aptamer was able to outperform the monovalent aptamers under various flow conditions and capture the target cells with a higher capture efficiency and purity [195]. Sheng et al. developed another microfluidic device with aptamer modified micropillar arrays and was able to directly process unmanipulated whole blood samples to recover tumor cells with cell density as low as 10 cells/mL while maintaining a recovery rate higher than 95% [196]. Similarly, Wan et al. introduced a PDMS Hele-Shaw device with RNA aptamers functionalized glass beads embedded in the designed pit arrays. From a controlled experiment, it was shown that the aptamer conjugated glass beads were able to isolate overexpressed epidermal growth factor receptor (EGFR) hGBM cells with a 44% efficiency, while 92% of the captured cells can be eventually released from the device for further analysis by the complementary aptamers [197]. Wang et al. combined the use of RNA-aptamer and microelectrodes and developed an electrical tumor cell detection device, where the captured tumor cells on the aptamer functionalized electrodes can be detected through the change in resistance [198].

Sheng et al. developed a microfluidic device for the application of human acute lymphoblastic leukemia (CEM) cells enrichment from whole blood samples. The device combines the use of herringbone structures in the microfluidic device and the aptamer-functionalized gold nanoparticles and multivalent DNA aptamer nanospheres for the enrichment [199]. The combined effects from the aptamer functionalized particles and the herringbone structures enable the device to achieve a 92% recovery rate of the CEM cells in PBS buffer and about 90% recovery rate of the CEM cells that were spiked in whole blood samples. Zhao et al. employed aptamer cocktails in a microfluidic device for CTC enrichment and have successfully demonstrated the synergistic effect from the different

aptamers to achieve a high capture efficiency [200]. Recently, Labib et al. have developed a 2D microfluidic assay that is able to separate CTCs with different EpCAM and HER2 expression levels into 16 subpopulations. The device utilizes aptamer conjugated magnetic nanoparticles for the separation and differentiates cells based on their magnetic strength [201].

The aptamer-based CTC enrichment technologies allow for the simple release of the capture CTCs without affecting their viability. They also provide higher sensitivity and capture efficiency, especially with aptamer cocktails, making the aptamer-based enrichment approaches an attractive method for CTC enrichment.

2.2.3 Hybrid Technologies

Technologies that combine the use of biophysical and biochemical-based enrichment methods to enhance the performance have also been developed. By combining the use of different methods in the same device, the device can gain each method's advantages while eliminating the drawbacks of each individual technique. For example, in the CTC-iChip developed by Ozkumur et al. and Karabacak et al., it combines the use of DLD, inertial focusing, and immunoaffinity-based enrichment techniques which eliminated the need for RBC lysing that is usually required for the immunoaffinity-based approach and the lack of specificity faced by the DLD approach [202], [203]. To process the blood sample through the device, WBCs are pre-labeled with CD15 and CD45 immunomagnetic beads in the negative selection mode (negCTC-iChip) while CTCs are pre-labeled with anti-EpCAM conjugated immunomagnetic beads in the positive selection mode (posCTC-iChip). After pre-labeling of the blood sample, cells are injected into the inlet of the device where anucleated cells, such as the RBCs and platelets, are eliminated

by the DLD component of the device, allowing the WBCs and CTCs to move on to the inertial focusing channel. The WBCs and CTCs are then focused into a single line by the inertial focusing channel that prepared them for the magnetic separation stage. Finally, the WBCs and CTCs are introduced to a magnetic field that separates them from one another and completes the enrichment process. In the reported results, the negCTC-iChip had a consistent recovery rate of 97% for all of the cancer cell lines tested, while the cancer cell recovery rate for the posCTC-iChip varies from 77.8% to 98.6%, which was greatly dependent on the EpCAM expression level of the cell lines. It was also reported that the posCTC-iChip was able to outperform the CellSearch® system in detecting and recovering CTCs from blood samples with low CTC density (less than 4 CTCs/mL).

Other research groups have also combined batch processes with microfluidic approaches to increase the efficiency of CTC enrichment. For example, Park et al. were able to achieve high recovery rates of the DMS-79 and MCF-7 cells from whole blood samples by combining the use of immunoaffinity, density gradient centrifugation, and on-chip microfiltration [204]. The spiked cells in the blood sample were pre-labeled with size-density amplification beads (SDABs) before the centrifugation. The SDABs can significantly increase the density and size of the cell, so after centrifugation, tumor cells with SDABs attached aggregated at the bottom of the centrifugation tube, allowing the normal blood cells to be removed through aspiration. The residual cells in the centrifugation tube were then processed through the on-chip filter, where the SDABs attached tumor cells were retained on the filter. It was reported that a recovery rate as high as 99% was achieved using this method, while more than 99% of the WBCs were removed during the process.

Although devices that combine multiple enrichment techniques can lead to high complexity in both the fabrication and preparation of the device, they also combine the advantages of different enrichment methods and yield higher sensitivity and specificity for the enrichment of CTCs.

CHAPTER 3. MICROFABRICATION OF THE 3D-PRINTED MICROFLUIDIC DEVICE FOR CTC ENRICHMENT

Conventional microfluidic devices are typically fabricated by first, photolithographically patterning the SU-8 photoresist to create the 2D master templates. By the use of photolithography, specific microstructures and desired microchannel dimensions can be created on the SU-8 photoresist. Soft lithography is then applied to transfer the channel geometry onto a polymer. During the soft lithography process, a liquid polymer is pour over the 2D SU-8 template and cure by either heat or UV-light to create an inverted replication of the SU-8 channel geometry. Polydimethylsiloxane (PDMS) is the conventional material used for the soft lithography of the microfluidic device due to its great biocompatibility, high transparency, and low cost. Lastly, bonding the cured polymer onto a glass slide or other substrate completes the fabrication of the microfluidic device [30]. This fabrication method has been dominating the ways for microfluidic device fabrication over the past decades due to its high precision in creating desired microchannel geometries and microfeatures, as well as the reusability of the SU-8 master templates for reproducing microfluidic devices with the same structure using the same template.

Although microfluidic devices fabricated using the conventional method have been used to develop many different lab-on-a-chip devices with various applications, the advancement in 3D-printing has generated a great interest in the microfluidic community to use it as a new way of fabricating microfluidic devices. As mentioned earlier, with the advancement in the resolution of 3D printing technology, the current state-of-the-art 3D printers are capable of printing microscale features [37], [38]. They have emerged as a new

fabrication approach for microfluidic devices that exhibit many advantages over conventional microfluidic devices. 3D-printing allows microfluidic devices to be created in places where cleanroom facility is unavailable. The simple click-and-print fabrication process allows fast iteration of the design [37]. Also, one of the most noticeable advantages is the ability to create complex 3D microfluidic channels that are not possible in conventional microfluidic devices [41]. This overcomes the limitation faced by conventional microfluidic devices with only planner microchannel networks and allows the designing of microchannels in the third dimension, which can potentially be beneficial for different applications. But currently, there are also challenges associated with the creation of microfluidic devices using 3D-printing.

While it is straightforward to 3D-print solid objects, geometries embedded with fully enclosed microfluidic channels pose problems due to challenges associated with post-processing these structures to clean off uncured material trapped within the channels. Microfluidic devices are typically printed layer-by-layer via inkjet 3D-printing (i3DP) or stereolithography (SLA) due to their relatively high printing volume and resolution [205]. In i3DP, devices are printed by depositing sacrificial material as a space holder in channels, while the SLA relies on laser-induced curing of solid sections leaving the channels filled with a highly viscous uncured resin [206], [207]. Although an injection-based etching of the sacrificial materials from the printed microchannels has been developed [208], it is only suitable for discharging sacrificial materials or viscus uncured resin from simple channel geometry with low fluidic resistance. It is often not possible to fully discharge these sacrificial materials out of complex microfluidic channels, especially in devices with long and narrow channels containing densely packed microscale features [209]-[214].

Considering the advances in 3D-printing resolution, smaller microfluidic channels will only exacerbate the challenges associated with etching sacrificial materials in microfluidic channels. In fact, to alleviate these challenges, microfluidic channels were partially 3D-printed with an open side to expose the sacrificial material for etching and were later sealed to form the final device [215]-[219]. However, partial 3D-printing of devices not only complicates the fabrication process but also forfeits the capability to manufacture monolithic devices with freeform 3D geometries.

The challenges in reliably removing the sacrificial material from fully enclosed microfluidic channels hinder the use of 3D-printing to create microfluidic devices with intricate geometries. With advances in printer resolution, the etching of sacrificial materials from increasingly smaller channels is poised to be a bottleneck using the existing techniques. To overcome this challenge, I have developed a microfabrication approach that utilizes centrifugation to effortlessly and efficiently remove the sacrificial materials from 3D-printed microfluidic devices with densely packed microfeatures. I have characterized the process by measuring the etch rate under different centrifugal forces and developed a theoretical model to estimate process parameters for a given geometry. The effect of the device layout on the centrifugal etching process was also investigated. I demonstrate the applicability of the developed approach on devices fabricated using inkjet 3D-printing and stereolithography. The advantages of the developed approach over commonly used injection-based etching of sacrificial material were also experimentally demonstrated in direct comparisons. Lastly, I demonstrated the feasibility of fabricating complex 3D microfluidic devices using the developed method.

3.1 Device Design and Fabrication

The microfluidic devices were designed using SolidWorks. The majority of the devices presented in this thesis was printed with a PolyJet 3D printer (ProJet 3510 HD) as the printer was readily available to us as a shared Georgia Tech resource using VisiJet® M3 Crystal plastic and VisiJet® S300 (density ~0.88 g/cm^3 and viscosity ~13 mPa·s) sacrificial wax material. The microfluidic devices used for the rate characterization experiments measured 1.5 cm × 3.9 cm × 175 μm containing periodically placed 800 μm-diameter micropillar arrays with an 800 μm-pitch and had a single inlet and an outlet. The printing process started by first depositing a thin layer of the sacrificial wax material for planarization. After the device was printed, it was separated from the platform in a -20 °C freezer utilizing the difference in materials' contraction rates.

To manufacture microfluidic devices with stereolithography, we used on-demand printing services from Stratasys and 3D Systems. Specifically, the devices were printed using ProJet 7000 HD and Viper Si2, on two different materials (Accura ClearVue, density ~1.10 g/cm^3 and viscosity ~250 mPa·s, and Somos WaterClear Ultra 10122, density ~1.13 g/cm^3 and viscosity ~165 mPa·s). Printed devices were post-cleaned in isopropyl alcohol under ultrasonication to remove the uncured resin on the exterior surfaces of the printed devices.

3.2 Post-Processing of 3D-Printed Device

3.2.1 Injection-based processing of 3D-printed devices

To remove the sacrificial material with the injection-based process, a 30 mL syringe was connected to the inlet of the printed device and the manufacturer-suggested etching

liquid for the specific sacrificial material was injected into the microchannels. Specifically, for the devices fabricated with inkjet printing in this study, the printed devices were first placed in a mineral oil ultrasonication bath, which was heated above the glass transition temperature of the sacrificial wax, 65 °C, to liquefy the wax inside microchannels. Later, a warmed mineral oil (65 °C) was injected into the microchannels at a flow rate of 0.3 mL/min controlled by a syringe pump for 30 minutes [208]. Soapy water and DI water were then sequentially injected to remove the residual mineral oil and soapy water, respectively. As for the devices printed using stereolithography printers, they were first submerged in an isopropyl alcohol bath and injected with isopropyl alcohol to remove the uncured resin. A syringe pump was used to provide a 0.1 mL/min injection rate for 30 minutes. Followed by a rinse with DI water, the devices were then dried with pressurized air and post-cured with ultraviolet illumination following the manufacturer-suggested protocol. For any high-fluidic-resistance microchannel that would not accept the etchant with the syringe pump, we attempted to inject the etchant by hand to apply a higher force as the last resort and stopped when either the device was damaged or the etchant leaked from the inlet.

3.2.2 Centrifugal processing of 3D-printed devices.

The printed devices were placed in 50 mL-conical-tubes and centrifuged as submerged in their respective solvents. For devices fabricated with inkjet printing, printed devices were placed in mineral oil with a density of ~0.83 g/cm3. The chamber centrifuge was heated to 65 °C and the centrifugal forces were modulated throughout the characterization studies by setting the rotor spin rate (Figure 1).

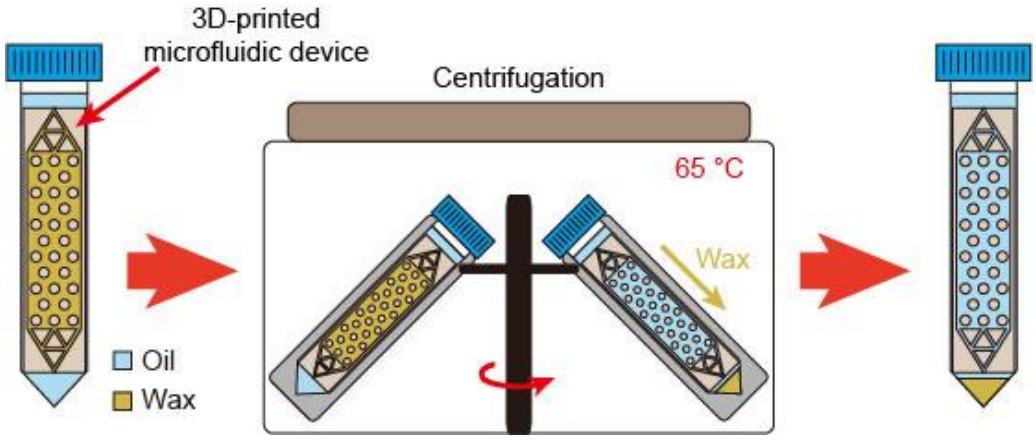

Figure 1: Centrifugal etching of the sacrificial wax material from microchannels in a 3D-printed device.

The devices were later centrifuged first in soapy water to remove the mineral oil and then in DI water for the final wash. Devices printed with stereolithography were centrifuged as immersed in isopropyl alcohol (density ~0.79 g/cm3) to remove the uncured resin from the microchannels. Centrifuged devices were later subjected to ultraviolet illumination for a final curing step per manufacturer-provided instructions. Successful etching of the sacrificial material was qualitatively confirmed by filling the channels with a dye solution and thorough inspection under an optical microscope (Figure 2).

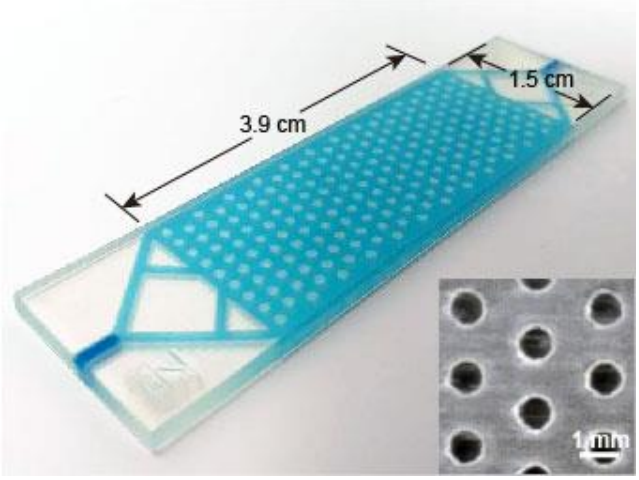

Figure 2: Photo of a 3D-printed microfluidic device after the sacrificial wax material was etched under centrifugation.

It should be noted that the amount of liquid in centrifuge tubes was set to ensure complete immersion of the printed device. Multiple devices could also be centrifuged concurrently in the same tube provided that there was sufficient liquid to cover all (Figure 3a). Finally, the partitioning of sacrificial material and the liquid ambient at the end of the centrifugation process could allow reusing the same chemicals repeatedly to process different devices to minimize chemical waste (Figure 3b).

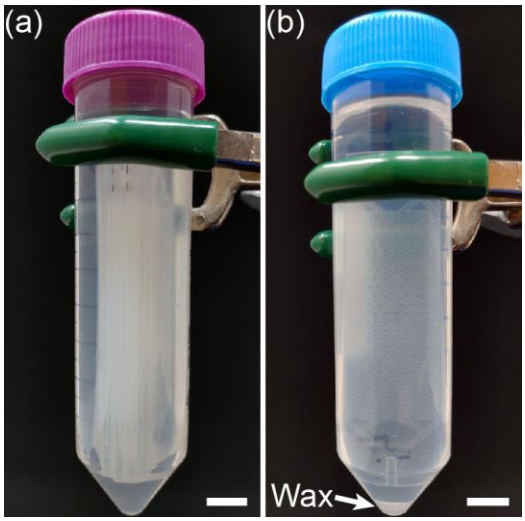

Figure 3: Reducing the chemical waste for centrifugal etching of sacrificial materials.

3.3 Process Characterization

3.3.1 Effect of the Centrifugal Force

Using the inkjet-printed microfluidic devices as the model system, we characterized the centrifugal etching process. We measured the centrifugal etch rate under forces ranging from 140 to 2170 × g. Within the tested force range, we could visually observe the heavier sacrificial wax material being gradually discharged from the device and replaced with the mineral oil. To quantitatively determine the rate of centrifugal discharge, we longitudinally weighed the devices every 15 minutes with an analytical balance starting with the as-printed ones having the channels completely filled with the sacrificial wax material (Figure 4).

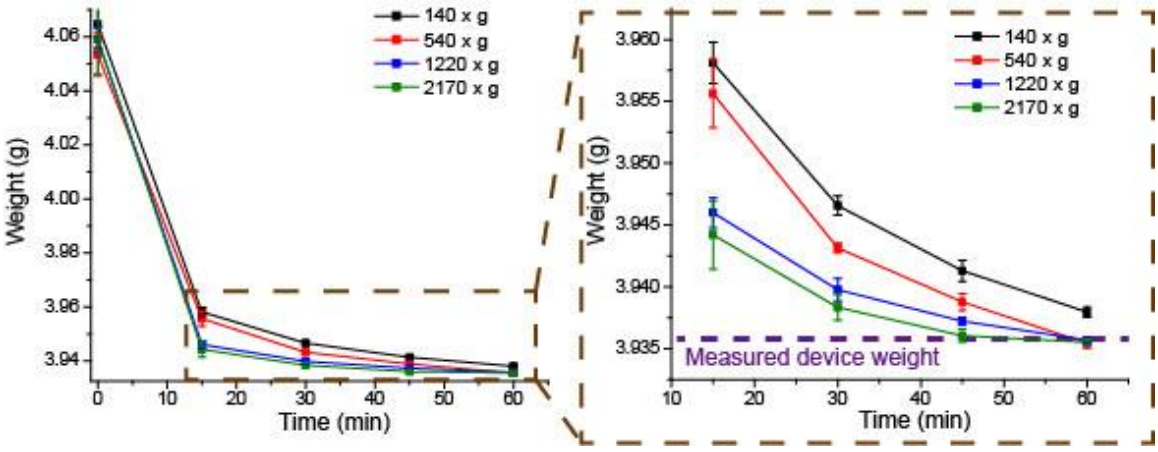

Figure 4: Investigation of residual sacrificial wax material in microfluidic devices for different centrifugal forces and times.

To determine the weight of the device free of the sacrificial wax material, an analytical device with identical geometry was printed as-split in half, exposing the microfluidic channels and ensuring complete etching of the wax with no centrifugation. The total weight of the wax-free portion of the device was then determined by averaging the sum of the weights of these two parts from three separate sets (~3.935g±0.001g) and was considered as a benchmark for the successful etching of the sacrificial wax material.

The amount of etched sacrificial wax material was observed to depend on both the centrifugal force and the duration of centrifugation. For the microfluidic devices centrifuged at 140 × g, the weight of the device was found to be higher than the fully-dewaxed device even after 60 minutes of centrifugation, suggesting residual wax in channels. However, all of the sacrificial wax material could successfully be discharged under 540 × g and 1220 × g, with both measured weights converging to that of the fully-dewaxed device at 60 minutes (Figure 4). For 2170 × g, the device was found to be free of the sacrificial wax material even after 45 minutes of centrifugation. It was clear that the higher centrifugal forces required less processing time to discharge sacrificial wax material. On the other hand, it should be noted that higher centrifugal forces risked device deformation as observed at 1220 and 2170 × g (Figure 5). These deformations, most

notably bending along its length where it is most compliant, can potentially be minimized by mechanically supporting the devices in the conical.

Figure 5: Deformation of the 3D-printed device under high centrifugal force.

To independently validate the centrifugal etching of the sacrificial material, we directly probed the inner surfaces of the 3D-printed microchannels for residual wax with Fourier-transform infrared spectroscopy (FTIR). For these measurements, devices taken out of the centrifuge were cut open to expose the channel for scanning. We first measured the FTIR spectrum of the cured resin (VisiJet® M3 Crystal) and compared the FTIR spectra of devices taken out of centrifugation at different time points to detect residual sacrificial wax material in the channels (Figure 6). We found that the FTIR spectra of as-printed devices whose channels were completely filled with the sacrificial wax material showed higher absorbance, especially below 1750 cm^{-1}. With increasing centrifugation time, the measured FTIR spectra gradually conformed to the FTIR spectra of the cured resin, proving, in support of the weight measurements, that sacrificial wax material could successfully be discharged from the microfluidic device.

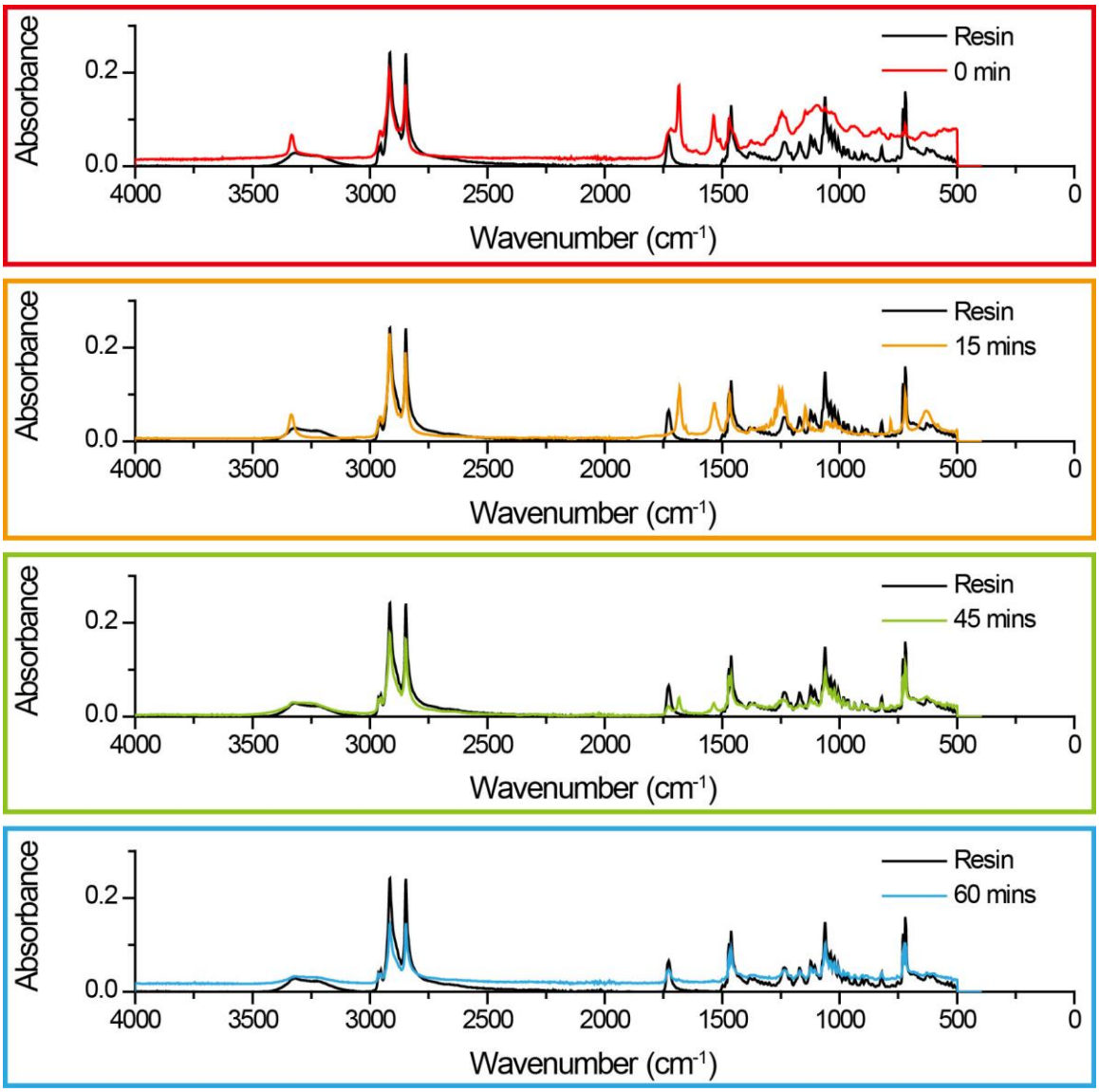

Figure 6: Measured FTIR spectra acquired from the inner surfaces of the microfluidic devices.

3.3.2 Effect of the Microchannel Geometry

We tested the applicability of our technique on microfluidic channels with different geometries. We first investigated the effects of microfluidic channel orientation on the etching of the sacrificial wax material. As long as a microfluidic channel was composed of polygon chains monotone with respect to the direction of the centrifugal force, the

sacrificial material was coherently driven by centrifugal forces and the channels could be fully cleared off the sacrificial material under centrifugation (Figure 7).

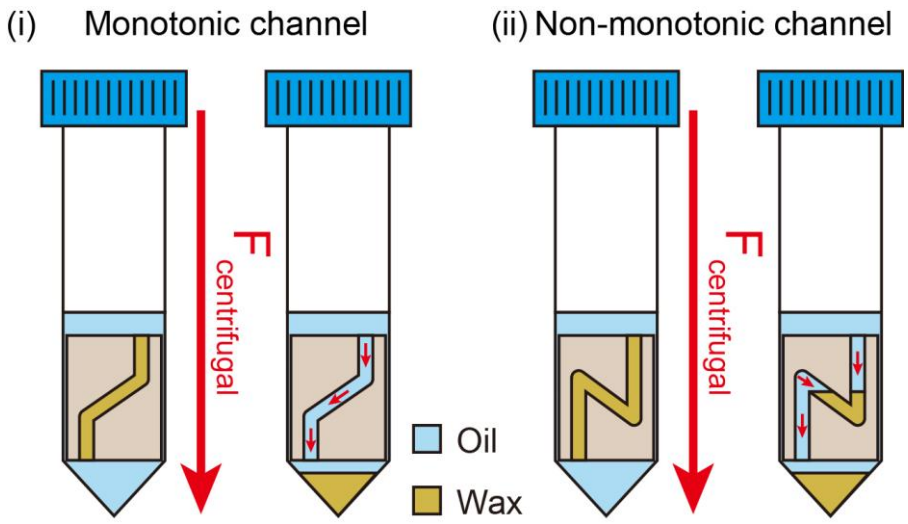

Figure 7: A schematic showing the direction of centrifugal forces and the resulting sacrificial material motion in monotonic and non-monotonic microchannels being centrifuged.

We found that microchannel sections aligned with offsets as small as 1 degree from the normal were clear of the sacrificial material (Figure 8).

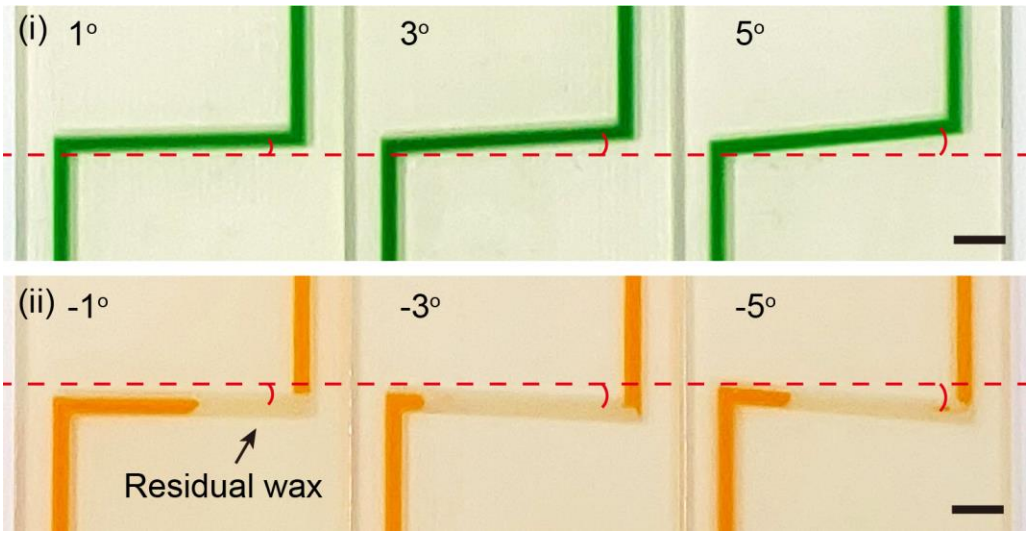

Figure 8: Images of (i) monotonic and (ii) non-monotonic microchannels taken after centrifugation.

On the other hand, a microfluidic channel non-monotone with respect to the centrifugal force led to sacrificial material being trapped locally at certain nodes and could not be cleared. These observations were also independently confirmed by the measured FTIR spectra from non-monotonic microchannels (Figure 9).

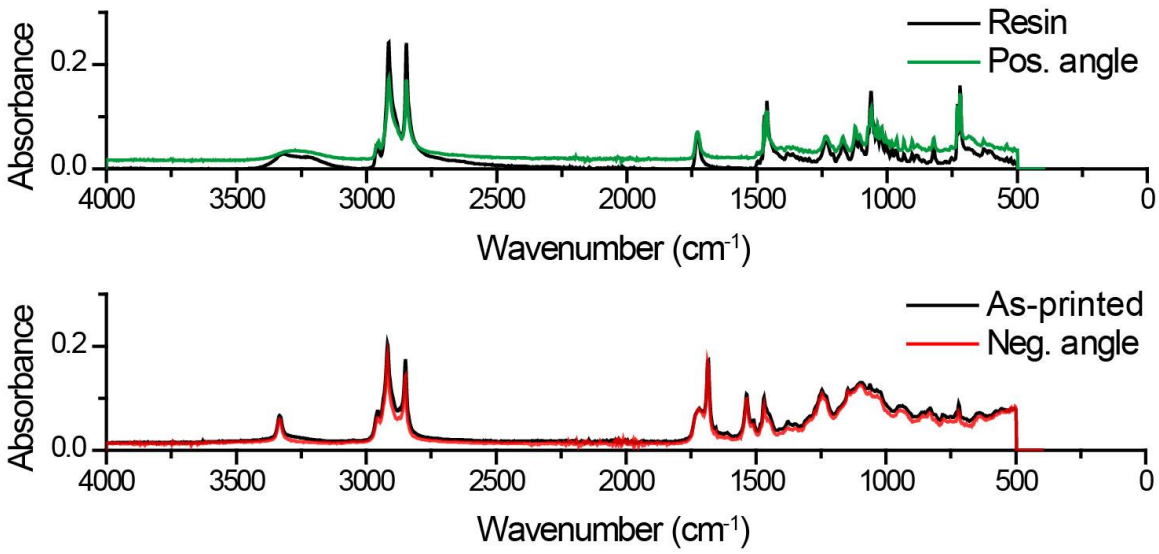

Figure 9: Comparison of FTIR spectra acquired from monotonic and non-monotonic microchannels.

While the requirement of designing microchannels exclusively of monotone polygon chains constraints the device design, this limitation could be alleviated by transforming the channel geometry for certain designs (Figure 10).

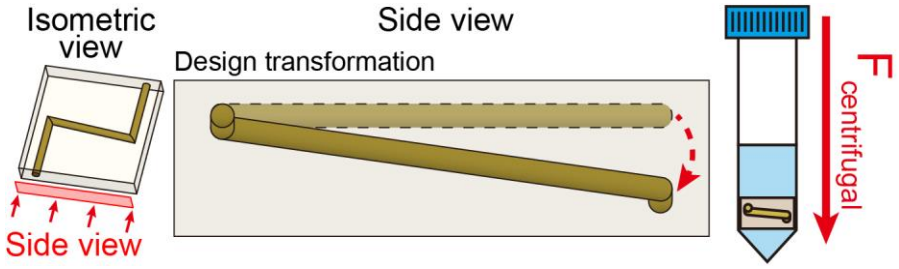

Figure 10: A schematic illustrating the geometrical transformation of a planar, non-monotonic microchannel into a 3D monotonic channel in the third dimension.

In fact, any planar geometry can be transformed to be monotone in the third axis by introducing a constant slope utilizing the 3D patterning capabilities of additive manufacturing (Figure 11).

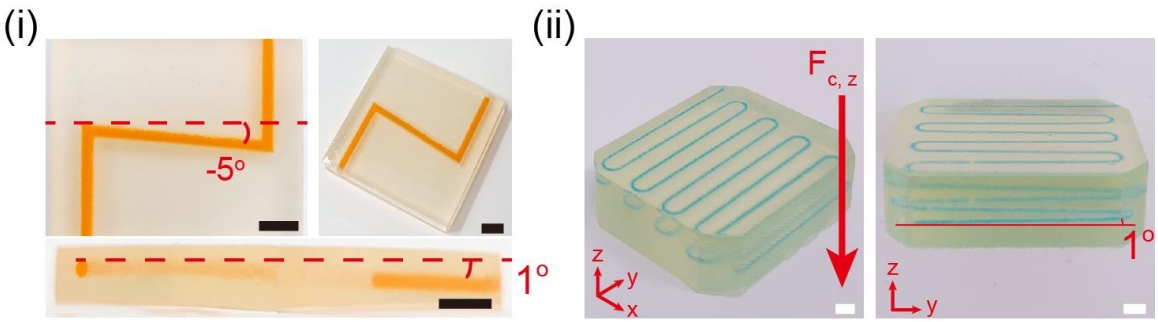

Figure 11: Images show two different transformed non-monotonic microchannels successfully cleared of sacrificial materials.

Sacrificial material inside microchannels designed using this approach could successfully be removed only when centrifuged along the monotonic axis (Figure 12).

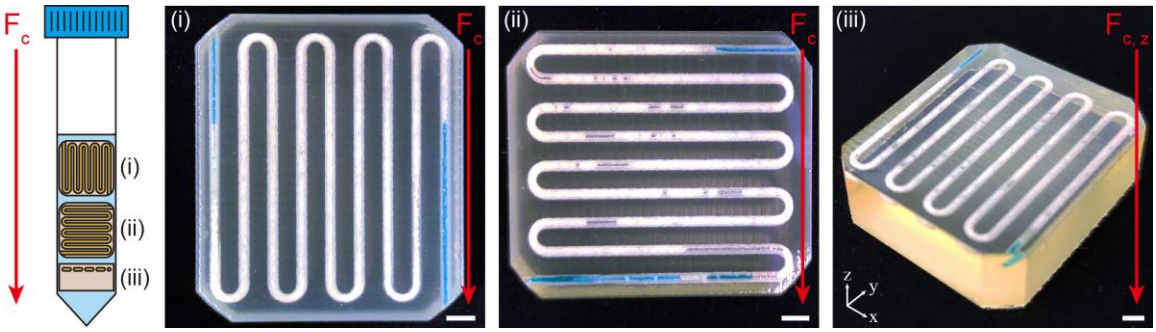

Figure 12: Centrifugal etching of a non-monotonic microchannel.

These results demonstrate the applicability of centrifugation for additive manufacturing for a large class of microchannel geometries, including all 2D designs and their multi-layered implementations. On the other hand, 3D microchannels that cannot be transformed to be monotone with respect to any axis would lead to incomplete etching of the sacrificial material under centrifugation and typify the device geometry-related limitations of our approach.

Next, we investigated the effect of microchannel fluidic resistance on the etching of the sacrificial material through centrifugation. The fluidic resistance (*R)* of a microchannel strongly depends on its geometry as is given by [221]:

$$R = \frac{128\mu L}{\pi d^4} \tag{1}$$

where μ is the dynamic viscosity of the fluid, L and d are the length and cross-sectional diameter of the channel, respectively. Therefore, we tested the etching of sacrificial materials from channels with varying lengths and cross-sections to test the effect of fluidic resistance on the process. Specifically, we inkjet-printed 58 mm-long microchannels with different cross-sectional diameters ranging from 1200 µm down to 200 µm, the smallest feature size we could reliably achieve. Taking the viscosity of the sacrificial wax at 65 °C into account, the smallest of these channels had a fluidic resistance of 1.92×10^{13} Pa·s/m^3. When subjected to centrifugation, we observed the sacrificial wax could successfully be discharged from all of the tested microchannels (Figure 13).

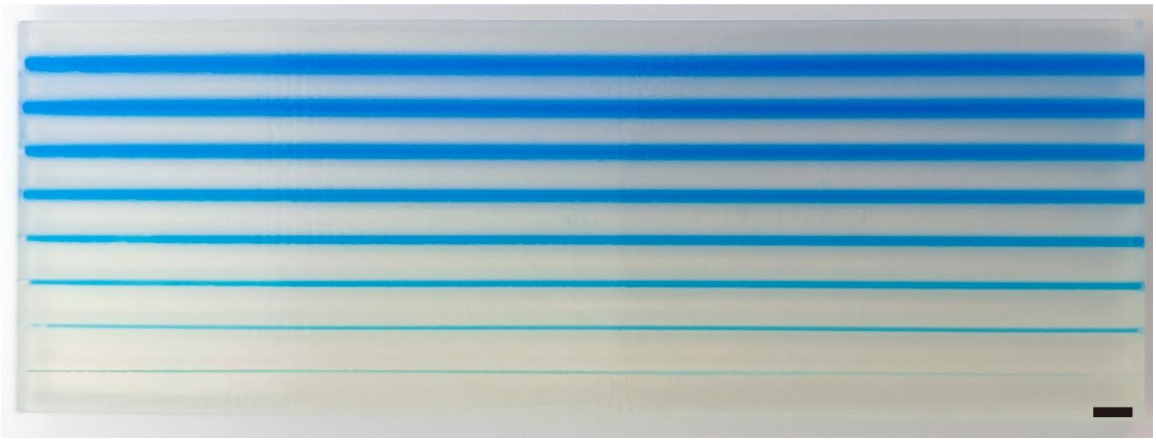

Figure 13: Images of microchannels, dewaxed under centrifugation, with cross-sectional diameters varying from 1.2 mm to 200 µm.

To demonstrate the validity of our approach for different printing technologies, we performed the same test on the microchannels printed with SLA. We fabricated a microchannel with a 300 µm cross-sectional diameter, the smallest channel diameter printable by the printer, and 176.95 mm channel length. Based on the dynamic viscosity value of 250 mPa·s provided by the manufacturer, the channel was estimated to have a fluidic resistance of 2.23×10^{14} $Pa \cdot s/m^3$. When centrifuged, the uncured resin was completely removed from the serpentine channel without any special measures or treatments (Figure 14).

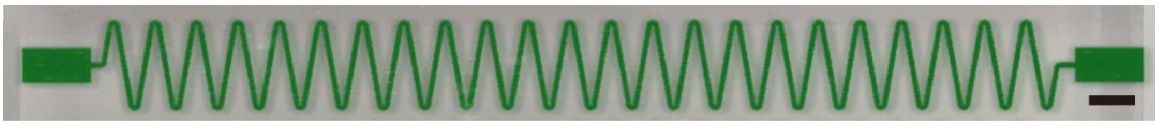

Figure 14: Image of a 300 µm-diameter serpentine microchannel with uncured resin removed through centrifugal etching.

While our experimental study was limited to channel diameters on the order of ~100 µm due to printer resolution, we expect the centrifugal forces to be effective in removing sacrificial materials from channels with smaller cross-sections as the centrifugal forces can uniformly be applied over the volume of the sacrificial material irrespective of the microchannel fluidic resistance.

3.4 Mathematical Modeling

To estimate the centrifugation parameters for different combinations of device geometry and materials, we derived a mathematical model for the centrifugal etching of sacrificial materials from microchannels. We considered the three forces exerted on the

sacrificial material during centrifugation, which are centrifugal force (FC), buoyancy force (FB), and drag force (FD), which could be expressed as:

$$F_c = m_s a_c = \forall_s \rho_s a_c \tag{2}$$

$$F_B = \forall_s \rho_{fluid} a_c \tag{3}$$

$$F_D = \frac{C_d \rho_{fluid} v_m^2 A}{2} \tag{4}$$

where m_s is the mass of the sacrificial material, $\forall_s$ is the volume of the sacrificial material, ρ_s is the density of the sacrificial material, ρ_{fluid} is the density of the fluid, a_c is the tangential acceleration, v_m is the terminal velocity, C_d is the drag coefficient, and A is the projected area of the sacrificial material normal to the direction of the motion. The tangential acceleration in a centrifuge can then be expressed as

$$a_c = r\left(\frac{2\pi N}{60}\right)^2 \tag{5}$$

where r is the centrifugal radius and N is the rotational speed of the centrifuge in revolutions per minute. For the laminar flow regime, drag coefficient is inversely proportional to Reynold's number [220], which can be expressed as follows:

$$C_d = \frac{\alpha}{Re} = \frac{\alpha \mu_{fluid}}{D_{avg} v_m \rho_{fluid}} \tag{6}$$

where α is a constant coefficient, μ_{fluid} is the dynamic viscosity of the fluid, and D_{avg} is the average diameter of the microfluidic channels. To solve for the terminal velocity, we balance the forces as

$$F_c - F_B = F_D \tag{7}$$

and express the terminal velocity as

$$v_m = \frac{2D_{avg}\forall_s r\left(\frac{2\pi N}{60}\right)^2\left(\rho_s - \rho_{fluid}\right)}{\alpha\mu_{fluid}A} \tag{8}$$

The rate of change in the weight of the sacrificial material can then be calculated by multiplying the terminal velocity, the projected area and density of the sacrificial material as

$$\frac{dw_s}{dt} = -w_s \cdot \frac{2D_{avg} r\left(\frac{2\pi N}{60}\right)^2\left(\rho_s - \rho_{fluid}\right)}{\alpha\mu_{fluid}} \tag{9}$$

where w_s is the weight of the sacrificial material. The weight of the centrifuged 3D-printed device, *w(t)*, can then be obtained by solving Equation 8 subject to the boundary conditions:

$$w(0) = w_{initial}, \qquad w(\infty) = w_{3D\ material}$$

where $w_{initial}$ is the initial weight of the as-printed device and $w_{3D\ material}$ is the weight of the device free of sacrificial material. As such, we calculate the weight of the centrifuged device as a function of time as

$$w(t) = C_1 e^{-\frac{2D_{avg} r\left(\frac{2\pi N}{60}\right)^2\left(\rho_s - \rho_{fluid}\right)}{\alpha\mu_{fluid}} t} + C_2 \tag{10}$$

with

$$C_1 = w_{initial} - w_{3D\ material}, \qquad C_2 = w_{3D\ material}$$

Applying the model using the parameters of the earlier experimental study, we found our model could successfully capture the effects of the centrifugal force and time (Figure 15). The experimentally observed etch rates being faster than the theoretical rates is likely due to the fact that the chemical interaction between the wax and the oil were not accounted for in our model.

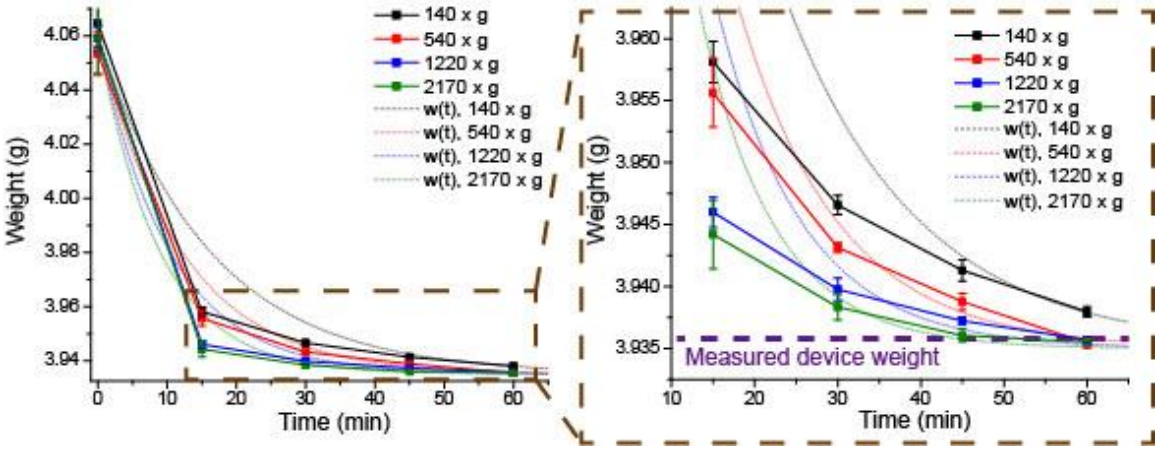

Figure 15: Estimated time-change of the centrifuge device weight based on the derived mathematical model.

3.5 Comparison with Injection-Based Etching

To experimentally compare our technique with injection-based etching of sacrificial material in 3D-printed microchannels [205], we printed matching geometries with both inkjet (ProJet 3510 HD) and SLA (ProJet 7000 HD) printing and evaluated microchannels after post-processing. We first printed serpentine microchannels with cross-sections as small as permitted by the specific 3D-printer and used them as representative models for challenging geometries with high fluidic resistance. The printed channel had

cross-sectional diameters of 200 and 300 µm and an effective channel length of 166.2 mm, which were estimated to produce fluidic resistances of 5.50×10^{13} and 2.09×10^{14} Pa·s/m^3 when filled with the support wax (VisiJet® S300) and the uncured resin (Accura ClearVue), respectively. When we attempted to inject the respective etchants into these microchannels, we failed to clear the microchannel for both sacrificial materials (Figure 16) with some devices eventually cracking under excessive pressure.

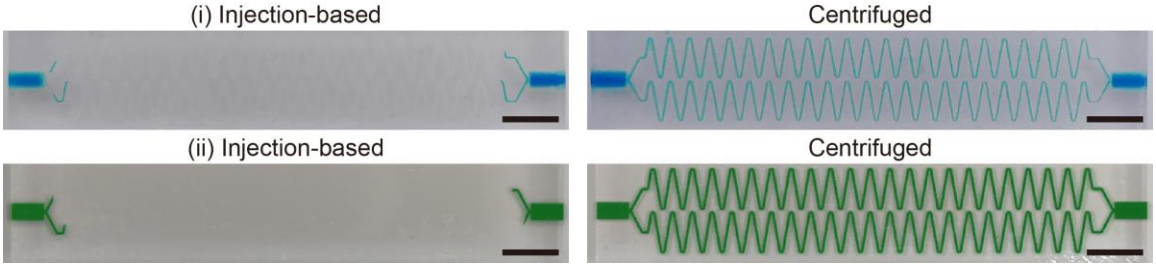

Figure 16: Images of serpentine microchannels fabricated by inkjet (top) and SLA (bottom) printers after they were subjected to injection-based and centrifugal etching.

These observations were, in fact, consistent with the previous reports on injection-based cleaning of 3D-printed microchannels [222]. In contrast, microchannels subjected to centrifugation as immersed in specific etchants could be successfully cleared for both materials. These results clearly demonstrated the advantage of uniform centrifugal forces acting on the material to be etched over injecting an etchant under a pressure gradient between the inlet and outlet for clearing microchannels with high fluidic resistances.

Next, we investigated both centrifugal and injection-based processing of 3D-printed geometries consisting of enclosed microchannels with varying cross-sectional areas. We first printed parallel microchannels with the previously studied serpentine geometry using two different SLA printers (Figure 17).

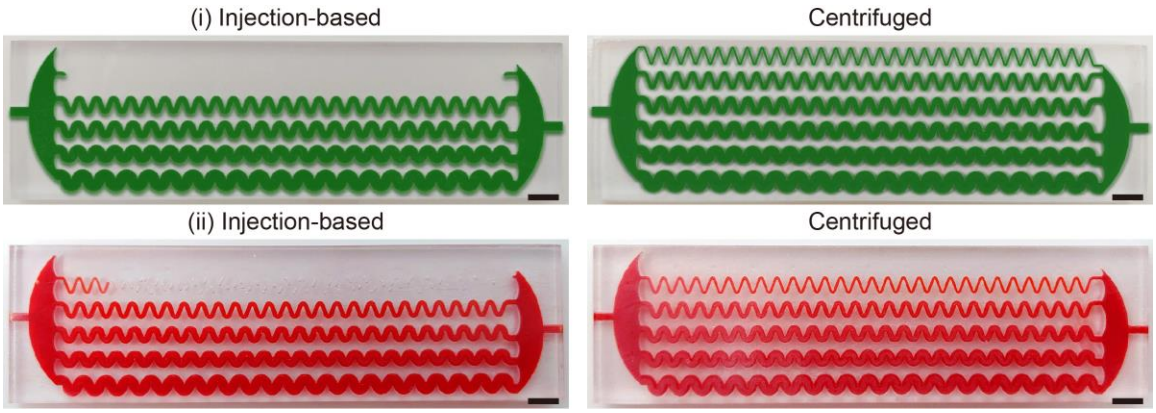

Figure 17: Images of microfluidic devices with parallel microchannels that have cross-sectional diameters varying from 300 µm to 1800 µm.

The channel cross-sectional diameters of individual microchannels varied from 300 µm to 1800 µm with 300 µm increments, which led to fluidic resistance between the microchannels to vary by as much as >2000X on the same device. When we attempted to clear microchannels by injecting isopropyl alcohol into the device, the microchannels with higher fluidic resistances (the microchannels with 300 µm and 600 µm cross-sectional diameters) could not be cleared from the uncured resin. This was because the larger parallel microchannels, once cleared off the viscous resin, did present a significantly reduced fluidic resistance, effectively shunting the smaller microchannels still filled with the uncured resin and limiting the amount of pressure gradient that could be sustained across the more resistive microchannel needed to remove the viscous resin. In fact, when we performed the same etching process on the 600 µm-diameter microchannel in isolation (Figure 18), we could clear the microchannel of the uncured resin, demonstrating it was not the fluidic resistance that actually failed the etching process.

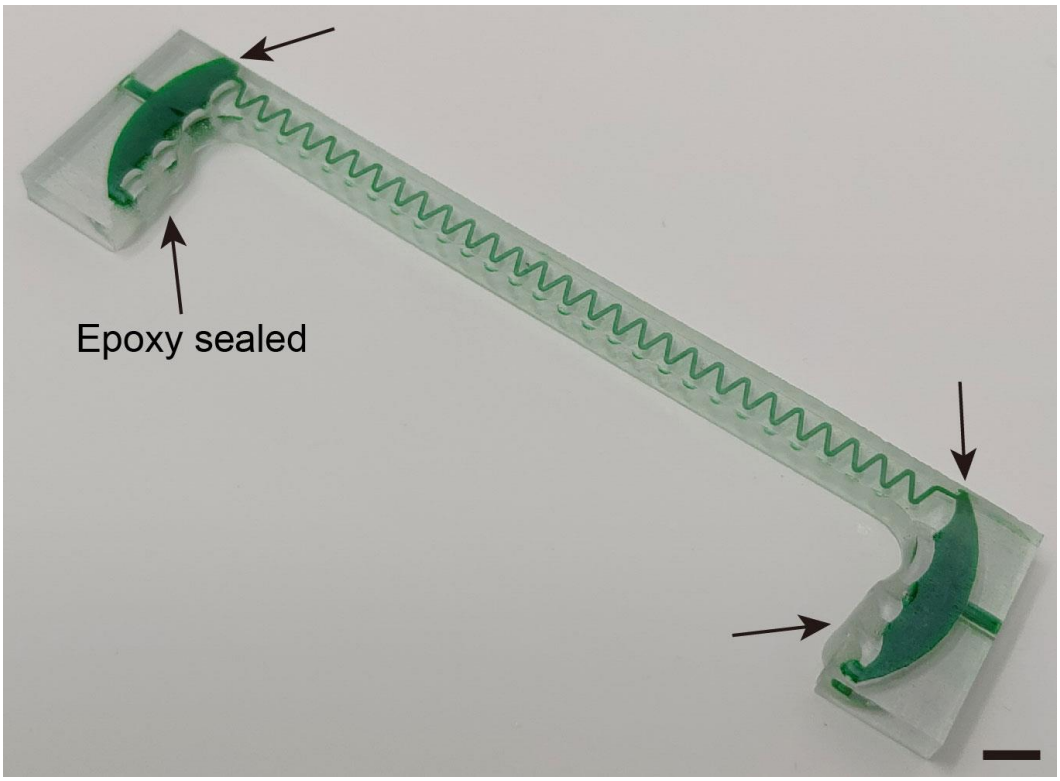

Figure 18: Testing of injection-based etching of uncured resin in an SLA-printed microchannel with a cross-sectional diameter of 600 µm.

In contrast, the centrifugal etching of the resin resulted in all microchannels down to the resolution-limit of the 3D-printer to be successfully cleared independent of fluidic resistances presented by individual microchannels in the geometry. Note that the 300 µm-diameter microchannel could not be printed in one of the studies due to resolution limit of the setup used (Viper Si2 3D-printer on Somos WaterClear Ultra 10122 resin).

In a similar comparative study, we investigated post-processing a complex geometry composed of a network of microchannels with different fluidic resistances when it was fabricated through inkjet printing. Specifically, we designed a vasculature-mimetic microfluidic device with a network of branching helical channels of varying sizes and printed using the ProJet 3510 HD printer. Across the device, the microchannel diameters

varied between 250 µm, 500 µm, 1000 µm, and 1500 µm with fluidic resistances (per length) ranging from 1.05×10^{11} Pa·s/m^4 to 1.36×10^{14} Pa·s/m^4 when filled with the liquified sacrificial wax at 65 °C. Similar to our studies on devices printed with SLA printing, our efforts to fully remove the sacrificial material from the microchannels failed when mineral oil was injected to the device. We observed that the mineral oil preferentially flowed through paths with wider channels with lower fluidic resistances and cleared out the sacrificial wax materials therein, leaving residual wax occluding the smaller channels with higher fluidic resistance (Figure 19).

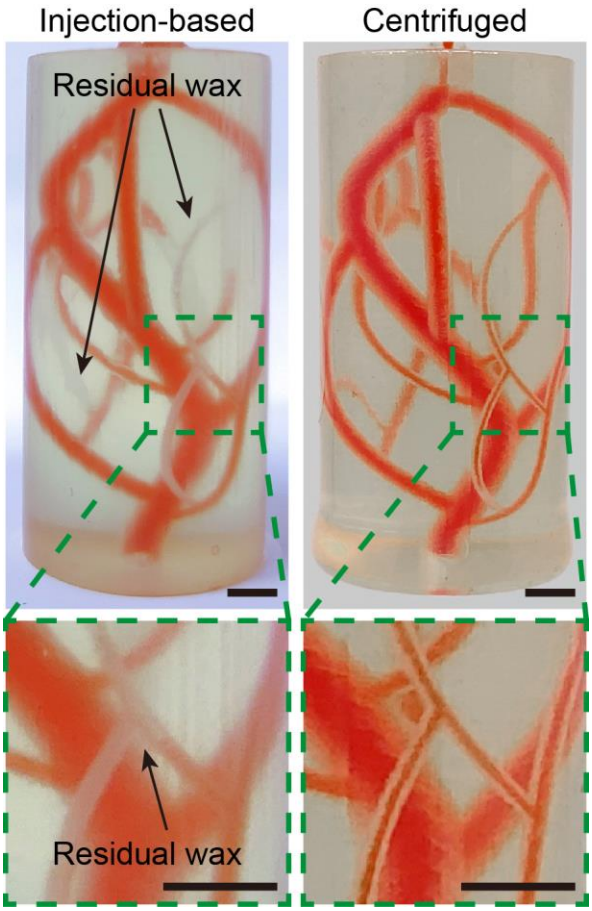

Figure 19: Photos of inkjet-printed 3D vasculature-mimetic microfluidic devices taken after they were subjected to injection-based (left) or centrifugal (right) etching.

When the same geometry was subjected to centrifugation, the device could be fully dewaxed and was free of occlusions when injected with a dye to test individual channels. Taken together, these results demonstrated the advantages of centrifugal etching of sacrificial materials in 3D-printed microchannels over the conventional method of injecting etching solutions in direct comparisons.

3.6 Summary

In summary, I have developed a technique that utilizes centrifugal forces to post-process 3D-printed microfluidic devices, so that sacrificial materials required for the printing process could later be efficiently and effortlessly discharged from microfluidic channels. Centrifugal forces driving etchants into microchannels act uniformly over the whole volume makes the process relatively agnostic to microchannel resistance variations, which facilitate efficient etching of high viscosity sacrificial materials not only from individual microchannels with high fluidic resistance but also from microchannel networks comprised of varying channel geometries. While 3D-printing offers attractive opportunities for microfluidic processes over conventional planar fabrication, its full potential can only be realized if the printed devices could be made functional through straightforward post-processing that does not negate the simplicity of 3D-printing. Therefore, the technique we introduced in this chapter can help expand the use of additive manufacturing in microfluidics and potentially impact applications that can uniquely benefit from 3D-printed microfluidic devices.

CHAPTER 4. NEGATIVE ENRICHMENT OF CIRCULATING TUMOR CELLS

Microfluidic devices that utilize immunoaffinity-based depletion methods offer high specificity enrichment of circulating tumor cells [45], [46]. For example, by targeting specific antigens that exist only on the tumor cells (e. g. EpCAM), only cells with the targeted antigen expression will be captured by the device [47]. Although immunoaffinity-based approaches that target the CTCs exhibit high specificity, due to the heterogeneity of the CTCs, these methods often lead to biased enrichment of the CTCs. Also, after the CTCs are captured by the device, it is often difficult to remove them from the device for further downstream assays without affecting their viability. Therefore, negative enrichment methods that eliminate the well-known peripheral blood cells instead of the CTCs allow intact CTCs to be released from the device while maintaining the specificity offered by the immunoaffinity-based approaches.

In the negative depletion method, WBCs are often removed by targeting their common antigen, CD45 [35], [36]. In conventional microfluidic devices for the negative enrichment of CTCs, WBCs are often pre-labeled with anti-CD45 conjugated magnetic particles and removed under a magnetic field gradient which increases the overall complexity of the system and takes away the portability advantage offered by the microfluidic devices [57]. Alternatively, the surface of the microchannels can be functionalized to capture the WBCs directly [58]. Still, due to the limited surface area offered by the conventional microfluidic devices, the large number of WBCs presented in the blood sample prevents clinically relevant volume of blood sample from being processed. Also, RBC lysing is often required, which increases the overall sample volume while prone to losing valuable CTCs during the process [60]. Therefore, a microfluidic

device with a large surface area is required to be able to effectively remove the large number of WBCs from the blood sample and achieve negative enrichment of CTCs.

In order to create a large surface area for the depletion of the WBCs, I utilized the centrifugal sacrificial material etching method that I have developed to create a 3D printed multi-layered microfluidic channel device with micropillar arrays in order to expand the functionalized surface area for accommodating large numbers of WBCs in milliliter blood volumes. Also, taking advantage of the cell size contrast between anucleated and nucleated cells, I embedded a 3 μm pore-size membrane filter in the device to retrieve the tumor cells from the leukodepleted blood sample and effectively remove the red blood cells and platelets. The combination of negative enrichment and filtration techniques prevents high concentration of WBCs from clogging the filter and enables the use of a smaller pore size filter to increase the retention rate of the enriched CTCs. I have also demonstrated the clinical feasibility of the device by processing a 10 mL of prostate cancer patient's blood sample and was able to observe the enriched CTCs on the membrane filter.

4.1 Device Design

Our microfluidic device is composed of two sections: a multi-layered immunoaffinity-based leukocyte capture section and a filtration section (Figure 20).

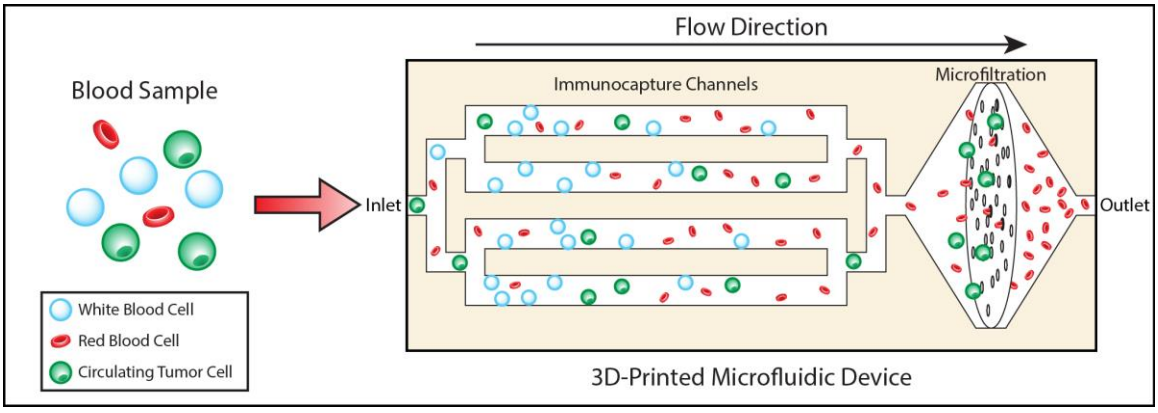

Figure 20: A schematic showing the tumor cell enrichment process in the device.

The device was designed with an overall dimension of 100 mm × 20.5 mm × 19.2 mm. The immunoaffinity capture section is composed of 4-32 stacked microfluidic layers, each with a footprint of a 20 mm × 67 mm. Microfluidic layers are designed to be 175 μm high and are arrayed in the vertical direction with a 475 μm-pitch (Figure 21).

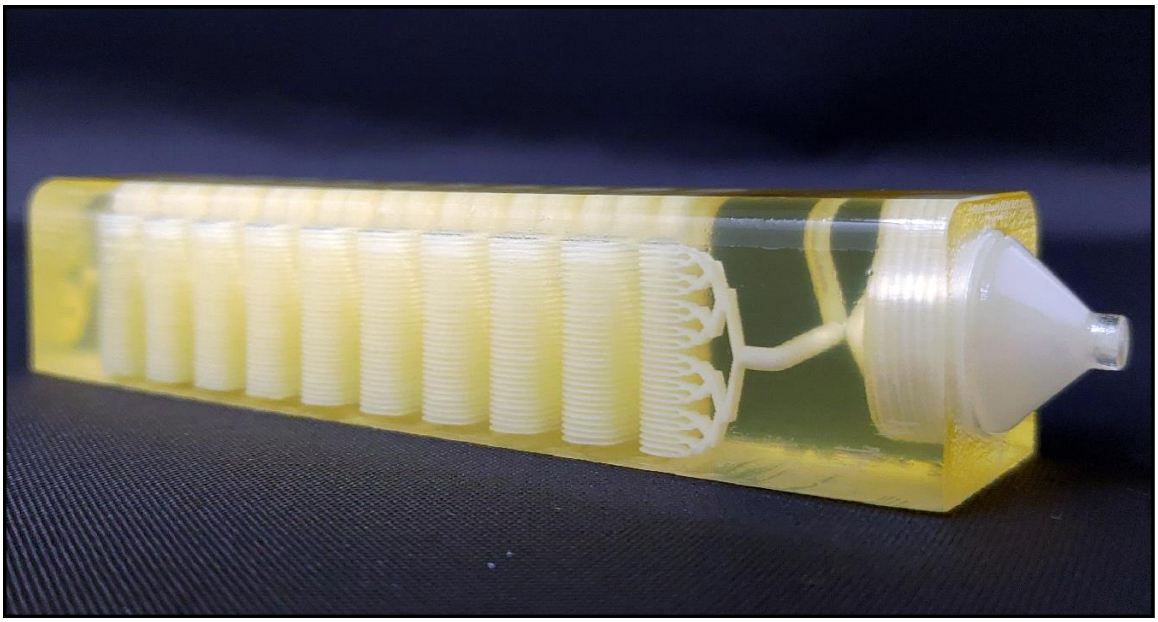

Figure 21: A photo of the 3D-printed device showing the microfluidic channels with 32 stacked microfluidic layers and the filter holder.

Inside the microfluidic layers, 200 µm-diameter microposts (1) increase the cell capture surface area (2) maximize the frequency of interactions between WBCs and the functionalized surface and (3) provide structural support between the stacked microfluidic layers to ensure the device integrity (Figure 22). Microposts are separated from each other by 200 µm and are shifted by 10 µm in each row to ensure interaction with WBCs that may follow different streamlines in laminar flow (Figure 22).

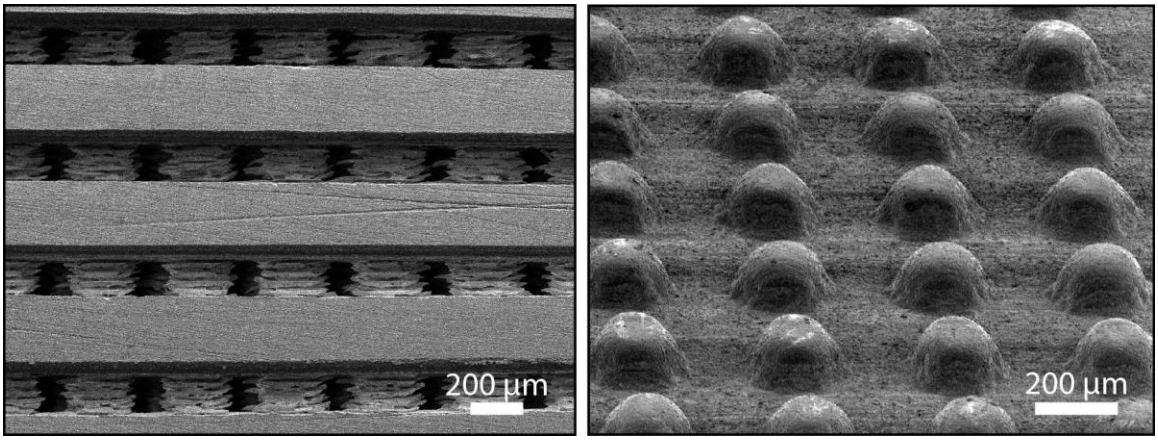

Figure 22: Scanning electron micrograph of the cross-section of the device showing 200 µm-diameter microposts within the microfluidic layers.

The filtration section of the device serves as a holder for a commercially available track-etched membrane filter with 3 µm-diameter pores and has a compartment with a threaded cap to facilitate straightforward installation and removal of the membrane filter (Figure 23).

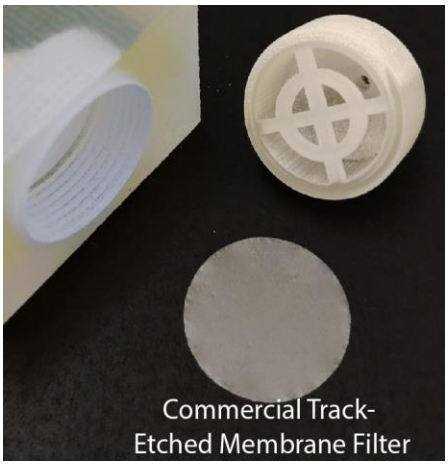

Figure 23: A photo of the 3D-printed device with the filter holder.

The integration of a commercial membrane filter into our device provides several advantages: First, potential cell loss due to sample handling during filtration is eliminated. Second, using commercially available membrane filters allows us to attain desired pore sizes that are well below a typical 3D printer resolution. Third, the removable membrane filter allows downstream analysis with a microscope or micromanipulation following the enrichment and on-chip staining of the tumor cells. Our device has two inlets, a sample inlet and a buffer inlet, which bypasses the immunodepletion section and is dedicated for washing the membrane filter. Through a network of 3D bifurcating microfluidic channels, the sample is first uniformly distributed into microfluidic layers for immunocapture and then recollected to pass onto the membrane filter. The filtrate (i.e., red blood cells, platelets and serum) along with wash buffer is then discharged from the waste outlet.

4.2 Device Fabrication and Assembly

A computer drawing of the microfluidic device was created using SolidWorks (SolidWorks Corp., Waltham, MA) in stereolithography (STL) file format. To reduce the file size, microposts were specifically drawn with hexagonal cross-section with the rationale that they would regardless be printed in a circular form due to the limited printer

resolution. The finished STL file was transferred to a ProJet 3510 HD 3D printer (3D Systems, Rock Hill, SC) and the device was printed in VisiJet® M3-X plastic material (3D Systems, Rock Hill, SC). The VisiJet® M3-X was chosen due to its favorable physical properties among other printable materials available from the vendor. Specifically, the VisiJet® M3-X has relatively low opacity and high rigidity (Young's Modulus = 2.168 GPa). Furthermore, the heat distortion temperature of the VisiJet® M3-X is 88 °C, which is well above the 65 °C melting temperature of the sacrificial wax support material (VisiJet® S300). In addition, the cost of the VisiJet® M3-X (~$5.7 per in3) is comparable to polydimethylsiloxane (PDMS) (~$4.6 per in^3) commonly used to build microfluidic devices with soft lithography. After the device was printed, the wax support material was etched using the centrifugal-etching method described in the previous chapter. The dewaxed channels were examined with a scanning electron microscope (SEM) to determine the printed feature size (Figure 22). The observed surface roughness in our device is due to the specific 3D printing technique (Inkjet 3D Printing) employed by the printer. Smoother surfaces could be obtained with a stereolithography-based 3D printer, which was not readily available for our use (Figure 24).

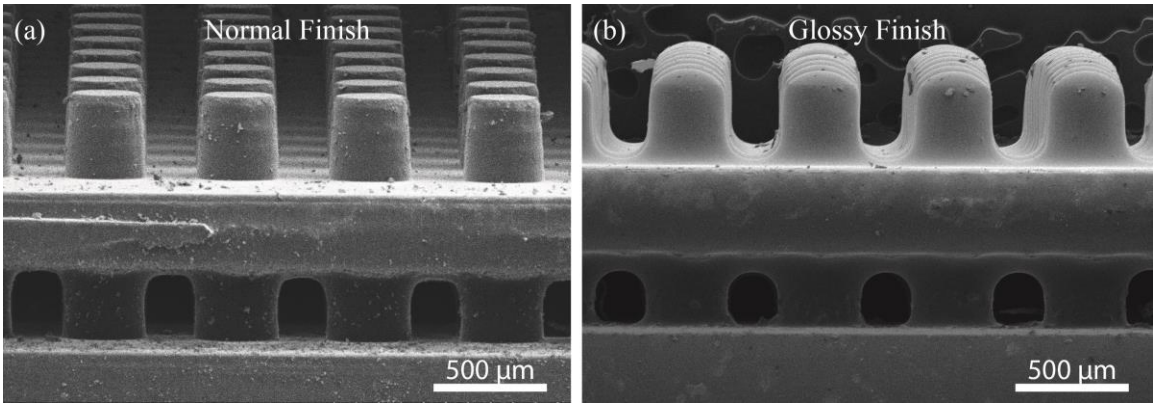

Figure 24: Scanning electron micrographs of the micropillars and microfluidic channels printed by an SLA 3D printer

In this work, the size of our device was limited by the size of the centrifugation tube for dewaxing. While we used a proof of principle device with 32 stacked microfluidic layers for our experiments, the printing and dewaxing process we developed could easily be scaled to print devices with higher complexity (Figure 25).

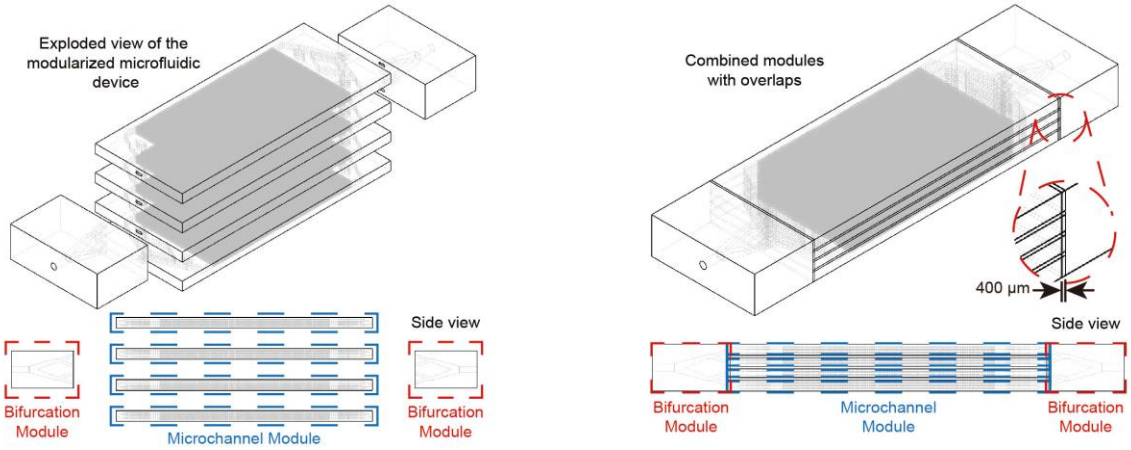

Figure 25: The device with 16 stacked microfluidic layers was divided into different modules and reassembled with overlaps between the modules during the 3D printing process.

4.3 Surface Functionalization and Characterization

To specifically capture WBCs, we functionalized the printed microfluidic channels through a modified version of the functionalization protocol developed by Stott et al. [43] Specifically, the microfluidic channels were first treated with 3-mercaptopropyl-trimethoxysilane (MPTMS) (Gelest, Morrisville, PA) mixed with 200 proof ethanol (Thermo Fisher Scientific, Waltham, MA) at 4% v/v ratio. Following 1 h incubation at room temperature, channels were washed with ethanol. Next, a stock solution of N-y-maleimidobutyryloxy succinimide ester (GMBS) (Pierce Biotechnology, Rockford, IL) in dimethyl sulfoxide (DMSO) (Pierce Biotechnology, Rockford, IL) was prepared at a final concentration of 100 mg mL^{-1}. The device was incubated with 0.28% v/v of GMBS stock

solution in ethanol for 30 minutes at room temperature. Residual GMBS was then removed with an ethanol flush and the device was rinsed with phosphate buffered saline (PBS) (Corning Inc., Corning, NY). Next, a 10 µg mL^{-1} solution of NeutrAvidin (Pierce Biotechnology, Rockford, IL) in PBS was introduced into the device. Following 1 h incubation, the protocol was completed by washing the functionalized device with PBS (Figure 26).

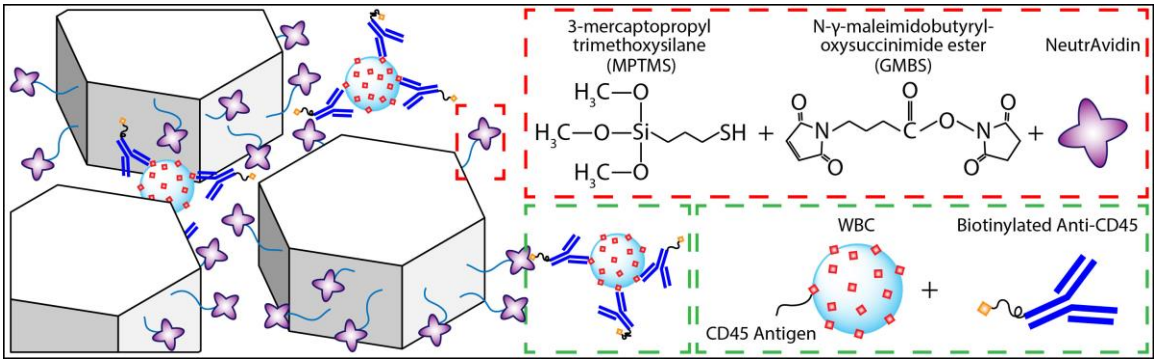

Figure 26: Functionalization protocol of the 3D printed device.

To characterize the surface chemistry following the functionalization process, we used X-ray photoelectron spectroscopy (XPS) and fluorescence microscopy. We first verified the attachment of MPTMS molecules with XPS by measuring the amount of sulfur, which is part of the MPTMS molecule. The presence of the sulfur peak from the scan of the coated sample, while no peak could be observed for the uncoated sample, verified the successful coating of the MPTMS on the 3D-printed material (Figure 27).

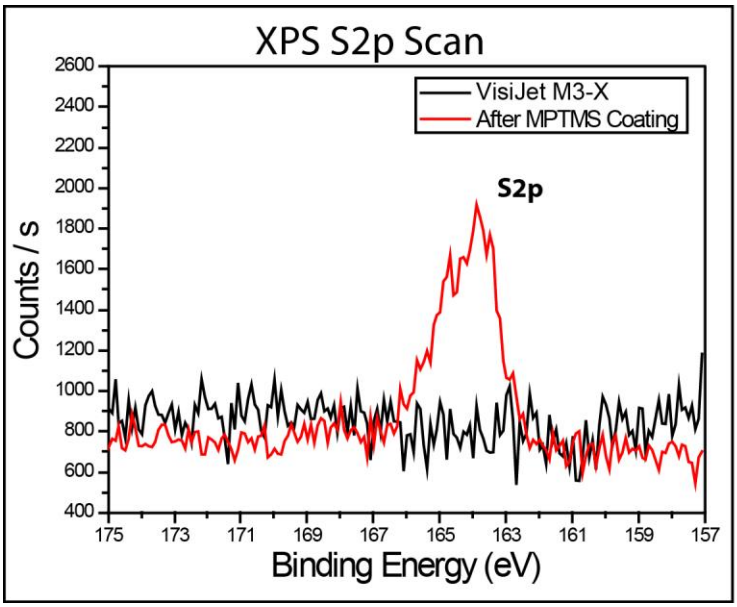

Figure 27: Results from the XPS scan of sulfur on the surface of VisiJet® M3-X material before and after the coating of MPTMS.

To validate the GMBS attachment to the MPTMS, sole use of XPS was not as effective because the GMBS and VisiJet® M3-X material both contained nitrogen, oxygen, and carbon. Therefore, we used fluorophore-conjugated reagents to investigate the GMBS coating and the subsequent functionalization steps. In this process, a section of the 3D-printed material was first selectively coated with MPTMS and GMBS and then FITC-conjugated NeutrAvidin (Thermo Fisher Scientific, Waltham, MA) was applied to the entire surface and washed thoroughly with PBS. Fluorescence signal differentially observed at the MPTMS-coated section compared to the bare sample demonstrated the specific attachment of GMBS to the surface-bound MPTMS. Following a similar process, we also verified specific binding of the Atto 610-conjugated biotin (Sigma-Aldrich, Saint Louis, MO) to the NeutrAvidin on the 3D-printed surface (Figure 28).

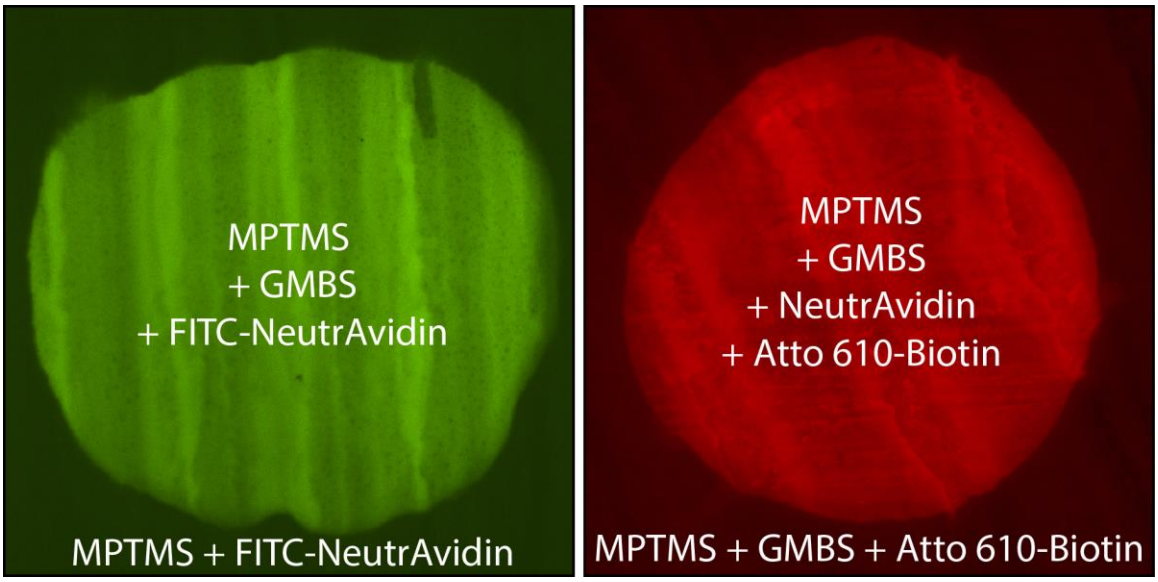

Figure 28: NeutrAvidin (FITC) and biotin (Atto 610) on chemically modified VisiJet® M3-X material.

4.4 Characterization of White Blood Cell Immunocapture

To investigate immunodepletion in our device, we used both CD45+ cell lines and whole blood samples. For cell line experiments, CD45+ Jurkat Clone E61 (ATCC® TIB152TM) cells were cultured according to the instructions provided by the manufacturer. Cells were incubated in an RPMI 1640 medium (Corning, Corning, NY) mixed with 10% fetal bovine serum (FBS) (Corning, Corning, NY) at 37 °C in a 5% CO2 ambient. A seeding density >1 × 105 cells per mL was used in subcultures to ensure optimum growth rate. When cells reach 80% confluency, they were stained with CellTracker^{TM} Orange CMRA dye (Molecular Probes, Eugene, OR) according to the protocol provided by the company and resuspended in PBS to reach a final concentration of 7×10^6 cells per mL, to mimic the WBC concentration in blood.

For the device characterization, blood was withdrawn from consenting healthy donors according to the protocol approved by the Georgia Institute of Technology Central Institutional Review Board. For the patient blood sample, the blood was collected after consenting the patient according to the protocol approved by the Emory University Institutional Review Board. All experiments with blood samples were approved and performed in compliance with the institutional guidelines of the Georgia Institute of Technology Central Institutional Review Board. All blood samples were collected in tubes with ethylenediaminetetraacetic acid (EDTA). Following a complete blood count, blood samples were incubated with 500 fg per WBC of biotinylated mouse anti-human CD45 antibodies (SouthernBiotech, Birmingham, AL) for 20 minutes on a rocker to label the WBCs with biotin (Figure 26).

The immunocapture efficiency of the chip was calculated by comparing the concentration of target cells in the sample and in the product with a fluorescence microscope. For whole blood samples, Turk's blood diluent (Azer Scientific, Morgantown, PA) was mixed with the product at 10:1 v/v ratio to both lyse the RBCs and stain the nuclei of WBCs for accurate quantification. The number of cells in the product were counted on a Nageotte Chamber (Hausser Scientific, Horsham, PA) using a fluorescence microscope (Nikon Eclipse Ti-E).

4.5 Measurement of Tumor Cell Enrichment

To investigate the tumor cell enrichment with our device, we prepared simulated samples by spiking cultured tumor cells into whole blood. Ovarian cancer cell line HeyA8, human breast cancer cell line MDA-MB-231 (ATCC® HTB-26™) and prostate cancer cell

line LNCaP (ATCC® CRL-1740™) were cultured according to the manufacturer-provided protocols. HeyA8 and LNCaP cells were grown in RPMI 1640, while Dulbecco's Modified Eagle's medium (DMEM) (Corning, Corning, NY) was used to culture MDA-MB-231 cells. All cultures were supplemented with 10% FBS and incubated in 5% CO2 atmosphere at 37 °C. Cells were subcultured every 2 - 4 days depending on the confluency levels. Prior to spiking, cultured cells were stained with CellTracker™ Orange dye to facilitate optical detection in the final product. Tumor cells were spiked (at a concentration of $3 \times 10^3 – 4 \times 10^3$/mL) into blood withdrawn from healthy donors according to the IRB-approved protocol. Prepared blood samples were stored in EDTA tubes until they were processed through the device within 4 h of phlebotomy.

To calculate the tumor cell enrichment factor, we compared the tumor-cell-to-WBC concentration ratio of the sample and the product. To count WBCs and tumor cells in the product, filter-retained cells were immunostained following the blood processing and washing steps. In addition to the nuclear stain with Hoescht 33342 (Thermo Fisher Scientific, Waltham, MA), FITC-conjugated NeutrAvidin was used to label the WBCs that were prelabeled with biotin. After staining, the filter was carefully removed from the filter holder compartment of the device, transferred onto a glass slide and cells are counted with a fluorescent microscope. The viability of tumor cells was determined using 0.4% trypan blue (Thermo Fisher Scientific, Waltham, MA) and live/dead cell assay (ab115347) (Abcam, Cambridge, UK) according to the manufacturer-suggested protocol.

4.6 Optimization of Surface Functionalization with Cell Lines

To test the immunocapture in our device, we initially used Jurkat cells with known CD45 expression as a model system. This allowed us to determine the target cell capture efficiency in the absence of steric effects due to RBCs (Figure 29).

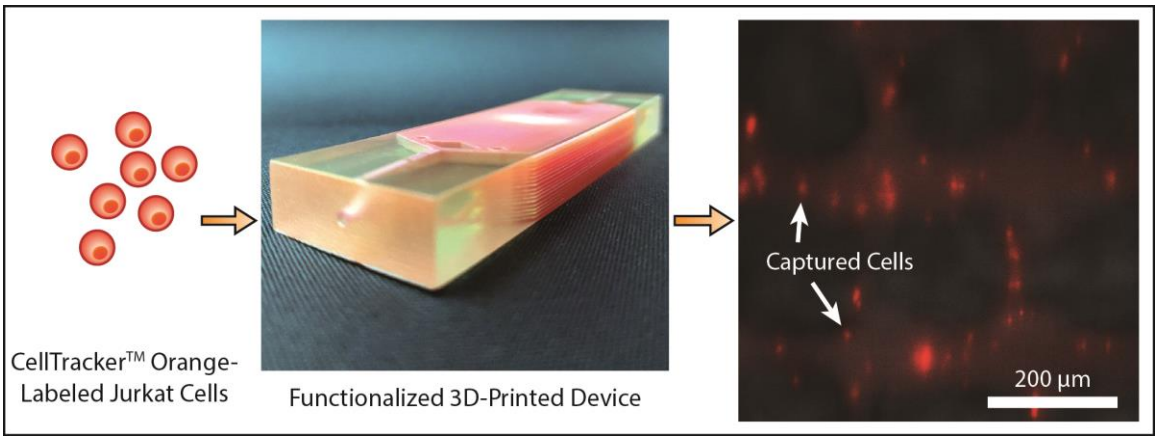

Figure 29: Procedure used to test Jurkat cell immunocapture.

We tested two different strategies for the cell capture. In the first scheme, we functionalized the device surface with the anti-CD45 antibody (10 µg mL^{-1}) and captured the cells through antibody-antigen interaction. In the second scheme, we labeled Jurkat cells with biotinylated anti-CD45 antibody (500 fg per Jurkat cell) and captured the cells on NeutrAvidin-coated channels via stronger avidin-biotin interaction. To compare the two strategies, we processed matched samples at controlled flow rates (0.125-2.5 mL h^{-1} per layer) and calculated the capture efficiency by counting the fluorescently labeled cells in the product versus the input. Overall, tagged Jurkat cells were found to be captured with higher efficiency (Figure 30).

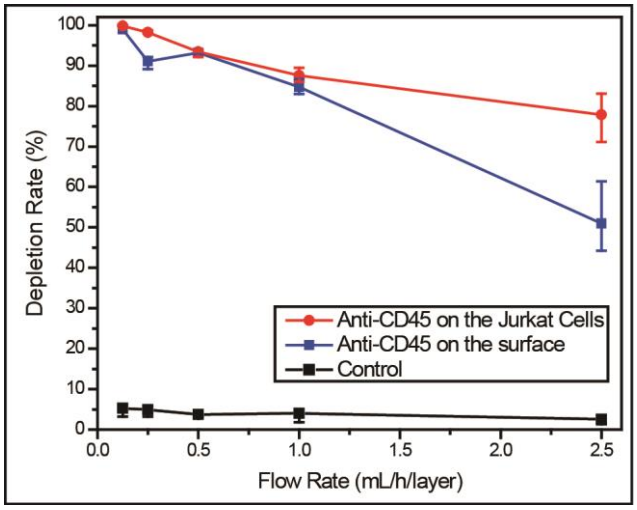

Figure 30: Jurkat cell depletion rate as a function of the sample flow rate for labeled (red curve) and non-labeled (blue curve) Jurkat cells.

In both functionalization strategies, >99% of the Jurkat cells were captured at a low sample flow rate (125 µL h^{-1} per layer) and virtually no cells could be observed in the product. In contrast, a large concentration of non-captured Jurkat cells was observed in the product processed at a high sample flow rate (2.5 mL h^{-1} per layer) (Figure 31).

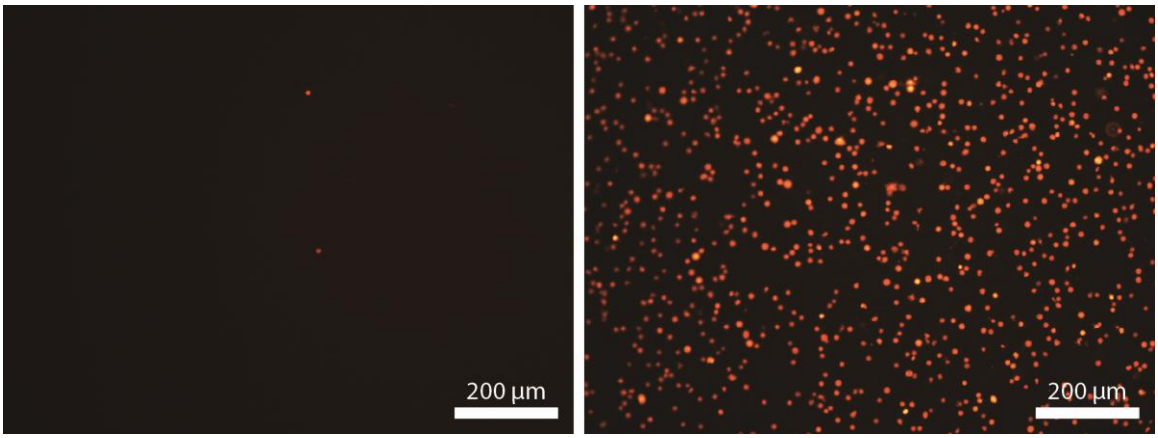

Figure 31: Representative fluorescence images of the non-captured cells collected in the product.

Furthermore, even though ~90% of Jurkat cells could be captured for both strategies at sample flow rates below 1 mL h^{-1} per layer, the capture efficiency for labeled Jurkat cells was significantly higher for the faster sample flow rate (2.5 mL h^{-1} per layer) (Figure 30).

Based on results from experiments with Jurkat cells, biotin-labeling of target cells was chosen as the functionalization strategy for blood samples. Besides providing higher immunocapture efficiency, biotin-labeling of target cells is also more practical as it reduces the antibody consumption considering the large device surface that needs to be coated otherwise.

To ensure against potential cytotoxicity of our device on tumor cells, we tested tumor cell viability after they were processed on our device. Using the live/dead assay we observed no notable difference on the viability of MDA-MB-231 tumor cells before and after processing with the 3D-printed device (Figure 32).

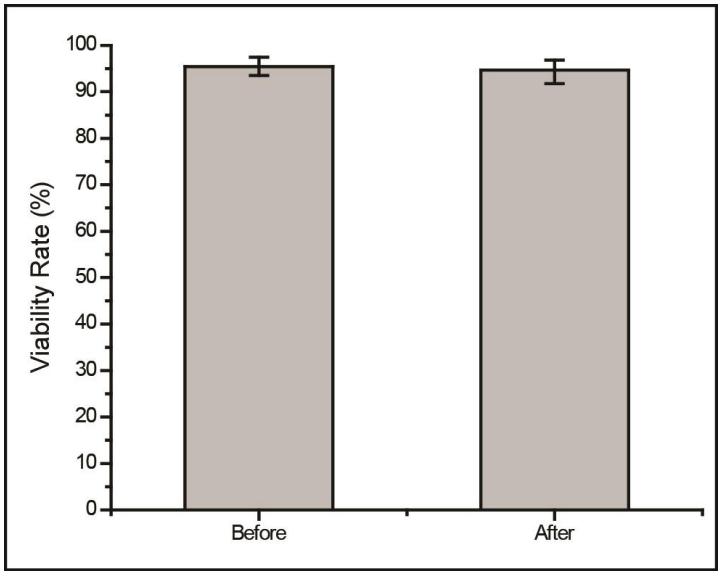

Figure 32: Cell viability before and after processing through the 3D printed device.

4.7 Immunodepletion of Leukocytes from Whole Blood

We processed whole blood samples collected from consenting healthy donors to characterize immunodepletion performance under different operating conditions (Figure 33).

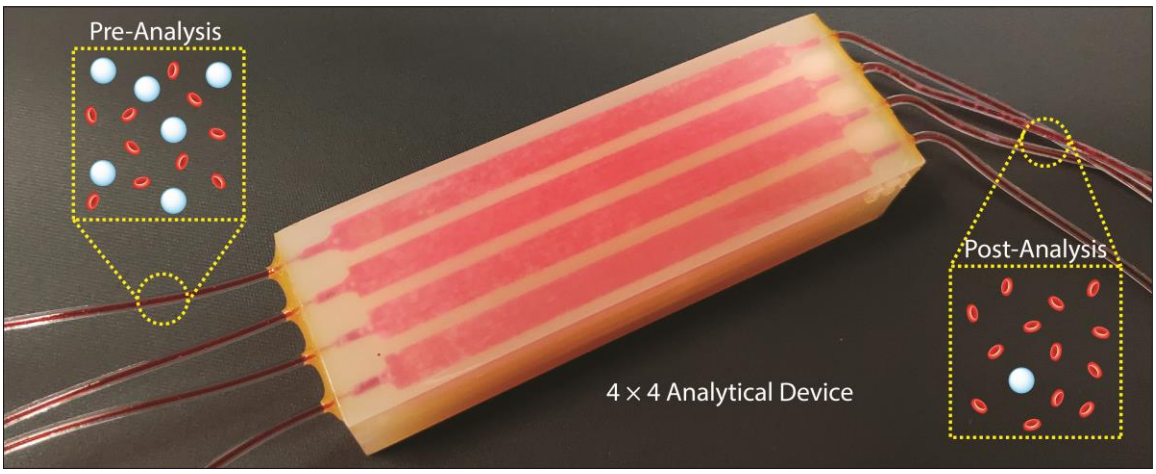

Figure 33: A photo of the analytical device equipped with 16 (4 × 4) smaller versions of the full device for testing the WBC immunocapture efficiency with whole blood samples.

In these experiments, 200 µL blood/layer were processed and WBCs were captured by targeting their CD45 antigen, which is expressed by virtually all WBCs at varying levels. In agreement with the previous studies [59], we found WBC capture rate from whole blood to be lower than Jurkat cells due to steric effects by other blood cells. While RBCs can be lysed to improve WBC capture rate, we chose to optimize our device for processing whole blood samples with the goal of minimizing upstream sample manipulation that may introduce cell loss.

To optimize the functionalization process, we first measured the WBC capture efficiency at different antibody concentrations for labeling WBCs. We found that

increasing the biotinylated anti-CD45 antibody concentration improved the cell capture efficiency only up to a certain point. Higher biotinylated anti-CD45 antibody concentration led to free biotin competing with WBCs for NerutrAvidin binding sites on the device and resulted in lower WBC capture efficiency (Figure 34). The optimal concentration of biotinylated anti-CD45 antibody per WBC was found to be 500 fg per WBC, which was used for the subsequent experiments.

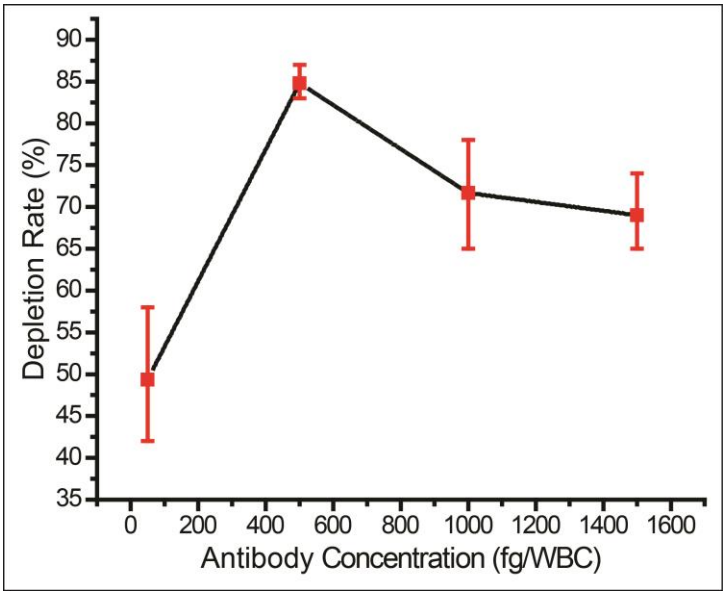

Figure 34: Measured whole blood WBC immunocapture rates as a function of the biotinylated anti-CD45 antibody concentration used per WBC.

Next, we characterized the device performance under different flow rates to optimize the device operating conditions. As expected, the WBC immunocapture efficiency decreased with higher sample flow rate (Figure 35). Differently, we can prioritize the capture rate over the throughput in this typical trade-off, as our scalable approach allows the sacrifice in the flow speed to be compensated by parallel running microfluidic layers to achieve a desired sample processing rate. Also considering an

excessively low flow speed will lead to non-specific cell attachment and cell sedimentation, we chose 0.5 mL h^{-1} per layer, where ~83% of the WBCs were captured, as the optimum flow rate.

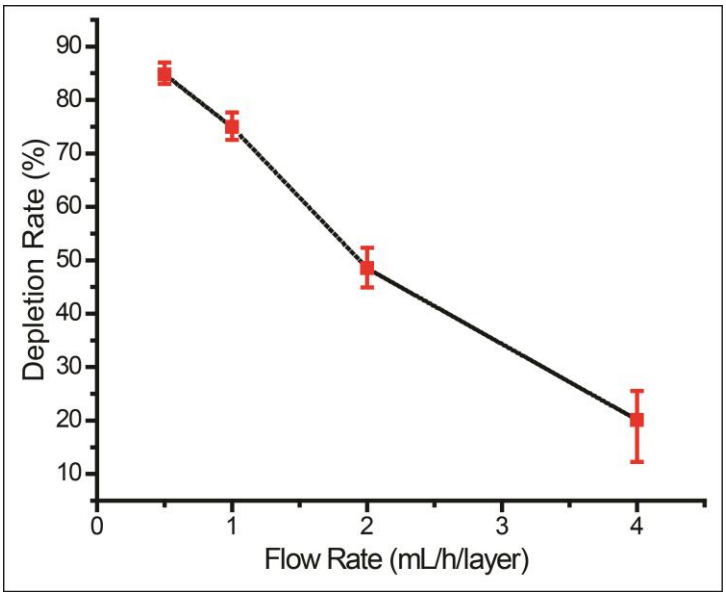

Figure 35: Measured whole blood WBC immunocapture rates as a function of the sample flow rate.

We also explored different channel geometries to increase the WBC capture rate from whole blood. Because our feature size was already at the limit of the 3D printer, we extended the channel length through 3D serpentine geometries. We found that by doubling the channel length from 6 cm to 12 cm, the depletion rate for WBCs increased from ~83% to ~92% (Figure 36). Further increases in the channel length to 24 cm and 48 cm produced tapering WBC depletion rates of ~95% and ~96%, respectively and demonstrated a limit for depletion rate enhancement that can be achieved by channel length increases alone.

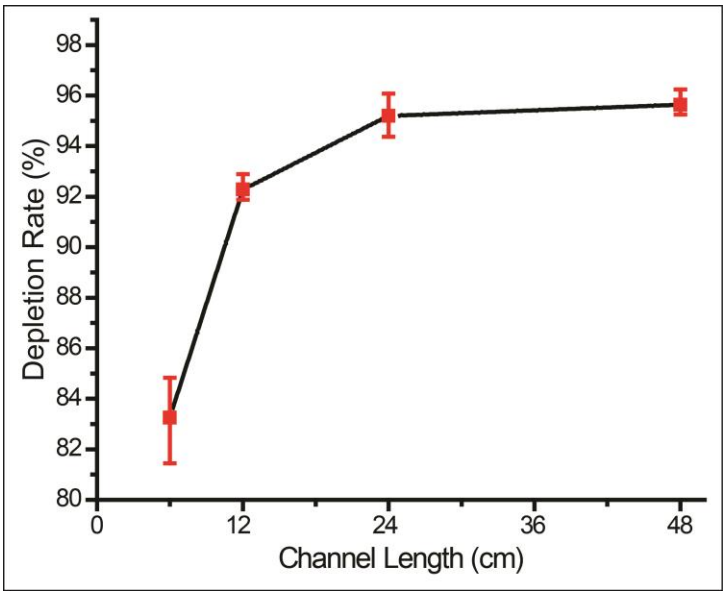

Figure 36: Measured whole blood WBC immunocapture rates as a function of the microfluidic channel length.

To investigate the effect of surface saturation on the device performance, we measured cell capture efficiency as a function of processed sample volume. Our device was designed such that immunocaptured WBCs from 550 µL of whole blood per layer will occupy ~10% of the total active surface area. In agreement with our calculations, we observed that at low sample volumes (200 - 400 µL per layer), the WBC depletion rate remained at ~85%, while there was a noticeable decrease in the WBC depletion rate for processing larger sample volumes (800 and 1600 µL per layer) (Figure 37). These results showed the importance of providing a substantial capture surface area for the efficient depletion of a large number of WBCs in a blood sample and effectively validated our enrichment approach.

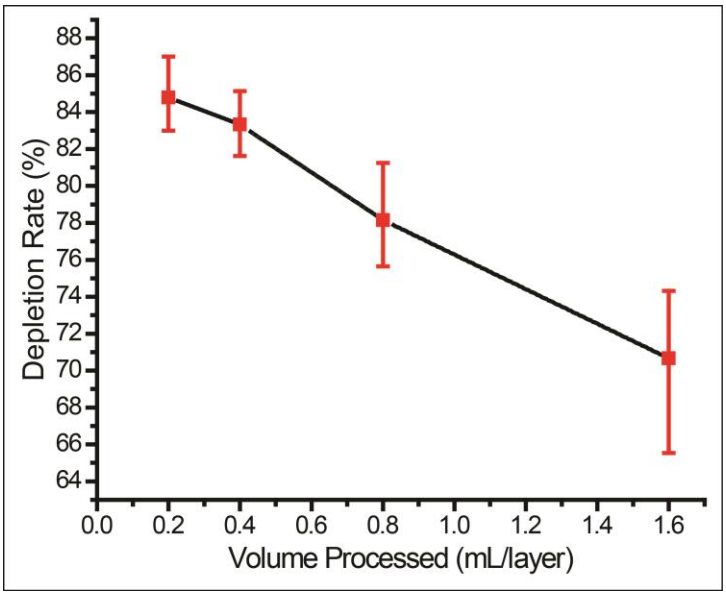

Figure 37: Measured whole blood WBC immunocapture rates as a function of the processed whole blood volume per microfluidic layer.

4.8 Removal of RBCs and Platelets from Whole Blood

To remove the remaining blood cells following the depletion of WBCs, we used filtration. Considering the significant size contrast between nucleated and anucleated cells in the blood, we chose a filter with a 3 µm-pore diameter to ensure against tumor cell loss. Furthermore, filtration-based CTC enrichment technologies typically use larger pore size (5-10 µm) filters with high CTC recovery rates (>90%), and therefore, we thought a 3 µm membrane filter should minimize potential CTC loss in post-filtration. Through spiked cell experiments, we characterized a commercial 3 µm-pore membrane filter (Whatman plc, Maidstone, United Kingdom) separately from our 3D-printed device. In our experiments, we processed 200 µL aliquots of whole blood samples each spiked with ~4 × 10^3 fluorescently labeled MDA-MB-231 breast cancer cells per milliliter of blood under different filtration pressures. Filtration pressure was set by pneumatically introducing a

diluting buffer (PBS) into the filter holder, while the blood was concurrently driven by a syringe pump at a flow rate of 2 mL h^{-1}. Under low buffer pressure (<50 mbar), the filter got clogged due to RBCs not being cleared efficiently and eventually forming a cake layer on the filter (Figure 38). In contrast, we achieved a clog-free operation at buffer pressures of 50 mbar and higher with no visible caking of RBCs on the filter.

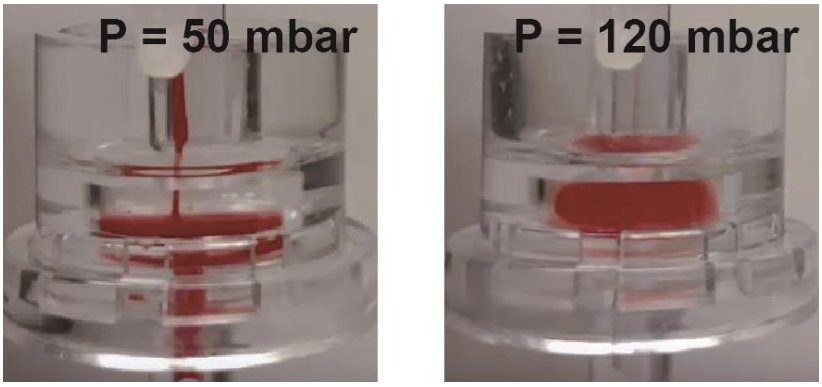

Figure 38: Images of a 3 µm-pore membrane filter operated under different buffer pressures to recover spiked cancer cells from whole blood.

To optimize the filter operating conditions for maximizing tumor cell enrichment, we measured retention rates for both tumor cells and WBCs. For retention rate measurements, WBCs on the filter were immunostained with a color different than pre-labeled tumor cells and counts for both cells were compared with the original counts at the inlet (Figure 39).

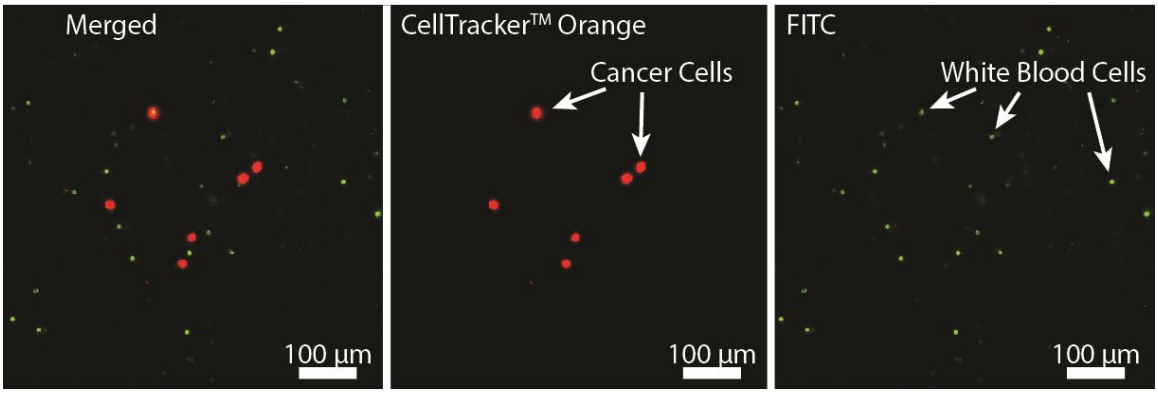

Figure 39: Fluorescence microscope images of nucleated cells retained on the filter.

Among different buffer pressures tested, 120 mbar was determined to deliver optimum results such that virtually all tumor cells, as well as ~81% of WBCs, were retained on the filter (Figure 40). At 50 mbar, partial caking on the filter led to a pressure build-up and tumor cell loss. At the high end, pressures >120 mbar did not change the tumor cell retention rate notably but resulted in a lower WBC retention rate indicating a higher stress on retained cells.

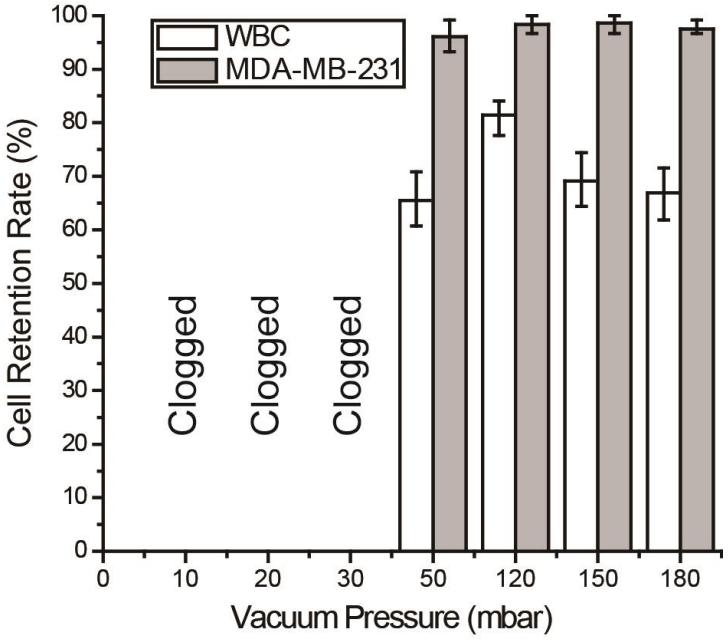

Figure 40: Measured retention rates for both spiked MDA-MB-231 breast cancer cells and the WBCs under different vacuum pressures.

The viability of the tumor cells, retained on the filter under 120 mbar, was measured using live/dead assay and no notable effect was observed (Figure 41).

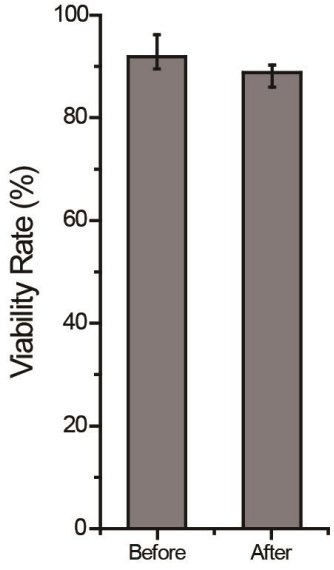

Figure 41: Measured MDA-MB-231 tumor cell viability rate before and after processing through the membrane filter under 120 mbar.

Moreover, an analysis of the WBC cell size in the filtrate collected at 120 mbar showed that cells with >8 µm diameter are not likely to squeeze through the pores (Figure 42).

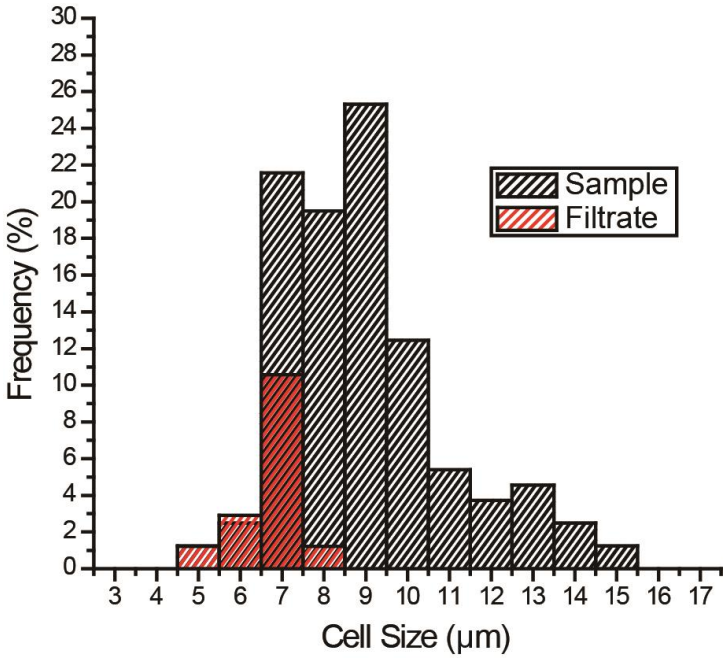

Figure 42: Measured cell size distribution of the WBCs in the sample and the filtrate at 120 mbar vacuum pressure.

Compared to WBCs ranging in size from 5 to 15 µm in the blood sample, WBCs passing through the 3 µm-pore size filter ranged between 5 to 8 µm. In addition, virtually all (~96%) of 8-µm diameter WBCs and half (~52%) of 7-µm diameter WBCs were retained on the filter. Therefore, we concluded the size range of cells that could pass through the 3 µm-pore membrane filter overlaps with the reported CTC size range only for very small CTCs. Having said that, we believe post-filtration cell loss can further be reduced by employing a smaller pore size and through further optimization of the processing conditions.

4.9 Circulating Tumor Cell Enrichment from Patient Blood Sample

Combining the immunoaffinity based WBC depletion and post-filtration processes that were separately characterized, we tested a 3D-printed microfluidic device with an embedded micropore filter. In assembling the final device, previously characterized 3 µm-pore size commercial filter was placed in the dedicated filter holder printed as part of the microfluidic device and sealed with an O-ring to prevent leakage. The device was operated under previously identified optimal conditions. Specifically, the blood sample was premixed with 500 fg per WBC biotinylated anti-CD45 antibody, driven at a flow rate of 0.5 mL h^{-1} per layer using a syringe pump and with a blood volume of ~300 µL per layer and PBS was supplied from the dedicated buffer inlet of the 3D-printed device and driven under 120 mbar vacuum by an electronic pressure regulator. Because the buffer line bypassed the immunocapture chambers within the device and directly drained onto the membrane filter, it did not interfere with the WBC depletion process (Figure 43). Moreover, driving the blood sample via syringe pump served two purposes: First, the sample flow rate, which is crucial for the immunocapture, could be kept constant independent of pressure fluctuations in the filtration section. Second, any potential backflow from the pneumatically driven filtration section into the immunocapture was eliminated.

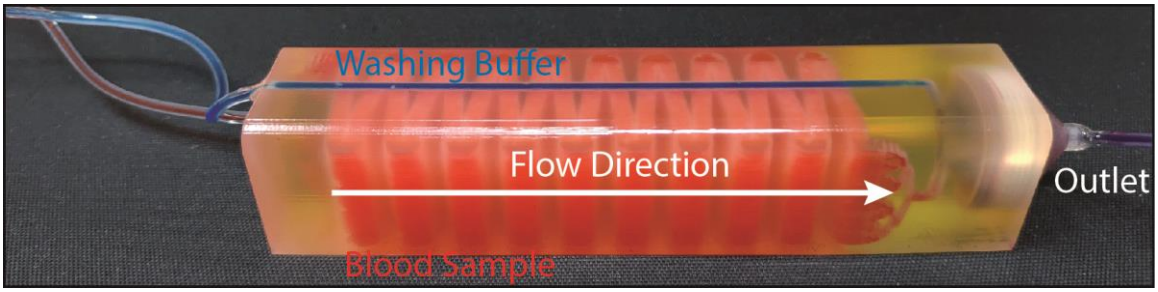

Figure 43: A photo of the full 3D-printed device.

We first processed simulated blood samples spiked with fluorescently labeled tumor cells to characterize the performance of our system. To calculate enrichment factors, the product (i.e., cells retained on the filter) was post-stained for WBC and nuclear markers and imaged using fluorescence microscopy (Figure 44).

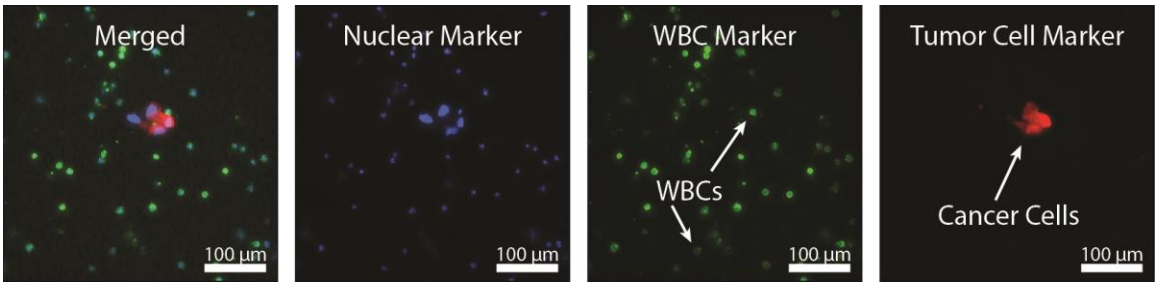

Figure 44: Fluorescence microscope images of the nucleated cells retained on the membrane filter.

To demonstrate the antigen-agnostic enrichment of tumor cells from whole blood, we used cancer cell lines of different cancers, namely breast (MDA-MB-231), prostate (LNCaP) and ovarian (HeyA8) cancers. For all cancer cell types tested, we achieved a ~90% tumor cell recovery rate (Figure 45).

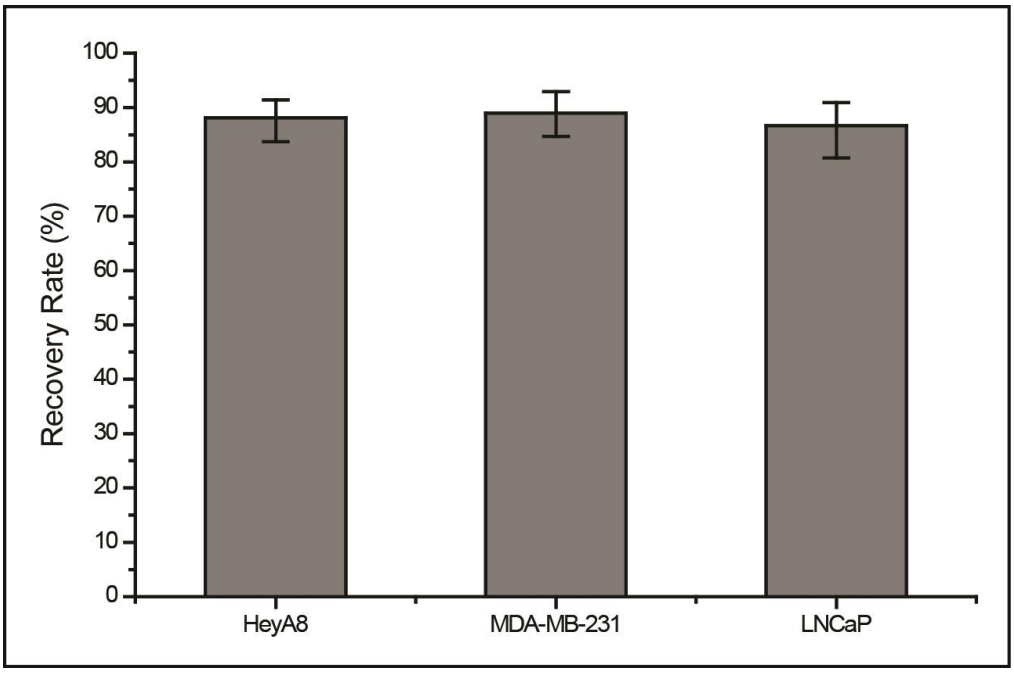

Figure 45: Measured recovery rates for cancer cells spiked into whole blood samples.

The cell loss was found to be due to non-specific adhesion and/or retention of tumor cells in the immunocapture channels from control experiments and can potentially be lowered with optimized blocking protocols and by using different 3D printing techniques and materials (Figure 46).

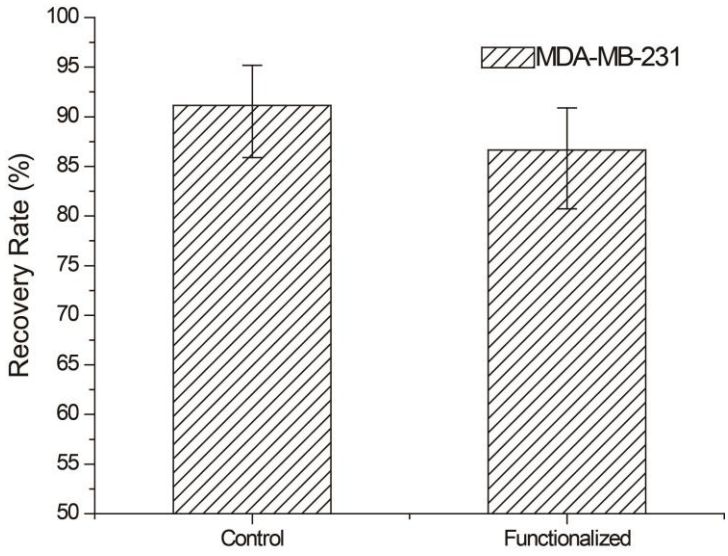

Figure 46: MDA-MB-231 cancer cell recovery rate in the immunocapture channels with and without surface functionalization.

To demonstrate the feasibility of employing our device for clinical samples, we designed a device for large-volume blood samples and processed a sample collected from a consenting prostate cancer patient according to an IRB-approved protocol. For the clinical sample, we printed a device with 32 immunodepletion layers, each in the form of serpentine channels with an effective path length of ~40 cm (Figure 43). Based on the previously measured 96% leukodepletion and ~80% membrane retention rates, we estimated ~60% of pores on the 13 mm-diameter membrane filter to be eventually clogged with a WBC while processing a 10 mL blood sample with a WBC concentration of 5 million cells per mL. Following the processing of 10 mL of patient whole blood sample on our device, the cells on the filter were first fixed with 4% paraformaldehyde (PFA) (Electron Microscopy Sciences, Hatfield, PA), permeabilized with 1% Nonidet-P40 (Thermo Fisher Scientific, Waltham, MA), and post-stained on the filter with their respective markers. Cytokeratin 8/18 (Invitrogen, Carlsbad, CA) and prostate specific

antigen Kallikrein 3 (PSA/KLK3) (Cell Signaling, Danvers, MA) were used to label the prostate tumor cells with Alexa Fluor 488 (Invitrogen, Carlsbad, CA) while anti- CD45 (BD Biosciences, San Jose, CA) and anti-CD66b (Biolegend, San Diego, CA) were used to label the WBCs with Alexa Fluor 594. The nuclei of both prostate tumor cells and WBCs were stained with DAPI (Invitrogen, Carlsbad, CA). The recovered prostate tumor cells were identified on the filter with fluorescence microscopy (Figure 47).

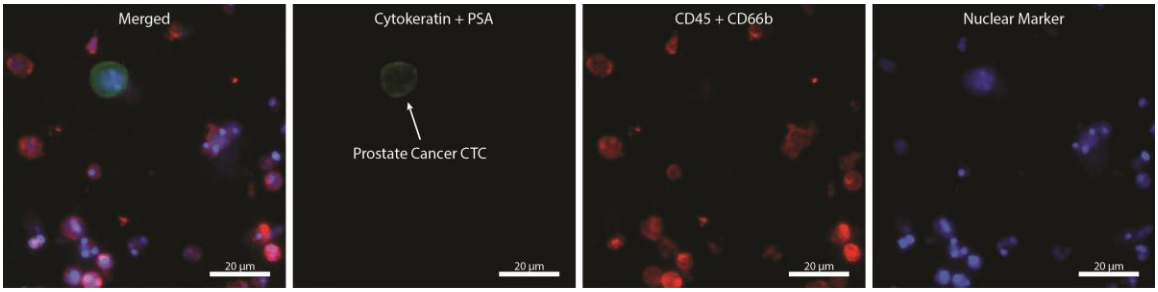

Figure 47: Fluorescence microscope images of the prostate cancer CTC retained on the membrane filter.

4.10 Summary

Depletion of WBCs from blood allows antigen-agnostic and unbiased enrichment of tumor cells. We have developed a monolithic 3D microfluidic device combining immunodepletion and post-filtration for negative enrichment of CTCs directly from whole blood. Taking advantage of the design flexibility afforded by the 3D printing, we created stacked microfluidic layers with an immunocapture surface, large enough to accommodate millions of WBCs from clinically relevant volumes of blood. Post-filtration of leuko-depleted blood within the same device allowed us to retain all nucleated cells, including residual WBCs on a detachable membrane filter, which enabled effortless removal of viable tumor cells off the chip for downstream assays.

CHAPTER 5. LABEL-FREE NEGATIVE ENRICHMENT OF CTC VIA A 3D-PRINTED MICROFLUIDIC DEVICE WITH IMMUNO-ENHANCED MICROFILTRATION

Although I have demonstrated the clinical feasibility of the developed 3D microfluidic device for the negative enrichment of CTCs from a clinically relevant volume of prostate patient's blood sample, there was still room for improving of the device. First, the WBCs in the blood sample were pre-labeled with biotinylated anti-CD45 antibody, which takes away the label-free aspect that we were trying to achieve. Second, there was still a relatively high number of WBC contamination on the membrane filter after the enrichment process, which can cause problems during the micromanipulation of the CTCs for any further downstream assays. To overcome these issues, modifications to the developed 3D microfluidic device are needed to achieve true label-free enrichment of CTCs while reducing the number of WBC contamination in the final product.

In order to achieve label-free enrichment of the CTCs using the 3D microfluidic device, I modified the functionalization protocol to directly label the inner surfaces of the leukodepletion channels with antibody that specifically binds to a WBC-specific membrane antigen for the capturing of the non-labeled WBCs. Also, to increase the capture efficiency of the WBCs, I employed the use of immuno-enhanced microfiltration that can be simultaneously functionalized during the functionalization of the leukodepletion channels, which simplifies the functionalization process and capture the residual WBCs that bypass the leukodepletion channels chemically. The enriched, concentrated label-free CTCs can then be released from the device with a revere flow, making them compatible

with immunocytochemical, molecular, and functional studies downstream. I first optimized the device operational conditions of the immune-enhanced microfiltration with spiked-cell experiments. I then applied it in the 3D-printed device with clinical samples collected from patients with pancreatic and prostate cancers to demonstrate the clinical utility of the full device. I was able to successfully observe the enriched CTCs from the patient samples processed with much less contamination from WBCs.

5.1 Design of the Microfluidic Device

The working principle of the 3D-printed microfluidic device is very similar to the device shown in Chapter 4, but there is an extra cell releasing step added to the operation process. When the whole blood sample is introduced into the device, it is first uniformly distributed, via 3D bifurcating channels, into multi-layered leukodepletion channels chemically functionalized for selectively capturing WBCs in flow. The leukodepleted blood sample is then routed onto a custom-built membrane filter. The immuno-functionalized membrane filter then chemically captures residual WBCs that escaped from the leukodepletion channels and only mechanically retains the CTCs. The rest of the blood components (i.e., RBCs, platelets, and serum) can pass through the filter pores and are ejected from the waste outlet. A reverse flow is then applied from the waste outlet to release the mechanically retained CTCs from the membrane filter and recollect them in a petri dish for downstream analysis (Figure 48).

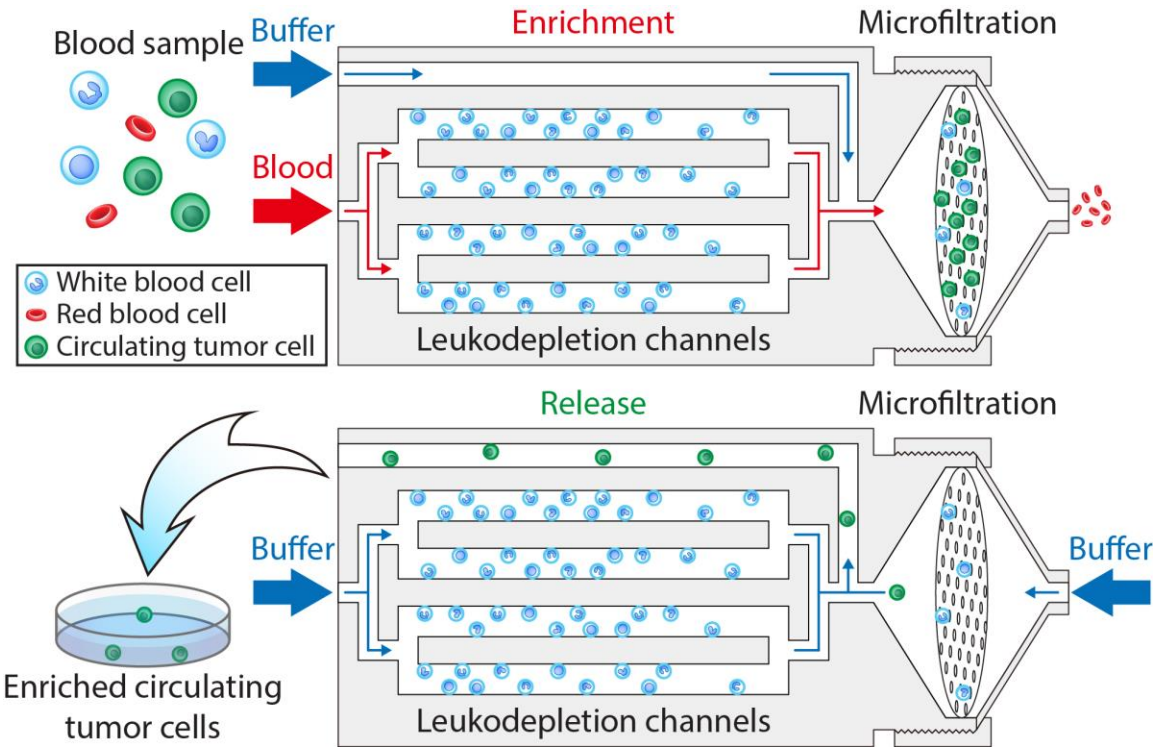

Figure 48: The design and operation principle of the 3D-printed microfluidic device.

Structurally, the designed device is similar to the device shown in Chapter 4 (Figure 49), but the filter compartment was modified to be compatible with the 20 mm-diameter, 3 µm-pore, membrane filter microfabricated out of polydimethylsiloxane (PDMS) (Figure 50). The filter itself could not be 3D-printed as with the rest of the device components due to insufficient resolution of the printer for achieving the desired pore size. In assembling the device, the separately fabricated membrane filter was sandwiched between two support layers with O-ring in place to prevent leakage. A threaded lock was used to secure the whole filter compartment assembly. This particular design of the microfiltration compartment allowed direct access for inserting and removing the thin PDMS membrane filter and held the membrane stable during capping and uncapping, which ensured against potential shear damage.

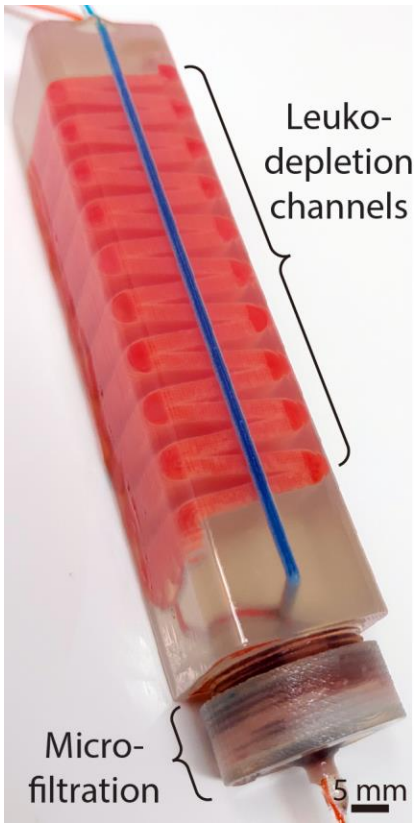

Figure 49: A photo of the 3D-printed microfluidic device.

Figure 50: A photo of the microfiltration stage and associated components.

5.2 Fabrication of the PDMS Filter Membrane

The 3D-printed microfluidic device was fabricated the same way as described in Chapter 4 and the membrane filter was fabricated through standard photolithography and spin-cast soft lithography.

To fabricate the PDMS membrane filter, first, we manufactured the mold with an array of micropillars. A 4-inch silicon wafer (UniversityWafer, Inc., Boston, MA) was first spin-coated with SU-8 2000 series photoresist (MicroChem, Westborough, MA) at 4000 rpm to create a 25 µm-thick photoresist film. The photoresist film was patterned with conventional photolithography to form a 30 mm × 30 mm 3 µm micropillar array with a 25% duty cycle, which was projected to produce a membrane filter with a pore density of 6,950 pores/mm^2 (Figure 51).

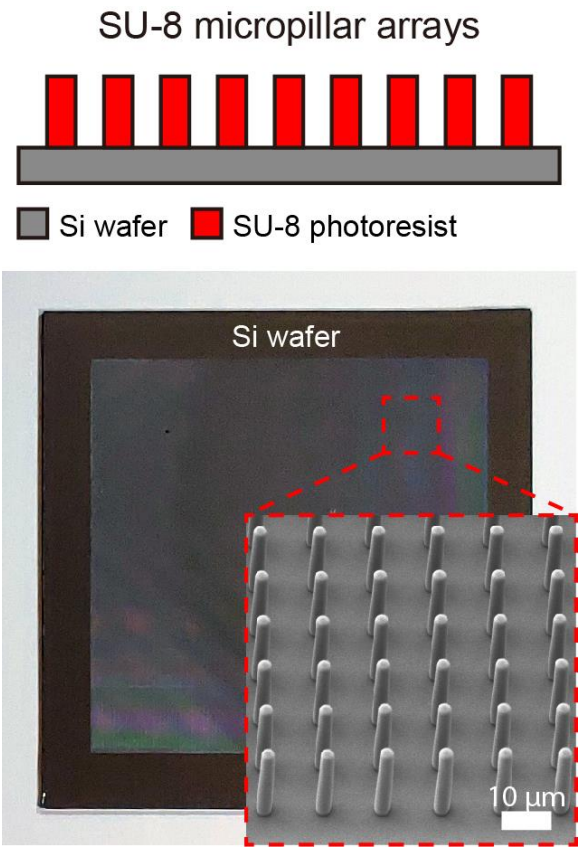

Figure 51: Fabrication illustration of the 3 μm SU-8 micropillar arrays on a silicon substrate.

After ensuring the mold is defect-free with a scanning electron microscope (SEM), a thin film of NR9-1500PY photoresist (Futurrex, Inc., Franklin, NJ) was spin-coated onto the mold as a sacrificial layer to facilitate demolding. In this process, to achieve a final thickness of <1 μm, the wafer was first spun at 600 rpm to evenly spread the photoresist and then at 4000 rpm. Next, a mixture (10:1) of PDMS elastomer Sylgard 184 and crosslinker (Dow Corning, Auburn, MI) was degassed in a desiccator and spin-coated on the sacrificial photoresist film at 3000 rpm, which produced a PDMS layer thick enough to fully cover all micropillars. We then uniformly etched the excess PDMS on micropillars to achieve through-holes by spinning 200 μL of hexane at 1000 rpm across the whole wafer

and cured on a hot plate at 120 °C for 10 minutes [223]. At this point, micropillars were observed to protrude from the PDMS film as intended (Figure 52).

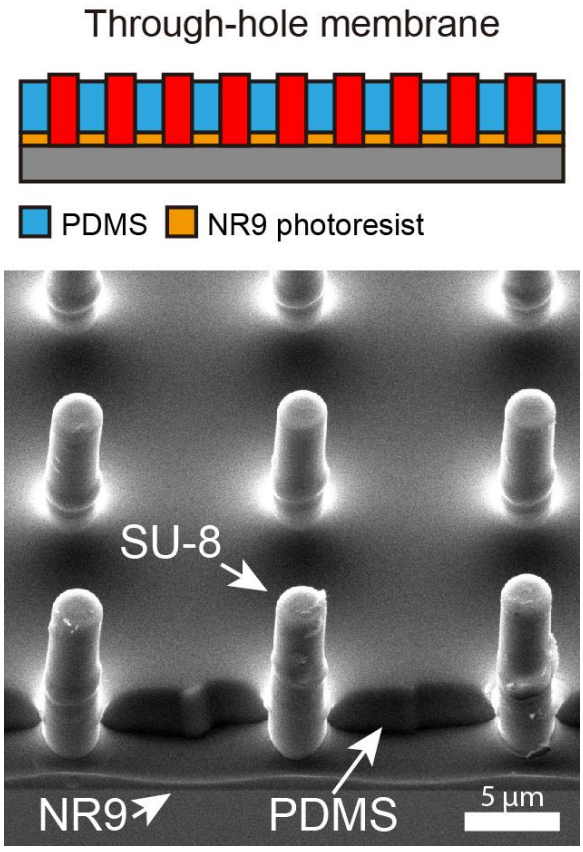

Figure 52: Fabrication illustration of the through-hole PDMS membrane on the SU-8 mold.

Next, the PDMS membrane filter was released from the mold by etching the sacrificial photoresist in acetone (Figure 53).

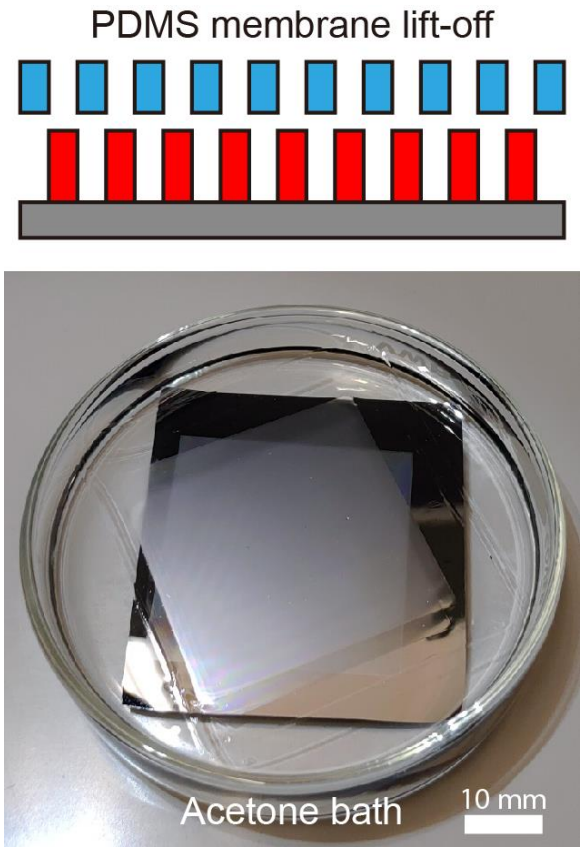

Figure 53: Fabrication illustration of the PDMS membrane filter demolded through the etching of the NR9 sacrificial photoresist.

The hydrophobicity of the PDMS membrane allowed it to float atop of the acetone after release [224], which we utilized to transfer the thin membrane filter onto the 3D-printed device (Figure 54). Scanning electron micrograph of the final PDMS membrane was observed to be free of defects and uniformly sized and spaced with through holes throughout the entire functional area.

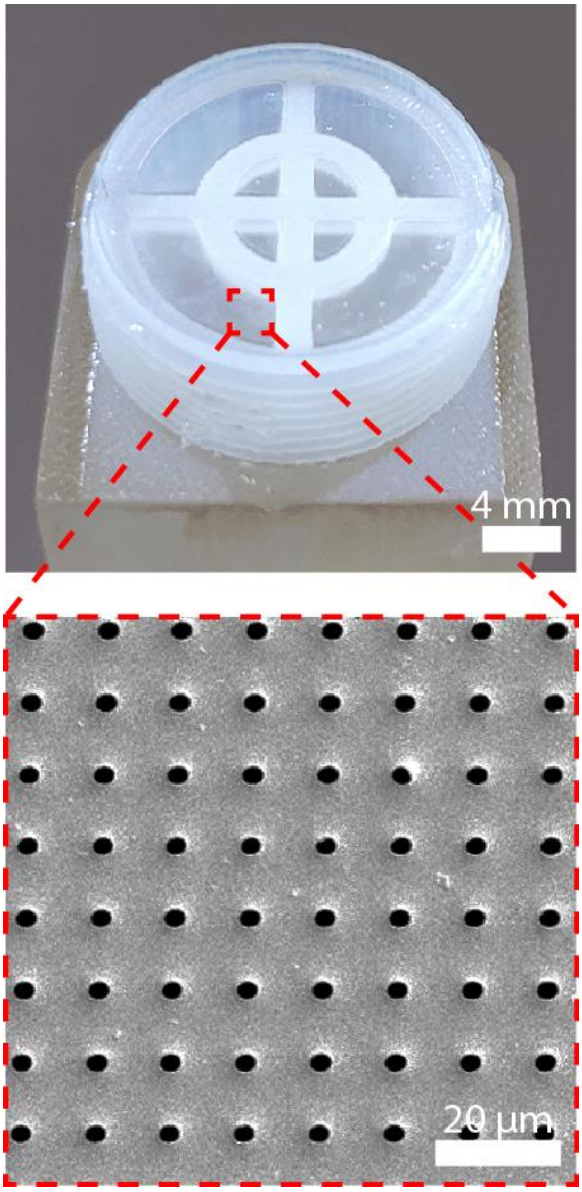

Figure 54: Photo of the PDMS membrane filter in the filtration compartment of the 3D-printed device.

5.3 Immuno-Functionalization of the Device

Prior to surface functionalization, the PDMS membrane filter was activated in oxygen plasma and then integrated into the 3D-printed microfluidic device. To functionalize the microfluidic channels and membrane filter for immunocapturing WBCs,

we first wetted the device with 200 proof ethanol (Thermo Fisher Scientific, Waltham, MA), and then applied the functionalization protocol described in Section 4.3. But after the incubation of NeutrAvidin, instead of pre-labeling the WBCs with biotinylated mouse anti-human CD45 antibodies, the biotinylated mouse anti-human CD45 antibodies were mixed in PBS and introduced to the device for 1 hour at room temperature to directly label the surfaces of the microchannels and membrane filter with anti-CD45 antibodies. Lastly, following a PBS wash, the device was then incubated with SuperBlock™ T20 (PBS) Blocking Buffer (Thermo Fisher Scientific, Waltham, MA) for 1 hour to block all non-specific binding sites, completing the functionalization process (Figure 55).

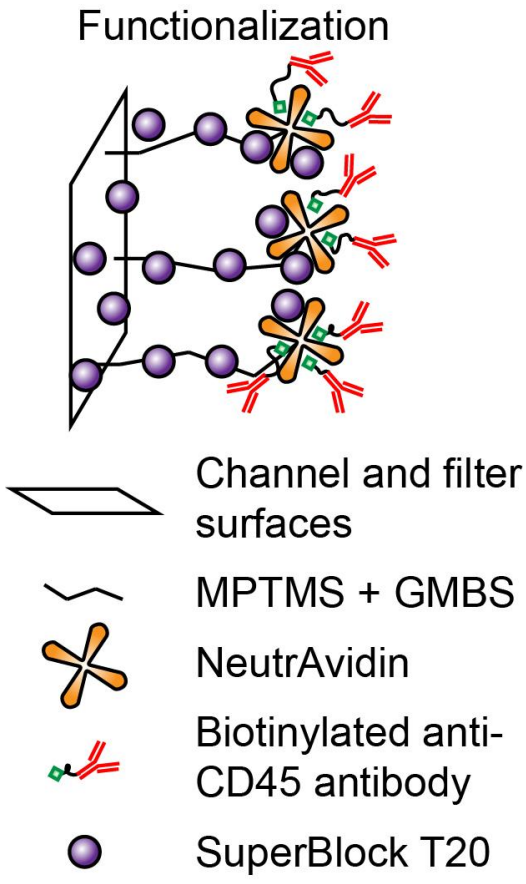

Figure 55: Functionalization of the 3D-printed microchannels and PDMS membrane filter surfaces.

5.4 Optimization of the Antibody Coverage on the Device Surface

To maximize the immunocapture efficiency, we next determined the optimal concentration of antibodies that would ensure complete surface coverage. In this process, antibody concentrations ranging from 0.5 μg/mL to 20 μg/mL were applied on an analytical version of the 3D-printed device and the PDMS membrane filter separately to account for potential disparity due to different materials. To measure antibody coverage in our tests, immobilized mouse anti-CD45 antibodies were labeled with a secondary antibody, Alexa Fluor 488 goat anti-mouse IgG (Invitrogen, Carlsbad, CA), at a manufacturer-suggested concentration of 1 μg/mL, and the resulting surface fluorescence intensity was measured with a fluorescence microscope (Figure 56). Measurements on the 3D-printed and PDMS surfaces were acquired under identical exposure settings for comparison, and all signals were normalized against the measured background fluorescence. While we observed ~40% more fluorescence on the PDMS surface at the limit, both surfaces were found to saturate at similar points with the surface fluorescence intensity rapidly increasing only with antibody concentrations of <10 μg/mL. Because the fluorescence signal remained virtually unchanged (<3% difference) for concentrations >10 μg/mL, we chose 10 μg/mL as the optimal concentration for antibody immobilization.

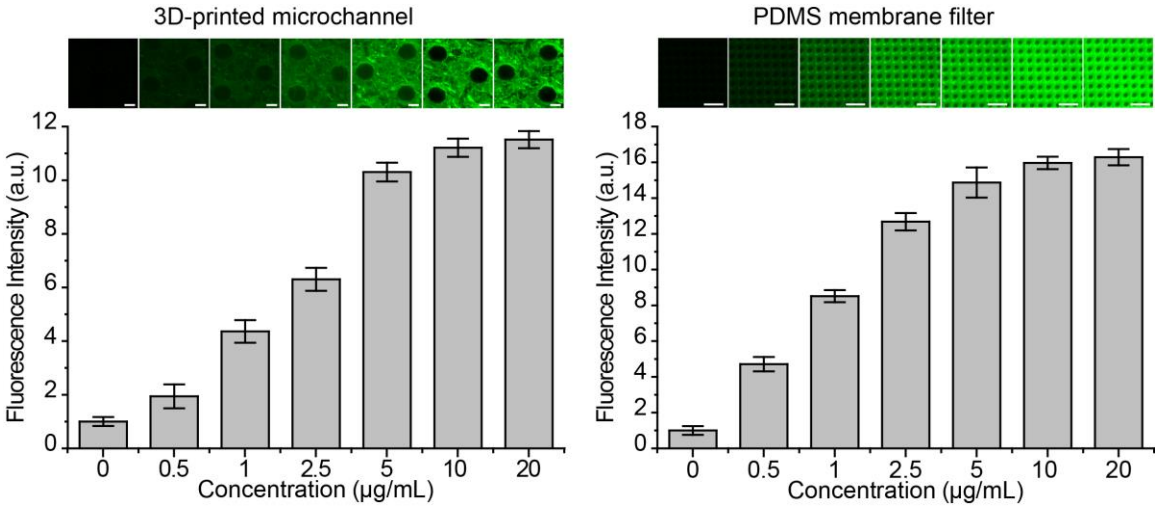

Figure 56: Measured normalized fluorescence signal intensity from anti-CD45 on (left) the 3D-printed microchannels and (right) the PDMS filter as a function of the antibody concentration used for incubation.

5.5 Processing Blood Samples on the Device

To test and optimize our microfluidic device, we processed fresh whole blood samples collected from consenting healthy volunteers. All research and experimental protocols were approved by the Institutional Review Board (IRB) at Georgia Institute of Technology and studies were performed in accordance with the relevant guidelines and ethical regulations of the IRB-approved protocol. Written informed consent was obtained from all volunteers for their participation in this study. Blood samples were withdrawn into tubes containing anti-coagulant ethylenediaminetetraacetic acid (EDTA) (BD, Franklin Lakes, NJ) and stored on a rocker at room temperature to prevent settling until they are processed within 4 hours of the collection. Complete blood count (CBC) was performed on all samples with a hematology analyzer (Abbott CELL-DYN Emerald) to measure the initial concentration of the WBCs. To measure WBC concentration in processed samples,

WBCs were first stained with Hoechst dye and imaged with a fluorescence microscope (Nikon Eclipse Ti-E), and counts acquired from multiple (>10) locations were averaged.

To investigate device performance for tumor cell enrichment, we processed simulated samples prepared by spiking a known amount of the tumor cells into whole blood samples collected from healthy donors. Human breast cancer cells MDA-MB-231 (ATCC® HTB-26™) were cultured in Dulbecco's Modified Eagle's medium (Corning Inc., Corning, NY) supplemented with 10% fetal bovine serum (FBS) (Seradigm, Radnor, PA) in an incubator at 37 °C and 5% CO_2. Once reached 80% confluency, cells were suspended via trypsinization and labeled with CellTracker™ Orange or Green dyes for identification with a fluorescence microscope. Fluorescently labeled tumor cells were then spiked in whole blood samples to achieve final concentrations of 1-5 × 10^3 tumor cells/mL. The viability of enriched tumor cells was measured with a live/dead cell assay (ab115347) (Abcam, Cambridge, UK) according to the manufacturer-suggested protocol.

5.6 Negative Depletion of White Blood Cells with the Functionalized Filter

To assess the contribution of a downstream anti-CD45-functionalized filter in depleting white blood cells, we separately tested the membrane filter outside of the device (Figure 57).

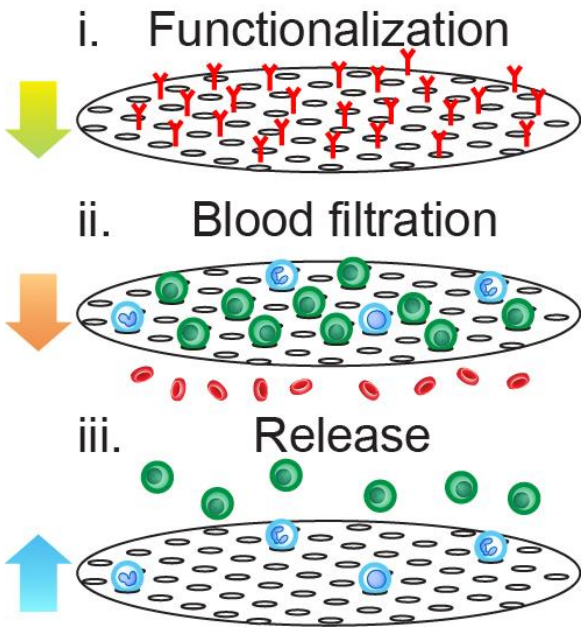

Figure 57: A schematic showing the tumor cell enrichment process.

Forward flow rates for both the sample and the buffer were set based on our earlier work in the last chapter that used a track-etched filter with 3 μm-diameter pores. To mimic the filter operating conditions when it is in the device (i.e., a buffer mixing with whole blood during the filtration stage), we simultaneously introduced 200 μL of whole blood spiked with MDA-MB-231 human breast tumor cells at 2 mL/hr and PBS washing buffer under 120 mbar pressure through a T-connector coupled to a commercial filter holder. We first characterized the efficiency of our microfabricated filter nucleated in capturing nucleated cells by counting fluorescently labeled tumor cells and nuclei-stained white blood cells both on the filter and in the filtrate with a fluorescence microscope. We found that our filter could retain virtually all (~99%) spiked tumor cells while capturing ~94% of the WBCs (Figure 58).

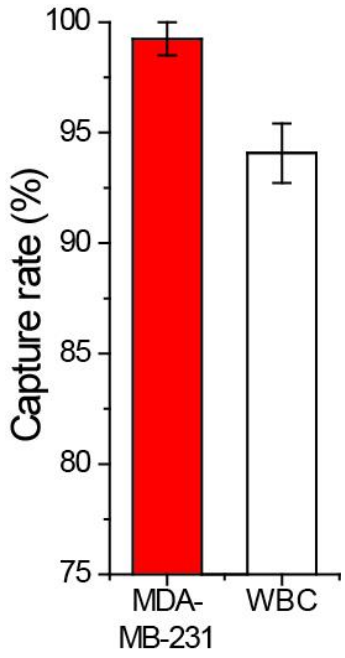

Figure 58: Measured capture rates of the MDA-MB-231 tumor cells and WBCs during filtration.

It should be noted that the measured WBC capture rate was higher than the previously reported capture rate of 82% on a non-functionalized 3 μm track-etched membrane filter. Enhanced capture efficiency was likely due to higher retention forces on WBCs due to their immunoaffinity towards the filter surface, an assessment supported by other studies on immuno-functionalized filtration [227].

Next, we analyzed the cell population released from our filter under varying reverse flow rates to determine the optimum conditions for maximizing enrichment. For each tested flow rate, cells were subjected to 5 mL of PBS in the reverse direction and the population collected in a petri dish was imaged with a fluorescence microscope to determine the fraction of cells that were successfully released. For all reverse flow rates tested, >95% of the spiked tumor cell population could be recovered with increasing flow rate from 1 to 10

mL/min having minimal (~2%) effect in enhancing the tumor cell release efficiency (Figure 59).

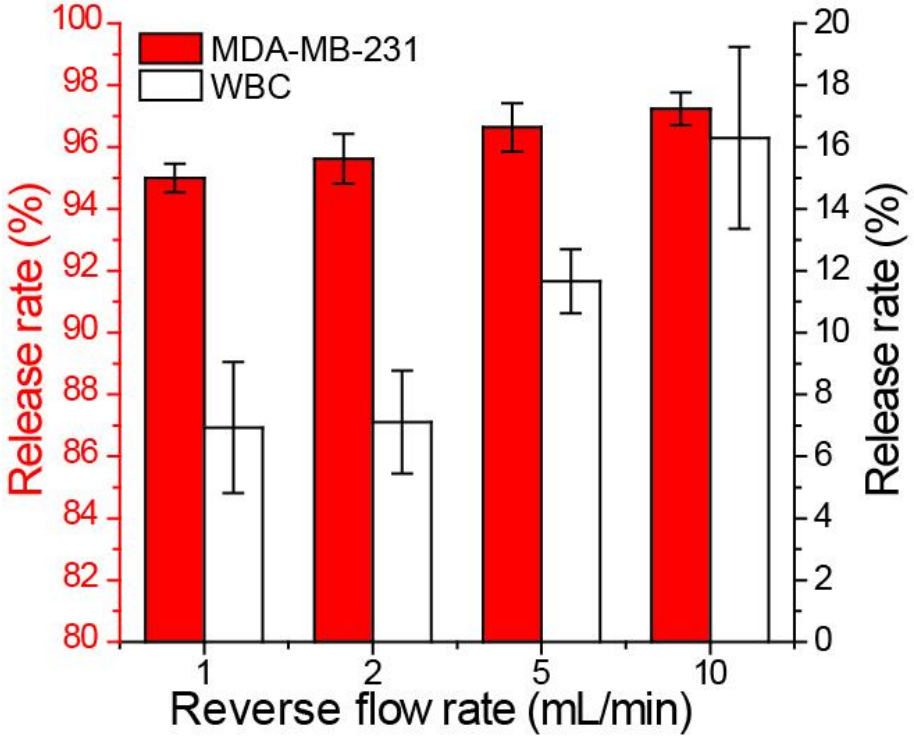

Figure 59: Measured release rates of the (left axis) MDA-MB-231 tumor cells and (right axis) WBCs under different reverse flow rates.

While more tumor cells could be released by increasing the reverse flow rate, those potential gains were negated with the increasing number of non-specifically- or loosely-bound WBCs detaching from the filter into the product. In fact, we found the number of WBCs in the released product more than doubled when the reverse flow rate increased from 1 mL/min to 10 mL/min. Also, a direct comparison between the microscope images of pre- and post-release states of the PDMS filter confirmed the release of WBCs along with tumor cells under reverse flow (Figure 60).

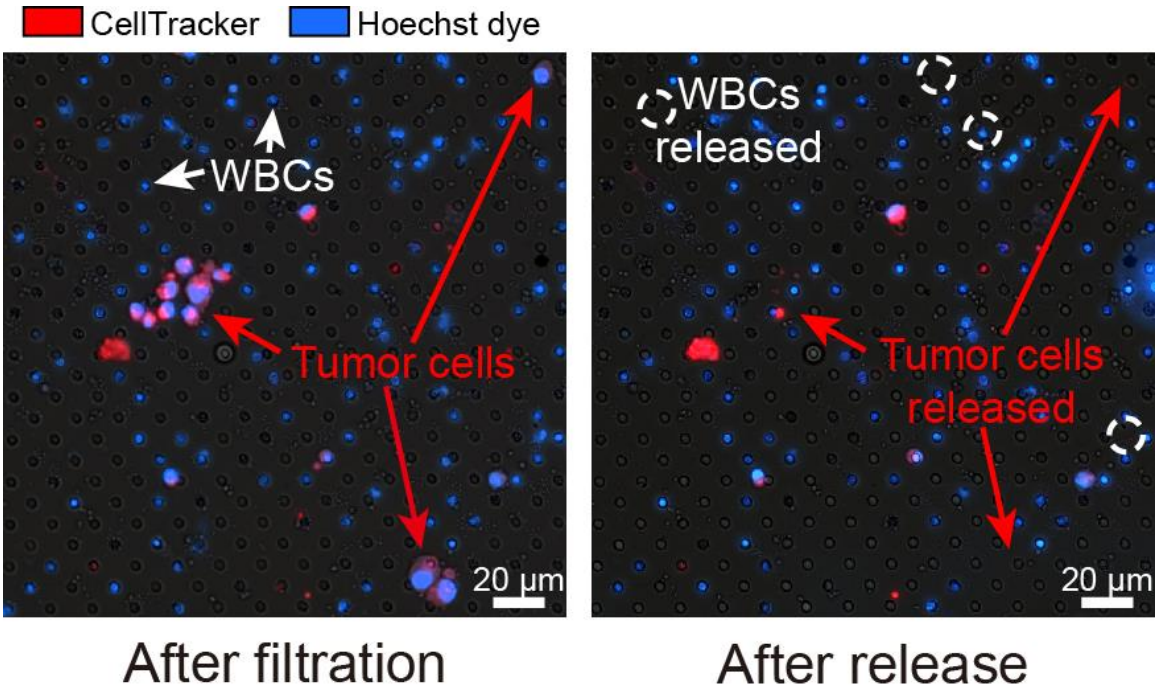

Figure 60: Fluorescence microscope images of the PDMS membrane filter (left) right after the filtration of the blood sample and (right) following the release of cells under reverse flow.

Therefore, to account for WBC contamination in the released product, we instead focused on the enrichment of tumor cells. For each reverse flow rate, we calculated an enrichment factor by dividing the tumor cell release rate by the WBC release rate (Figure 61). At lower reverse flow rates (1-2 mL/min), we found the functionalized filter provided more than an order of magnitude increase in CTC enrichment. The maximum enrichment factor of ~13.7X was achieved at a reverse flow rate of 1 mL/min, which we chose as the optimal flow rate for releasing from our device in subsequent studies in this work.

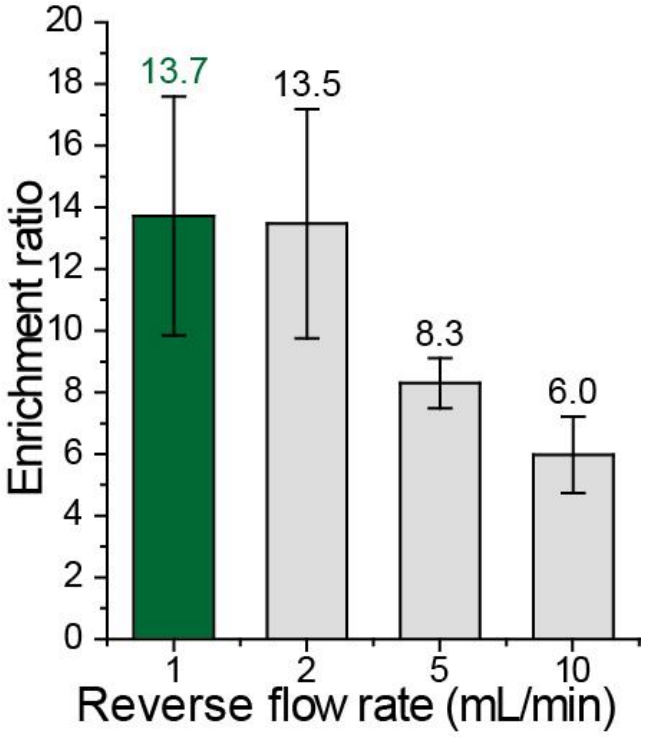

Figure 61: Calculated average enrichment ratio for the spiked tumor cells as a function of different reverse flow rates.

5.7 Characterization of the Full Device with Simulated Blood Samples

To characterize the complete device, we placed the microfabricated PDMS filter into the filter compartment of our microfluidic device, chemically functionalized the device and then processed blood samples collected from healthy volunteers (Figure 62).

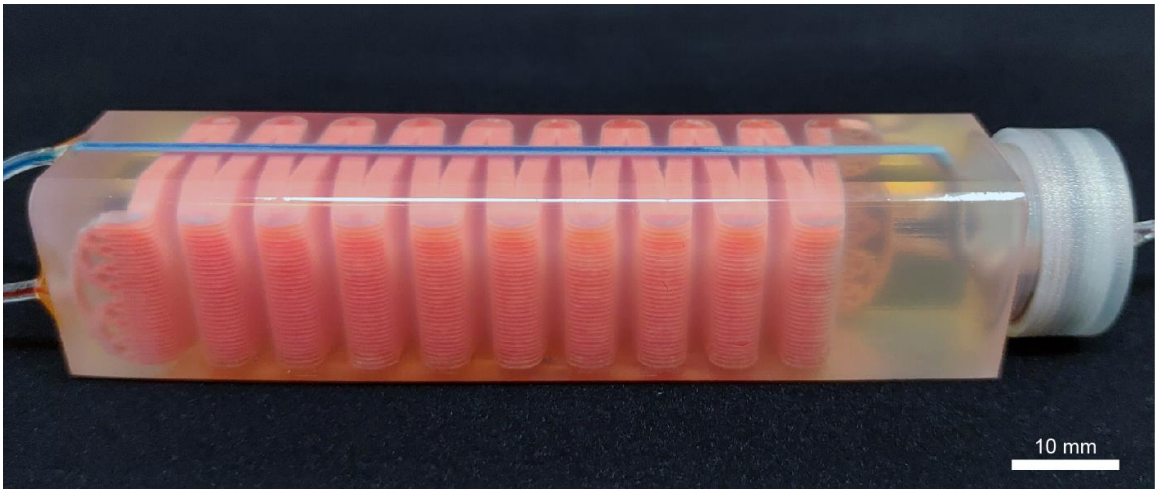

Figure 62: Characterization of the full device with simulated blood samples.

We first studied the immunocapture of WBCs within the device. In these experiments, 10 mL whole blood was driven through the device at an optimized flow rate of 2 mL/hr, which resulted in an average cell flow speed of ~100 μm/s throughout microfluidic channels and led to an efficient immunocapture of WBCs. Likewise, the PBS washing buffer was pneumatically delivered at an optimized rate to the filtration compartment at 120 mbar. By comparing the concentration of WBCs in the sample versus the waste, we found that our device was able to capture on average ~99.6 of WBCs directly from whole blood with no labels (Figure 63).

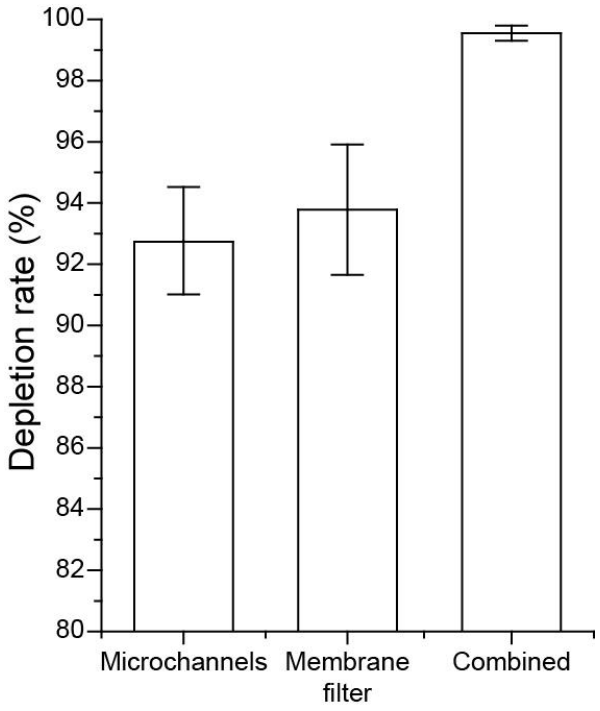

Figure 63: Measured WBC immunocapture rates in the leukodepletion channels, on the membrane filter, and the combined immunocapture rate for the whole device.

To determine the individual contributions of immunodepletion channels and the filter on this capture rate, we removed the filter from the device at the end of the process, immunostained the nuclei of cells and directly counted filter-captured WBCs with a fluorescence microscope. Based on this information, we also calculated the number of WBCs captured at immunodepletion channels by subtracting the number of cells on the filter and in the waste from the number of WBC in the original sample. We found that we could capture on average ~92.8% of WBCs at immunodepletion channels while the anti-CD45 functionalized filter captured on average an additional ~6.8% (out of the ~7.2% that evaded capture at immunodepletion channels) corresponding to a ~93.8% capture efficiency (Figure 63).

Next, we tested our device in its ability to enrich tumor cells spiked in whole blood samples collected from healthy donors. The simulated blood samples were processed with our device, and the enriched product was released into a petri dish for analysis. We could positively identify cells in the released product for measurements since we (1) pre-labeled tumor cells with CellTracker™ Green before spiking, (2) immunostained WBCs against CD45 using Alexa Fluor® 594 anti-human CD45 (Biolegend, San Diego, CA) on the filter prior to release. In addition, nuclei of both tumor cells and WBCs were labeled with Hoechst 33342 dye to prevent false positives (Figure 64).

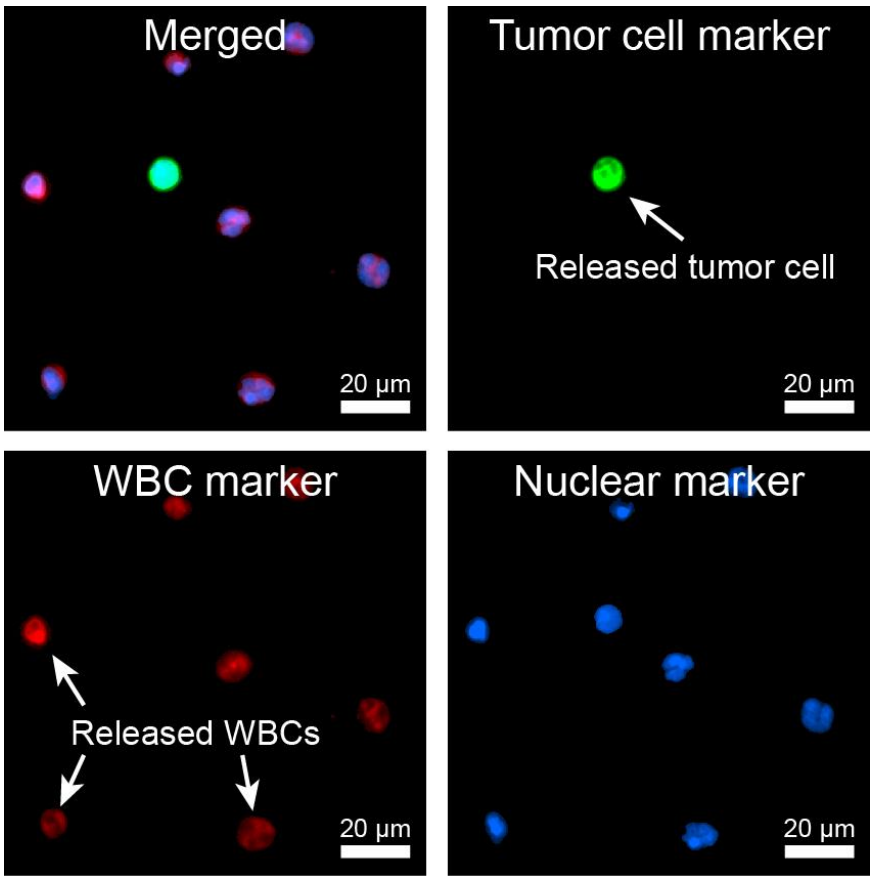

Figure 64: Fluorescence microscope images of the released cells in suspension.

By comparing the number of tumor cells in the released product with the initial number of spiked tumor cells in the sample, we found that we could recover on average ~91.4% of tumor cells (Figure 65).

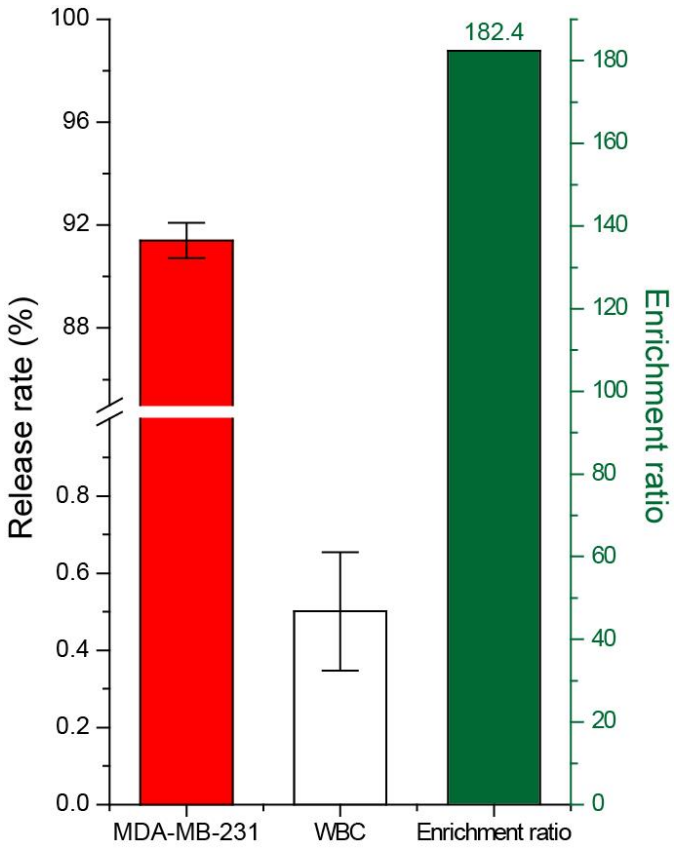

Figure 65: Measured (left axis) release rates for the spiked tumor cells and WBCs, and (right axis) the enrichment ratio calculated based on these release rates.

Part of the cell loss was contributed by the non-specific binding of tumor cells to the leukodepletion channels (Figure 66).

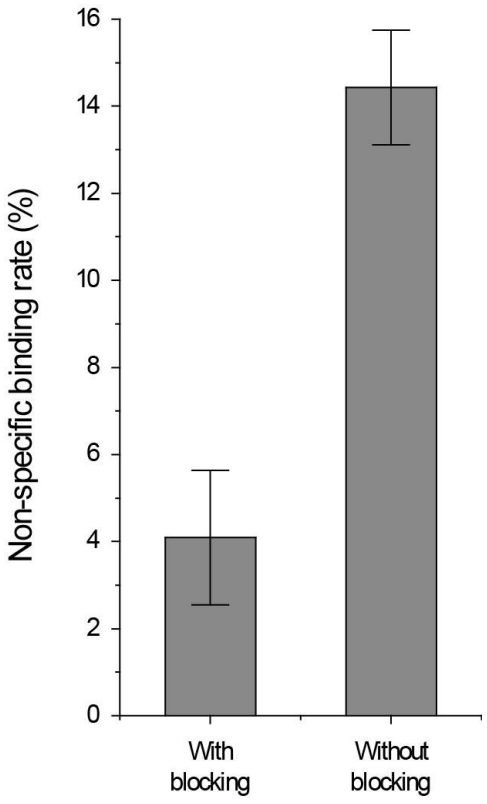

Figure 66: Non-specific binding of the MDA-MB-231 tumor cells in the microchannels.

In agreement with experiments with non-spiked samples, we could find <0.5% of WBCs in the released product. Taken together, these figures demonstrated that our device could enrich the tumor cells on average by ~182.4X against the contaminating WBCs in addition to removing virtually all of RBCs and platelets. Furthermore, we tested the viability of the enriched tumor cells in the released product and found that enriched cells remained intact with no noticeable change in viability (Figure 67).

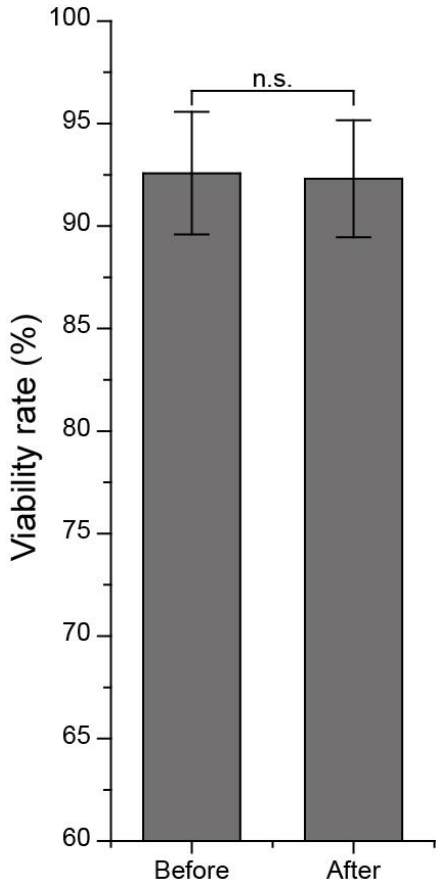

Figure 67: Measured tumor cell viability rates before and after processing through microfluidic device.

Given the label-free enrichment process and the fact that viable tumor cells are readily available in suspension suggests the possibility of directly coupling our device with standard molecular and functional assays downstream.

5.8 Isolation of Circulating Tumor Cells from Clinical Samples

We finally used our devices to isolate CTCs from peripheral blood samples collected from patients with metastatic disease. We analyzed both prostate and pancreatic cancer samples to demonstrate the applicability of our assay with different cancer types. Blood samples for this study were collected from consenting patients at Emory University

Hospital or Grady Memorial Hospital following Institutional Review Board (IRB)-approved protocols and then transported to Georgia Tech to be processed within 4 hours of withdrawal. For each case, 10 mL of unmanipulated blood samples were processed with our device under the conditions established earlier in this paper, and the product was immunostained against tumor-specific antigens to positively identify CTCs among contaminating blood cells. Immunostaining and washing steps were performed external to the device by directly releasing the enriched population from the device onto a commercial track-etched membrane filter (Whatman plc, Maidstone, United Kingdom) with 1 μm-diameter pores to ensure complete retention. Following the fixation and permeabilization of the released cells, samples were immunostained against established prostate or pancreatic cancer markers along with WBC markers and a nuclear stain to positively identify enriched CTCs.

5.8.1 Immunofluorescence Staining of Patient CTCs

Blood samples from prostate and pancreatic cancer patients were obtained under the IRB-approved protocols at Grady Memorial Hospital and Emory University Hospital, respectively, according to the relevant guidelines and regulations. Informed consent was obtained from all patients according to the IRB-approved protocols. To immunostain the CTCs enriched from cancer patient blood samples, cells released from our device were first fixed in 4% paraformaldehyde (PFA) (Electron Microscopy Sciences, Hatfield, PA) and permeabilized with 1% Nonidet-P40 (Thermo Fisher Scientific, Waltham, MA). Prostate cancer CTCs were labeled with primary antibodies against Cytokeratin 8/18 (Invitrogen, Carlsbad, CA), vimentin (Invitrogen, Carlsbad, CA), and prostate-specific antigen Kallikrein 3 (PSA/KLK3) (Cell Signaling, Danvers, MA) [228]-[230]. Pancreatic cancer

CTCs were immunostained against Cytokeratin 7/8/18 (Invitrogen, Carlsbad, CA), EpCAM (Invitrogen, Carlsbad, CA), and vimentin [231]-[233]. For both cancer types, a matching secondary antibody with Alexa Fluor 488 (Invitrogen, Carlsbad, CA) was then applied to generate the fluorescence signal from immunolabeled CTCs. Contaminating WBCs were labeled with Anti-CD45 (BD Biosciences, San Jose, CA) primary antibody followed by Alexa Fluor 594 (Invitrogen, Carlsbad, CA). Finally, 4′,6-diamidino-2-phenylindole (DAPI) (Invitrogen, Carlsbad, CA) was used to stain the nuclei of all nucleated cells.

We scored immunostained cells as CTCs only if they were positive for tumor and nuclear markers and also negative for WBC markers (Figure 68).

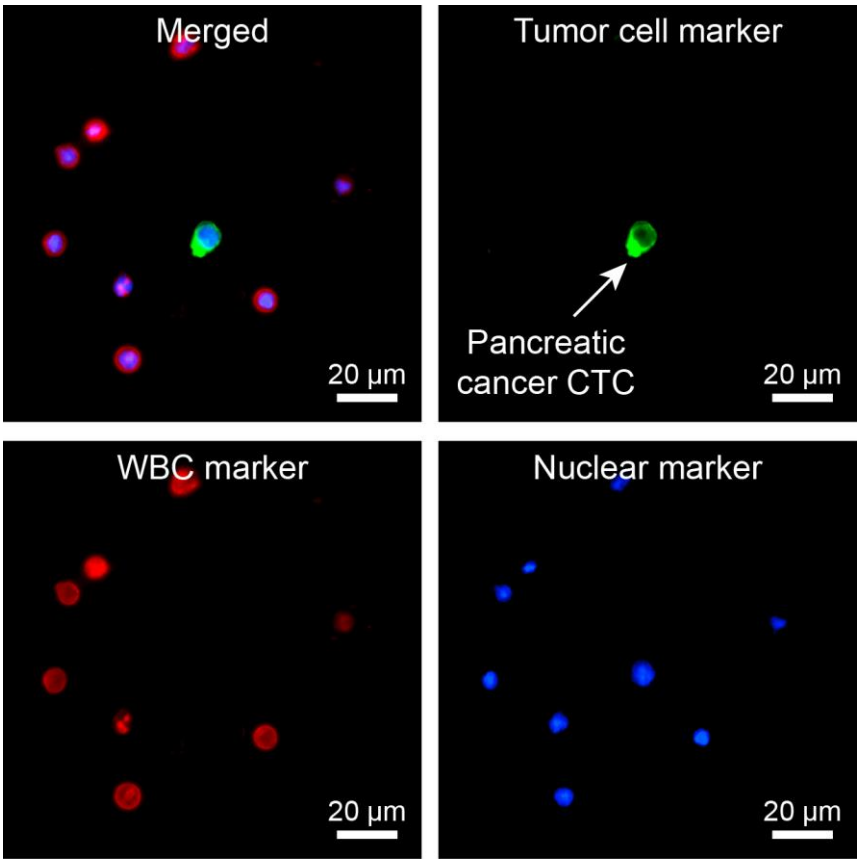

Figure 68: Fluorescence microscope images of the enriched CTC from a pancreatic cancer patient's blood sample.

In the clinical samples processed, we found 8 and 12 CTCs from the prostate samples and 3 CTCs from the pancreatic sample (Table 1).

Table 1: Number of CTCs enriched from prostate and pancreatic patients' samples.

Patient Type	Patient ID	Number of CTCs	CTC Density (CTCs/mL)
Prostate	Pro_001	8	0.8
	Pro_002	12	1.2
Pancreatic	Pan_001	3	0.3

In one of the prostate cancer patient samples, we also found a two-cell cluster (Figure 69), demonstrating the potential of our device for isolation of CTC-clusters, which has been shown to have greater metastatic propensity than single CTCs [234], [235].

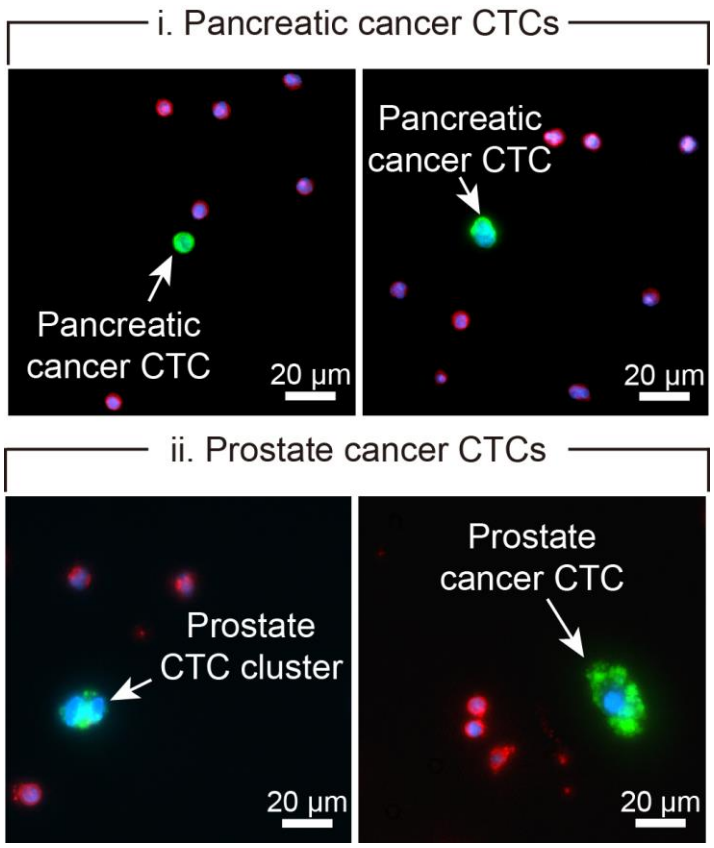

Figure 69: Representative immunofluorescence images of patient CTCs isolated from pancreatic and prostate cancer patients' blood samples.

In fact, relatively large features in our immunodepletion channels leave ample space for cell clusters to proceed without facing obstacles and can be seen as an advantage to protect the integrity of CTC clusters. Taken together, these preliminary results demonstrate the clinical potential of our technology for isolating CTCs from blood samples as-withdrawn from patients with no sample preparation.

5.9 Summary

The ability to reliably harvest tumor cells from peripheral blood of cancer patients in a practical manner will not only transform how cancers are diagnosed and managed but also impact the basic research on metastasis and drug development. In my Ph. D. thesis, I

reported a blood test that relies on a combination of chemical and physical markers to specifically identify CTCs with no sample manipulation whatsoever. The fact that the enrichment process does not rely on tumor-specific markers makes our assay applicable virtually on cancers with solid tumors.

CHAPTER 6. CONCLUSION AND FUTURE WORK

Isolation and analysis of circulating tumor cells (CTCs) from blood samples present exciting opportunities for basic cancer research and personalized treatment of the disease. While microchip-based negative CTC enrichment offers both sensitive microfluidic cell screening and unbiased selection, conventional microchips are inherently limited by their capacity to deplete a large number of normal blood cells. In my Ph. D. research, I have used 3D printing and developed a monolithic device that combines immunoaffinity-based microfluidic cell capture and a membrane filter for negative enrichment of CTCs directly from whole blood.

In order to fabricate the complex 3D-printed microfluidic device for the negative enrichment of CTCs, I developed a centrifugal sacrificial material removal method that exploits the differences in densities between the sacrificial material and the liquid ambient to discharge sacrificial material. Unlike conventional methods that rely on injection-driven discharge of the sacrificial, uniform volume forces created via centrifugation remove sacrificial material from fully enclosed microchannels irrespective of the channel fluidic resistance. This was the key piece that allowed me to fabricate complex 3D microfluidic devices with no clogging or residual sacrificial materials inside the printed channels and utilized the full functionality of the printed devices.

Utilizing the technique that I have developed for fabricating complex 3D-printed microfluidic devices, I developed an immunoaffinity-based negative enrichment 3D-printed microfluidic device to achieve label-free enrichment of CTCs directly from clinically relevant volume of unmanipulated blood samples from both prostate and

pancreatic cancer patients. The developed 3D microfluidic device was designed with multi-layers of leukodepletion channels that provided sufficient active surface area to deplete a large number of WBCs presented in clinically relevant volumes of whole blood, which was not possible by the conventional microfluidic device. To eliminate the need for a sample preparation step for lysing RBCs, the device was integrated with a membrane micropore filter downstream of the leukodepletion channels. The membrane filter was used to retain all nucleated cells (tumor cells and potential WBCs that eluded immunocapture) in the immunodepleted sample and dispose of RBCs and platelets. To further enhanced the capture efficiency of the WBCs, the membrane filter was immuno-functionalized to chemically capture residual WBCs that escaped from the leukodepletion channels. The enriched intact and label-free CTCs can then be released from the device into liquid suspension, which is suitable for any functional assays downstream, such as drug testing and molecular analysis. With the developed device, I have demonstrated its clinical feasibility by isolating pancreatic and prostate cancer CTCs directly from 10 mL unmanipulated patients' blood samples.

With the demonstrated feasibility in processing clinical samples, I envision that with the finer microscale features that will be enabled by ongoing advances in additive manufacturing as well as the centrifugal sacrificial material removal method that I developed, the performance of developed label-free negative enrichment 3D microfluidic device will be further improved and ultimately allows it to be used in clinical settings for the screening of CTCs from patients with different kinds of metastatic cancer. Furthermore, considering the additive manufacturing becoming widely accessible for personal use and in commercial buildings such as schools and offices, the developed 3D printed device that

utilizes a commercially available 3D-printer to create the bulk of the fully-functional CTC assay suggests the intriguing possibility of on-demand, decentralized manufacturing of these tests at homes and offices.

6.1 Future Work

To further increase the depletion rate of the WBCs from a blood sample, we can implement the use of an antibody cocktail for the capturing of WBCs. Currently, only anti-CD45 antibody is used in the device. By including the use of other WBC-specific antibodies, such as anti-CD66b or anti-CD38 antibodies, I envision that the capture rate of the WBCs can be further increased. Also, with the increased resolution in 3D printing, thinner channels and more compact micropillar arrays can further improve the capture efficiency of the WBCs by the functionalized surfaces, which can lead to an increase in the overall throughput of the device. This will greatly decrease the processing time required for the blood sample and ultimately allow the device to be used in the clinical setting. Moreover, the number of parallel immunocapture channels can also be increased by implementing a custom-built container in the centrifuge to remove the support materials from devices that are larger than the 50 mL centrifugation tubes. Lastly, to prolong the functional time of the functionalized devices for the capturing of WBCs and negative enrichment of CTCs, aptamers that are specific to the WBCs can be used instead of antibodies since they are known to be more stable than the biological antibody while having a longer shelf life.

REFERENCES

[1] Esmaeilsabzali, H., Beischlag, T.V., Cox, M.E., Parameswaran, A.M. and Park, E.J. "Detection and isolation of circulating tumor cells: principles and methods," Biotechnol. Adv., vol. 31, pp.1063-1084, 2013.

[2] American Cancer Society. Cancer Statistics Center. http://cancerstatisticscenter.cancer.org. Accessed July 06, 2021.

[3] Dillekås, H., Rogers, M.S. and Straume, O. "Are 90% of deaths from cancer caused by metastases?," Cancer Med., vol. 8, pp.5574-5576, 2019.

[4] Yadav, A.R. and Mohite, S.K. "Cancer-A silent killer: An overview," Asian J. Pharm. Res., vol. 10, pp.213-216, 2020.

[5] Gupta, G.P. and Massagué, J. "Cancer metastasis: building a framework," Cell, vol. 127, pp.679-695, 2006.

[6] Ashworth, T.R. "A case of cancer in which cells similar to those in the tumours were seen in the blood after death," Aust. Med. J., vol. 14, p.146, 1869.

[7] Paget, S. "The distribution of secondary growths in cancer of the breast," The Lancet, vol. 133, pp.571-573, 1889.

[8] Fidler, I.J. "The pathogenesis of cancer metastasis: the 'seed and soil' hypothesis revisited," Nat. Rev. Cancer, vol. 3, p.453, 2003.

[9] Wittekind, C. and Neid, M. "Cancer invasion and metastasis," Oncology, vol. 69, pp.14-16, 2005.

[10] Paterlini-Brechot, P. and Benali, N.L. "Circulating tumor cells (CTC) detection: clinical impact and future directions," Cancer Lett., vol. 253, pp.180-204, 2007.

[11] van de Stolpe, A., Pantel, K., Sleijfer, S., Terstappen, L.W. and Den Toonder, J.M. "Circulating tumor cell isolation and diagnostics: toward routine clinical use," Cancer Res., vol. 71, 2011.

[12] Budd, G.T., Cristofanilli, M., Ellis, M.J., Stopeck, A., Borden, E., Miller, M.C., Matera, J., Repollet, M., Doyle, G.V., Terstappen, L.W. and Hayes, D.F. "Circulating tumor cells versus imaging—predicting overall survival in metastatic breast cancer," Clin. Cancer Res., vol. 12, pp.6403-6409, 2006.

[13] Al-Mehdi, A.B., Tozawa, K., Fisher, A.B., Shientag, L., Lee, A. and Muschel, R.J. "Intravascular origin of metastasis from the proliferation of endothelium-attached tumor cells: a new model for metastasis," Nat. Med., vol. 6, p.100, 2000.

[14] Lurje, G., Schiesser, M., Claudius Hoffmann, A. and Schneider, P.M. "Circulating tumor cells in gastrointestinal malignancies: current techniques and clinical implications," J. Oncol., vol. 2010, 2010.

[15] Arya, S.K., Lim, B. and Rahman, A.R.A. "Enrichment, detection and clinical significance of circulating tumor cells," Lab Chip, vol. 13, pp.1995-2027, 2013.

[16] Onstenk, W., Gratama, J.W., Foekens, J.A. and Sleijfer, S. "Towards a personalized breast cancer treatment approach guided by circulating tumor cell (CTC) characteristics," Cancer Treat. Rev., vol. 39, pp.691-700, 2013.

[17] Zhang, Y., Lv, Y., Niu, Y., Su, H. and Feng, A. "Role of circulating tumor cell (CTC) monitoring in evaluating prognosis of triple-negative breast cancer patients in China," Med. Sci. Monit., vol. 23, p.3071, 2017.

[18] Toss, A., Mu, Z., Fernandez, S. and Cristofanilli, M. "CTC enumeration and characterization: moving toward personalized medicine," Ann. Transl. Med., vol. 2, 2014.

[19] Allard, W.J., Matera, J., Miller, M.C., Repollet, M., Connelly, M.C., Rao, C., Tibbe, A.G., Uhr, J.W. and Terstappen, L.W. "Tumor cells circulate in the peripheral blood of all major carcinomas but not in healthy subjects or patients with nonmalignant diseases," Clin. Cancer Res., vol. 10, pp.6897-6904, 2004.

[20] Paterlini-Brechot, P. and Benali, N.L. "Circulating tumor cells (CTC) detection: clinical impact and future directions," Cancer Lett., vol. 253, pp.180-204, 2007.

[21] Yap, T.A., Lorente, D., Omlin, A., Olmos, D. and De Bono, J.S. "Circulating tumor cells: a multifunctional biomarker," Clin. Cancer Res., vol. 20, pp.2553-2568, 2014.

[22] Vona, G., Sabile, A., Louha, M., Sitruk, V., Romana, S., Schütze, K., Capron, F., Franco, D., Pazzagli, M., Vekemans, M. and Lacour, B. “Isolation by size of epithelial tumor cells: a new method for the immunomorphological and molecular characterization of circulating tumor cells,” Am. J. Pathol., vol. 156, pp.57–63, 2000.

[23] Zheng, S., Lin, H., Liu, J.Q., Balic, M., Datar, R., Cote, R.J. and Tai, Y.C. “Membrane microfilter device for selective capture, electrolysis and genomic analysis of human circulating tumor cells,” J. Chromatogr. A, vol. 1162, pp.154-161, 2007.

[24] Rosenberg, R., Gertler, R., Friederichs, J., Fuehrer, K., Dahm, M., Phelps, R., Thorban, S., Nekarda, H. and Siewert, J.R. “Comparison of two density gradient centrifugation systems for the enrichment of disseminated tumor cells in blood,” Cytometry, vol. 49, pp.150-158, 2002.

[25] Krivacic, R.T., Ladanyi, A., Curry, D.N., Hsieh, H.B., Kuhn, P., Bergsrud, D.E., Kepros, J.F., Barbera, T., Ho, M.Y., Chen, L.B. and Lerner, R.A. “A rare-cell detector for cancer,” Proc. Natl. Acad. Sci. U. S. A., vol. 101, pp.10501-10504, 2004.

[26] Talasaz, A.H., Powell, A.A., Huber, D.E., Berbee, J.G., Roh, K.H., Yu, W., Xiao, W., Davis, M.M., Pease, R.F., Mindrinos, M.N. and Jeffrey, S.S. “Isolating highly enriched populations of circulating epithelial cells and other rare cells from blood using a magnetic sweeper device,” Proc. Natl. Acad. Sci. U. S. A., vol. 106, pp.3970-3975, 2009.

[27] Miller, M.C., Doyle, G.V. and Terstappen, L.W. “Significance of circulating tumor cells detected by the CellSearch system in patients with metastatic breast colorectal and prostate cancer,” J. Oncol., vol. 2010, 2010.

[28] Lara, O., Tong, X., Zborowski, M. and Chalmers, J.J. “Enrichment of rare cancer cells through depletion of normal cells using density and flow-through, immunomagnetic cell separation,” Exp. Hematol., vol. 32, pp.891-904, 2004.

[29] Wheeler, A.R., Throndset, W.R., Whelan, R.J., Leach, A.M., Zare, R.N., Liao, Y.H., Farrell, K., Manger, I.D. and Daridon, A. “Microfluidic device for single-cell analysis,” Anal. Chem., vol. 75, pp.3581-3586, 2003.

[30] McDonald, J.C., Duffy, D.C., Anderson, J.R., Chiu, D.T., Wu, H., Schueller, O.J. and Whitesides, G.M. “Fabrication of microfluidic systems in poly (dimethylsiloxane),” Electrophoresis, vol. 21, pp.27-40, 2000.

[31] Whitesides, G.M. “The origins and the future of microfluidics,” Nature, vol. 442, p.368, 2006.

[32] Liu, Z., Huang, F., Du, J., Shu, W., Feng, H., Xu, X. and Chen, Y. “Rapid isolation of cancer cells using microfluidic deterministic lateral displacement structure,” Biomicrofluidics, vol. 7, p.011801, 2013.

[33] Lee, M.G., Shin, J.H., Bae, C.Y., Choi, S. and Park, J.K. “Label-free cancer cell separation from human whole blood using inertial microfluidics at low shear stress,” Anal. Chem., vol. 85, pp.6213-6218, 2013.

[34] Sarioglu, A.F., Aceto, N., Kojic, N., Donaldson, M.C., Zeinali, M., Hamza, B., Engstrom, A., Zhu, H., Sundaresan, T.K., Miyamoto, D.T., Luo, X. Bardia, A., Wittner, B.S., Ramaswamy, S., Shioda, T., Ting, D.T., Stott, S.L., Kapur, R., Maheswaran, S., Haber, D.A. and Toner, M. “A microfluidic device for label-free, physical capture of circulating tumor cell clusters,” Nat. Methods, vol. 12, p.685, 2015.

[35] Ozkumur, E., Shah, A.M., Ciciliano, J.C., Emmink, B.L., Miyamoto, D.T., Brachtel, E., Yu, M., Chen, P.I., Morgan, B., Trautwein, J. and Kimura, A. “Inertial focusing for tumor antigen–dependent and–independent sorting of rare circulating tumor cells,” Sci. Transl. Med., vol. 5, pp.179ra47-179ra47, 2013.

[36] Karabacak, N.M., Spuhler, P.S., Fachin, F., Lim, E.J., Pai, V., Ozkumur, E., Martel, J.M., Kojic, N., Smith, K., Chen, P.I. and Yang, J. “Microfluidic, marker-free isolation of circulating tumor cells from blood samples,” Nat. Protoc., vol. 9, p.694, 2014.

[37] Ho, C.M.B., Ng, S.H., Li, K.H.H. and Yoon, Y.J. “3D printed microfluidics for biological applications,” Lab Chip, vol. 15, pp.3627-3637, 2015.

[38] Bhushan, B. and Caspers, M. “An overview of additive manufacturing (3D printing) for microfabrication,” Microsyst. Technol., vol. 23, pp.1117-1124, 2017.

[39] Comina, G., Suska, A. and Filippini, D. “PDMS lab-on-a-chip fabrication using 3D printed templates,” Lab Chip, vol. 14, pp.424-430, 2014.

[40] Sun, M., Xie, Y., Zhu, J., Li, J. and Eijkel, J.C. “Improving the resolution of 3D-Printed molds for microfluidics by iterative casting-shrinkage cycles,” Anal. Chem., vol. 89, pp.2227-2231, 2017.

[41] Amin, R., Knowlton, S., Hart, A., Yenilmez, B., Ghaderinezhad, F., Katebifar, S., Messina, M., Khademhosseini, A. and Tasoglu, S. “3D-printed microfluidic devices,” Biofabrication, vol. 8, p.022001, 2016.

[42] Au, A.K., Huynh, W., Horowitz, L.F. and Folch, A. “3D-printed microfluidics,” Angew. Chem. Int., vol. 55, pp.3862-3881, 2016.

[43] Chen, J., Liu, C.Y., Wang, X., Sweet, E., Liu, N., Gong, X. and Lin, L. “3D printed microfluidic devices for circulating tumor cells (CTCs) isolation,” Biosens. Bioelectron., vol. 150, p.111900, 2020.

[44] Chen, C., Mehl, B.T., Munshi, A.S., Townsend, A.D., Spence, D.M. and Martin, R.S. “3D-printed microfluidic devices: fabrication, advantages and limitations—a mini review,” Anal. Methods, vol. 8, pp.6005-6012, 2016.

[45] Stott, S.L., Hsu, C.H., Tsukrov, D.I., Yu, M., Miyamoto, D.T., Waltman, B.A., Rothenberg, S.M., Shah, A.M., Smas, M.E., Korir, G.K. and Floyd, F.P. “Isolation of circulating tumor cells using a microvortex-generating herringbone-chip,” Proc. Natl. Acad. Sci. U. S. A., vol. 107, pp.18392-18397, 2010.

[46] Chen, G.D., Fachin, F., Fernandez-Suarez, M., Wardle, B.L. and Toner, M. “Nanoporous elements in microfluidics for multiscale manipulation of bioparticles,” Small, vol. 7, pp.1061-1067, 2011.

[47] Antolovic, D., Galindo, L., Carstens, A., Rahbari, N., Büchler, M.W., Weitz, J. and Koch, M. “Heterogeneous detection of circulating tumor cells in patients with colorectal cancer by immunomagnetic enrichment using different EpCAM-specific antibodies,” BMC biotechnol., vol. 10, p.35, 2010.

[48] Cheng, S.B., Xie, M., Xu, J.Q., Wang, J., Lv, S.W., Guo, S., Shu, Y., Wang, M., Dong, W.G. and Huang, W.H. “High-efficiency capture of individual and cluster of circulating tumor cells by a microchip embedded with three-dimensional poly (dimethylsiloxane) scaffold,” Anal. Chem., vol. 88, pp.6773-6780, 2016.

[49] Jack, R., Hussain, K., Rodrigues, D., Zeinali, M., Azizi, E., Wicha, M., Simeone, D.M. and Nagrath, S. “Microfluidic continuum sorting of sub-populations of tumor cells via surface antibody expression levels,” Lab Chip, vol. 17, pp.1349-1358, 2017.

[50] Kasimir-Bauer, S., Hoffmann, O., Wallwiener, D., Kimmig, R. and Fehm, T. “Expression of stem cell and epithelial-mesenchymal transition markers in primary

breast cancer patients with circulating tumor cells," Breast Cancer Res., vol. 14, p.R15, 2012.

[51] Gorges, T.M., Tinhofer, I., Drosch, M., Röse, L., Zollner, T.M., Krahn, T. and von Ahsen, O. "Circulating tumour cells escape from EpCAM-based detection due to epithelial-to-mesenchymal transition," BMC Cancer, vol. 12, p.178, 2012.

[52] Cushing, K., Undvall, E., Ceder, Y., Lilja, H. and Laurell, T. "Reducing WBC background in cancer cell separation products by negative acoustic contrast particle immuno-acoustophoresis," Anal. Chim. Acta, vol. 1000, pp.256-264, 2018.

[53] Chu, P.Y., Hsieh, C.H. and Wu, M.H. "The combination of immunomagnetic bead-based cell isolation and optically induced dielectrophoresis (ODEP)-based microfluidic device for the negative selection-based isolation of circulating tumor cells (CTCs)," Front. Bioeng. Biotechnol., vol. 8, p.921, 2020.

[54] Karabacak, N.M., Spuhler, P.S., Fachin, F., Lim, E.J., Pai, V., Ozkumur, E., Martel, J.M., Kojic, N., Smith, K., Chen, P.I. and Yang, J. "Microfluidic, marker-free isolation of circulating tumor cells from blood samples," Nat. Protoc., vol. 9, pp.694-710, 2014.

[55] Gourikutty, S.B.N., Chang, C.P. and Puiu, P.D. "Microfluidic immunomagnetic cell separation from whole blood," J. Chromatogr. B, vol. 1011, pp.77-88, 2016.

[56] Jiang, J., Zhao, H., Shu, W., Tian, J., Huang, Y., Song, Y., Wang, R., Li, E., Slamon, D., Hou, D. and Du, X. "An integrated microfluidic device for rapid and high-sensitivity analysis of circulating tumor cells," Sci. Rep., 7, p.42612, 2017.

[57] Zhao, W., Liu, Y., Jenkins, B.D., Cheng, R., Harris, B.N., Zhang, W., Xie, J., Murrow, J.R., Hodgson, J., Egan, M. and Bankey, A. "Tumor antigen-independent and cell size variation-inclusive enrichment of viable circulating tumor cells," Lab Chip, vol. 19, pp.1860-1876, 2019.

[58] Hyun, K.A., Lee, T.Y. and Jung, H.I. "Negative enrichment of circulating tumor cells using a geometrically activated surface interaction chip," Anal. Chem., vol. 85, pp.4439-4445, 2013.

[59] Diéguez, L., Winter, M.A., Pocock, K.J., Bremmell, K.E. and Thierry, B., "Efficient microfluidic negative enrichment of circulating tumor cells in blood using roughened PDMS," Analyst, vol. 140, pp.3565-3572, 2015.

[60] Ferreira, M.M., Ramani, V.C. and Jeffrey, S.S. “Circulating tumor cell technologies,” Mol. Oncol., vol. 10, pp.374-394, 2016.

[61] Shaffer, D.R., Leversha, M.A., Danila, D.C., Lin, O., Gonzalez-Espinoza, R., Gu, B., Anand, A., Smith, K., Maslak, P., Doyle, G.V. and Terstappen, L.W. “Circulating tumor cell analysis in patients with progressive castration-resistant prostate cancer,” Clin. Cancer Res., vol. 13, pp.2023-2029, 2007.

[62] Maheswaran, S., Sequist, L.V., Nagrath, S., Ulkus, L., Brannigan, B., Collura, C.V., Inserra, E., Diederichs, S., Iafrate, A.J., Bell, D.W. and Digumarthy, S. “Detection of mutations in EGFR in circulating lung-cancer cells,” N. Engl. J. Med., vol. 359, pp.366-377, 2008.

[63] Pantel, K. and Alix-Panabières, C. “Circulating tumour cells in cancer patients: challenges and perspectives,” Trends Mol. Med., vol. 16, pp.398-406, 2010.

[64] Sawyers, C.L. “The cancer biomarker problem,” Nature, vol. 452, pp.548-552, 2008.

[65] Powell, A.A., Talasaz, A.H., Zhang, H., Coram, M.A., Reddy, A., Deng, G., Telli, M.L., Advani, R.H., Carlson, R.W., Mollick, J.A. and Sheth, S. “Single cell profiling of circulating tumor cells: transcriptional heterogeneity and diversity from breast cancer cell lines,” PloS One, vol. 7, p.e33788, 2012.

[66] Alix-Panabières, C. and Pantel, K. “Challenges in circulating tumour cell research” Nat. Rev. Cancer, vol. 14, pp.623-631, 2014.

[67] Pantel, K. and Alix-Panabières, C. “Circulating tumour cells in cancer patients: challenges and perspectives,” Trends Mol. Med., vol. 16, pp.398-406, 2010.

[68] Lucci, A., Hall, C.S., Lodhi, A.K., Bhattacharyya, A., Anderson, A.E., Xiao, L., Bedrosian, I., Kuerer, H.M. and Krishnamurthy, S. “Circulating tumour cells in non-metastatic breast cancer: a prospective study,” Lancet Oncol., vol. 13, pp.688-695, 2012.

[69] Nagrath, S., Sequist, L.V., Maheswaran, S., Bell, D.W., Irimia, D., Ulkus, L., Smith, M.R., Kwak, E.L., Digumarthy, S., Muzikansky, A. and Ryan, P. “Isolation of rare circulating tumour cells in cancer patients by microchip technology,” Nature, vol. 450, pp.1235-1239, 2007.

[70] Fawcett, D.W., Vallee, B.L. and Soule, M.H. “A method for concentration and segregation of malignant cells from bloody, pleural, and peritoneal fluids,” Science, vol. 111, pp.34-36, 1950.

[71] Seal, S.H. “Silicone flotation: A simple quantitative method for the isolation of free-floating cancer cells from the blood,” Cancer, vol. 12, pp.590-595, 1959.

[72] Yoo, C.E., Moon, H.S., Kim, Y.J., Park, J.M., Park, D., Han, K.Y., Park, K., Sun, J.M. and Park, W.Y. “Highly dense, optically inactive silica microbeads for the isolation and identification of circulating tumor cells,” Biomaterials, vol. 75, pp.271-278, 2016.

[73] Li, H., Meng, Q.H., Noh, H., Batth, I.S., Somaiah, N., Torres, K.E., Xia, X., Wang, R. and Li, S. “Detection of circulating tumor cells from cryopreserved human sarcoma peripheral blood mononuclear cells,” Cancer Lett., vol. 403, pp.216-223, 2017.

[74] Li, P., Stratton, Z.S., Dao, M., Ritz, J. and Huang, T.J. “Probing circulating tumor cells in microfluidics,” Lab Chip, vol. 13, pp.602-609, 2013.

[75] Jiang, J., Zhao, H., Shu, W., Tian, J., Huang, Y., Song, Y., Wang, R., Li, E., Slamon, D., Hou, D. and Du, X. “An integrated microfluidic device for rapid and high-sensitivity analysis of circulating tumor cells,” Sci. Rep., vol. 7, pp.1-11, 2017.

[76] Reece, A., Xia, B., Jiang, Z., Noren, B., McBride, R. and Oakey, J. “Microfluidic techniques for high throughput single cell analysis,” Curr. Opin. Biotechnol., vol. 40, pp.90-96, 2016.

[77] Lu, C., Xu, J., Han, J., Li, X., Xue, N., Li, J., Wu, W., Sun, X., Wang, Y., Ouyang, Q. and Yang, G. “A novel microfluidic device integrating focus-separation speed reduction design and trap arrays for high-throughput capture of circulating tumor cells,” Lab Chip, vol. 20, pp.4094-4105, 2020.

[78] Nasiri, R., Shamloo, A., Ahadian, S., Amirifar, L., Akbari, J., Goudie, M.J., Lee, K., Ashammakhi, N., Dokmeci, M.R., Di Carlo, D. and Khademhosseini, A. “Microfluidic-based approaches in targeted cell/particle separation based on physical properties: fundamentals and applications,” Small, vol. 16, p.2000171, 2020.

[79] Luo, L. and He, Y. “Magnetically driven microfluidics for isolation of circulating tumor cells,” Cancer Med., vol. 9, pp.4207-4231, 2020.

[80] Chelakkot, C., Ryu, J., Kim, M.Y., Kim, J.S., Kim, D., Hwang, J., Park, S.H., Ko, S.B., Park, J.W., Jung, M.Y. and Kim, R.N. “An Immune–Magnetophoretic Device for the Selective and Precise Enrichment of Circulating Tumor Cells from Whole Blood,” Micromachines, vol. 11, p.560, 2020.

[81] Zhu, L., Lin, H., Wan, S., Chen, X., Wu, L., Zhu, Z., Song, Y., Hu, B. and Yang, C. “Efficient isolation and phenotypic profiling of circulating hepatocellular carcinoma cells via a combinatorial-antibody-functionalized microfluidic synergetic-chip,” Anal. Chem., vol. 92, pp.15229-15235, 2020.

[82] Chen, K., Amontree, J., Varillas, J., Zhang, J., George, T.J. and Fan, Z.H. “Incorporation of lateral microfiltration with immunoaffinity for enhancing the capture efficiency of rare cells,” Sci. Rep., vol. 10, pp.1-12, 2020.

[83] Desitter, I., Guerrouahen, B.S., Benali-Furet, N., Wechsler, J., Jänne, P.A., Kuang, Y., Yanagita, M., Wang, L., Berkowitz, J.A., Distel, R.J. and Cayre, Y.E. “A new device for rapid isolation by size and characterization of rare circulating tumor cells,” Anticancer Res., vol. 31, pp.427-441, 2011.

[84] Freidin, M.B., Tay, A., Freydina, D.V., Chudasama, D., Nicholson, A.G., Rice, A., Anikin, V. and Lim, E. “An assessment of diagnostic performance of a filter-based antibody-independent peripheral blood circulating tumour cell capture paired with cytomorphologic criteria for the diagnosis of cancer,” Lung Cancer, vol. 85, pp.182-185, 2014.

[85] Adams, D.L., Zhu, P., Makarova, O.V., Martin, S.S., Charpentier, M., Chumsri, S., Li, S., Amstutz, P. and Tang, C.M. “The systematic study of circulating tumor cell isolation using lithographic microfilters,” RSC Adv., vol. 4, pp.4334-4342, 2014.

[86] Zheng, S., Lin, H., Liu, J.Q., Balic, M., Datar, R., Cote, R.J. and Tai, Y.C. “Membrane microfilter device for selective capture, electrolysis and genomic analysis of human circulating tumor cells,” J. Chromatogr. A, vol. 1162, pp.154-161, 2007.

[87] Lin, H.K., Zheng, S., Williams, A.J., Balic, M., Groshen, S., Scher, H.I., Fleisher, M., Stadler, W., Datar, R.H., Tai, Y.C. and Cote, R.J. “Portable filter-based microdevice for detection and characterization of circulating tumor cells,” Clin. Cancer Res., vol. 16, pp.5011-5018, 2010.

[88] Lu, B., Zheng, S., Quach, B.Q. and Tai, Y.C. “A study of the autofluorescence of parylene materials for μTAS applications,” Lab Chip, vol. 10, pp.1826-1834, 2010.

[89] Zhou, M.D., Hao, S., Williams, A.J., Harouaka, R.A., Schrand, B., Rawal, S., Ao, Z., Brenneman, R., Gilboa, E., Lu, B. and Wang, S. "Separable bilayer microfiltration device for viable label-free enrichment of circulating tumour cells," Sci. Rep., vol. 4, pp.1-11, 2014.

[90] Tan, S.J., Yobas, L., Lee, G.Y.H., Ong, C.N. and Lim, C.T. "Microdevice for the isolation and enumeration of cancer cells from blood," Biomed. Microdevices, vol. 11, pp.883-892, 2009.

[91] McDonald, J.C. and Whitesides, G.M. "Poly (dimethylsiloxane) as a material for fabricating microfluidic devices," Acc. Chem. Res., vol. 35, pp.491-499, 2002.

[92] Yoon, Y., Kim, S., Lee, J., Choi, J., Kim, R.K., Lee, S.J., Sul, O. and Lee, S.B. "Clogging-free microfluidics for continuous size-based separation of microparticles," Sci. Rep., vol. 6, pp.1-8, 2016.

[93] Ferreira, M.M., Ramani, V.C. and Jeffrey, S.S. "Circulating tumor cell technologies," Mol. Oncol., vol. 10, pp.374-394, 2016.

[94] Ozkumur, E., Shah, A.M., Ciciliano, J.C., Emmink, B.L., Miyamoto, D.T., Brachtel, E., Yu, M., Chen, P.I., Morgan, B., Trautwein, J. and Kimura, A. "Inertial focusing for tumor antigen–dependent and–independent sorting of rare circulating tumor cells," Sci. Transl. Med., vol. 5, pp.179ra47-179ra47, 2013.

[95] Hosic, S., Murthy, S.K. and Koppes, A.N. "Microfluidic sample preparation for single cell analysis," Anal. Chem., vol. 88, pp.354-380, 2016.

[96] Ji, H.M., Samper, V., Chen, Y., Heng, C.K., Lim, T.M. and Yobas, L. "Silicon-based microfilters for whole blood cell separation," Biomed. Microdevices, vol. 10, pp.251-257, 2008.

[97] Stone, H.A. and Kim, S. "Microfluidics: basic issues, applications, and challenges," AIChE J., vol. 47, pp.1250-1254, 2001.

[98] Holm, S.H., Beech, J.P., Barrett, M.P. and Tegenfeldt, J.O. "Separation of parasites from human blood using deterministic lateral displacement," Lab Chip, vol. 11, pp.1326-1332, 2011.

[99] Huang, L.R., Cox, E.C., Austin, R.H. and Sturm, J.C. “Continuous particle separation through deterministic lateral displacement,” Science, vol. 304, pp.987-990, 2004.

[100] Inglis, D.W., Davis, J.A., Austin, R.H. and Sturm, J.C. “Critical particle size for fractionation by deterministic lateral displacement,” Lab Chip, vol. 6, pp.655-658, 2006.

[101] Meng, S., Tripathy, D., Frenkel, E.P., Shete, S., Naftalis, E.Z., Huth, J.F., Beitsch, P.D., Leitch, M., Hoover, S., Euhus, D. and Haley, B. “Circulating tumor cells in patients with breast cancer dormancy,” Clin. Cancer Res., vol. 10, pp.8152-8162, 2004.

[102] Loutherback, K., D'Silva, J., Liu, L., Wu, A., Austin, R.H. and Sturm, J.C. “Deterministic separation of cancer cells from blood at 10 mL/min,” AIP Adv., vol. 2, p.042107, 2012.

[103] Davis, J.A., Inglis, D.W., Morton, K.J., Lawrence, D.A., Huang, L.R., Chou, S.Y., Sturm, J.C. and Austin, R.H. “Deterministic hydrodynamics: taking blood apart,” Proc. Natl. Acad. Sci. U. S. A., vol. 103, pp.14779-14784, 2006.

[104] Wunsch, B.H., Smith, J.T., Gifford, S.M., Wang, C., Brink, M., Bruce, R.L., Austin, R.H., Stolovitzky, G. and Astier, Y. “Nanoscale lateral displacement arrays for the separation of exosomes and colloids down to 20 nm,” Nat. Nanotechnol., vol. 11, pp.936-940, 2016.

[105] Loutherback, K., Chou, K.S., Newman, J., Puchalla, J., Austin, R.H. and Sturm, J.C. “Improved performance of deterministic lateral displacement arrays with triangular posts,” Microfluid. Nanofluidics, vol. 9, pp.1143-1149, 2010.

[106] Segre, G. and Silberberg, A. “Radial particle displacements in Poiseuille flow of suspensions,” Nature, vol. 189, pp.209-210, 1961.

[107] Segre, G. and Silberberg, A. “Behaviour of macroscopic rigid spheres in Poiseuille flow Part 2. Experimental results and interpretation,” J. Fluid Mech., vol. 14, pp.136-157, 1962.

[108] Karnis, A. Goldsmith, H.L. Mason, S.G. “The flow of suspensions through tubes: V. Inertial effects,” Can. J. Chem. Eng., vol. 44, pp.181-193, 1966.

[109] Tachibana, M. “On the behaviour of a sphere in the laminar tube flows,” Rheol. Acta, vol. 12, pp.58-69, 1973.

[110] Di Carlo, D., Irimia, D., Tompkins, R.G. and Toner, M. “Continuous inertial focusing, ordering, and separation of particles in microchannels,” Proc. Natl. Acad. Sci. U. S. A., vol. 104, pp.18892-18897, 2007.

[111] Lee, M.G., Choi, S. and Park, J.K. “Rapid multivortex mixing in an alternately formed contraction-expansion array microchannel,” Biomed. Microdevices, vol. 12, pp.1019-1026, 2010.

[112] Lee, M.G., Shin, J.H., Bae, C.Y., Choi, S. and Park, J.K. “Label-free cancer cell separation from human whole blood using inertial microfluidics at low shear stress,” Anal. Chem., vol. 85, pp.6213-6218, 2013.

[113] Di Carlo, D. “Inertial microfluidics,” Lab Chip, vol. 9, pp.3038-3046, 2009.

[114] Hur, S.C., Mach, A.J. and Di Carlo, D. “High-throughput size-based rare cell enrichment using microscale vortices,” Biomicrofluidics, vol. 5, p.022206, 2011.

[115] Sollier, E., Go, D.E., Che, J., Gossett, D.R., O'Byrne, S., Weaver, W.M., Kummer, N., Rettig, M., Goldman, J., Nickols, N. and McCloskey, S. “Size-selective collection of circulating tumor cells using Vortex technology,” Lab Chip, vol. 14, pp.63-77, 2014.

[116] Cherdron, W., Durst, F. and Whitelaw, J.H. “Asymmetric flows and instabilities in symmetric ducts with sudden expansions,” J. Fluid Mech., vol. 84, pp.13-31, 1978.

[117] Moffatt, H.K. “Viscous and resistive eddies near a sharp corner,” J. Fluid Mech., vol. 18, pp.1-18, 1964.

[118] Hur, S.C., Tse, H.T.K. and Di Carlo, D. “Sheathless inertial cell ordering for extreme throughput flow cytometry,” Lab Chip, vol. 10, pp.274-280, 2010.

[119] Vitha, M.F. “Circulating tumor cells: isolation and analysis,” John Wiley & Sons, 2016.

[120] Antfolk, M., Antfolk, C., Lilja, H., Laurell, T. and Augustsson, P. “A single inlet two-stage acoustophoresis chip enabling tumor cell enrichment from white blood cells,” Lab Chip, vol. 15, pp.2102-2109, 2015.

[121] Augustsson, P., Magnusson, C., Nordin, M., Lilja, H. and Laurell, T. “Microfluidic, label-free enrichment of prostate cancer cells in blood based on acoustophoresis,” Anal. Chem., vol. 84, pp.7954-7962, 2012.

[122] Ding, X., Peng, Z., Lin, S.C.S., Geri, M., Li, S., Li, P., Chen, Y., Dao, M., Suresh, S. and Huang, T.J. “Cell separation using tilted-angle standing surface acoustic waves,” Proc. Natl. Acad. Sci. U. S. A., vol. 111, pp.12992-12997, 2014.

[123] Li, P., Mao, Z., Peng, Z., Zhou, L., Chen, Y., Huang, P.H., Truica, C.I., Drabick, J.J., El-Deiry, W.S., Dao, M. and Suresh, S. “Acoustic separation of circulating tumor cells,” Proc. Natl. Acad. Sci. U. S. A., vol. 112, pp.4970-4975, 2015.

[124] Aceto, N., Bardia, A., Miyamoto, D.T., Donaldson, M.C., Wittner, B.S., Spencer, J.A., Yu, M., Pely, A., Engstrom, A., Zhu, H. and Brannigan, B.W. “Circulating tumor cell clusters are oligoclonal precursors of breast cancer metastasis,” Cell, vol. 158, pp.1110-1122, 2014.

[125] Watanabe, S. “The metastasizability of tumor cells,” Cancer, vol. 7, pp.215-223, 1954.

[126] Goto, W., Kashiwagi, S., Asano, Y., Takada, K., Takahashi, K., Hatano, T., Takashima, T., Tomita, S., Motomura, H., Ohsawa, M. and Hirakawa, K. “Circulating tumor cell clusters-associated gene plakoglobin is a significant prognostic predictor in patients with breast cancer,” Biomarker Res., vol. 5, pp.1-8, 2017.

[127] Hong, Y., Fang, F. and Zhang, Q. “Circulating tumor cell clusters: What we know and what we expect,” Int. J. Oncol., vol. 49, pp.2206-2216, 2016.

[128] Hou, S., Zhao, L., Shen, Q., Yu, J., Ng, C., Kong, X., Wu, D., Song, M., Shi, X., Xu, X. and OuYang, W.H. “Polymer nanofiber-embedded microchips for detection, isolation, and molecular analysis of single circulating melanoma cells,” Ange. Chem. Int. Ed., vol. 125, pp.3463-3467, 2013.

[129] Stott, S.L., Hsu, C.H., Tsukrov, D.I., Yu, M., Miyamoto, D.T., Waltman, B.A., Rothenberg, S.M., Shah, A.M., Smas, M.E., Korir, G.K. and Floyd, F.P. “Isolation

of circulating tumor cells using a microvortex-generating herringbone-chip," Proc. Natl. Acad. Sci. U. S. A., vol. 107, pp.18392-18397, 2010.

[130] Vona, G., Sabile, A., Louha, M., Sitruk, V., Romana, S., Schütze, K., Capron, F., Franco, D., Pazzagli, M., Vekemans, M. and Lacour, B. "Isolation by size of epithelial tumor cells: a new method for the immunomorphological and molecular characterization of circulating tumor cells," Am. J. Pathol., vol. 156, pp.57-63, 2000.

[131] Au, S.H., Storey, B.D., Moore, J.C., Tang, Q., Chen, Y.L., Javaid, S., Sarioglu, A.F., Sullivan, R., Madden, M.W., O'Keefe, R. and Haber, D.A. "Clusters of circulating tumor cells traverse capillary-sized vessels," Proc. Natl. Acad. Sci. U. S. A., vol. 113, pp.4947-4952, 2016.

[132] Au, S.H., Edd, J., Stoddard, A.E., Wong, K.H., Fachin, F., Maheswaran, S., Haber, D.A., Stott, S.L., Kapur, R. and Toner, M. "Microfluidic isolation of circulating tumor cell clusters by size and asymmetry," Sci. Rep., vol. 7, pp.1-10, 2017.

[133] Huang, L.R., Cox, E.C., Austin, R.H. and Sturm, J.C. "Continuous particle separation through deterministic lateral displacement," Science, vol. 304, pp.987-990, 2004.

[134] Inglis, D.W., Davis, J.A., Austin, R.H. and Sturm, J.C. "Critical particle size for fractionation by deterministic lateral displacement," Lab Chip, vol. 6, pp.655-658, 2006.

[135] Chandran, K.B., Rittgers, S.E. and Yoganathan, A.P. "Biofluid mechanics: the human circulation," CRC Press, 2006.

[136] Song, Y., Tian, T., Shi, Y., Liu, W., Zou, Y., Khajvand, T., Wang, S., Zhu, Z. and Yang, C. "Enrichment and single-cell analysis of circulating tumor cells," Chem. Sci., vol. 8, pp.1736-1751, 2017.

[137] Yu, M., Stott, S., Toner, M., Maheswaran, S. and Haber, D.A. "Circulating tumor cells: approaches to isolation and characterization," J. Cell Biol., vol. 192, pp.373-382, 2011.

[138] Hoshino, K., Huang, Y.Y., Lane, N., Huebschman, M., Uhr, J.W., Frenkel, E.P. and Zhang, X. "Microchip-based immunomagnetic detection of circulating tumor cells," Lab Chip, vol. 11, pp.3449-3457, 2011.

[139] Lee, H.J., Cho, H.Y., Oh, J.H., Namkoong, K., Lee, J.G., Park, J.M., Lee, S.S., Huh, N. and Choi, J.W. “Simultaneous capture and in situ analysis of circulating tumor cells using multiple hybrid nanoparticles,” Biosens. Bioelectron., vol. 47, pp.508-514, 2013.

[140] Went, P.T., Lugli, A., Meier, S., Bundi, M., Mirlacher, M., Sauter, G. and Dirnhofer, S. “Frequent EpCam protein expression in human carcinomas,” Hum. Pathol., vol.35, pp.122-128, 2004.

[141] Alix-Panabières, C. and Pantel, K. “Challenges in circulating tumour cell research,” Nat. Rev. Cancer, vol. 14, pp.623-631, 2014.

[142] Pantel, K., Brakenhoff, R.H. and Brandt, B. “Detection, clinical relevance and specific biological properties of disseminating tumour cells,” Nat. Rev. Cancer, vol. 8, pp.329-340, 2008.

[143] Saliba, A.E., Saias, L., Psychari, E., Minc, N., Simon, D., Bidard, F.C., Mathiot, C., Pierga, J.Y., Fraisier, V., Salamero, J. and Saada, V. “Microfluidic sorting and multimodal typing of cancer cells in self-assembled magnetic arrays,” Proc. Natl. Acad. Sci. U. S. A., vol. 107, pp.14524-14529, 2010.

[144] Allan, A.L. and Keeney, M. “Circulating tumor cell analysis: technical and statistical considerations for application to the clinic,” J. Oncol., vol. 2010, p.426218, 2010.

[145] Stott, S.L., Hsu, C.H., Tsukrov, D.I., Yu, M., Miyamoto, D.T., Waltman, B.A., Rothenberg, S.M., Shah, A.M., Smas, M.E., Korir, G.K. and Floyd, F.P. “Isolation of circulating tumor cells using a microvortex-generating herringbone-chip,” Proc. Natl. Acad. Sci. U. S. A., vol. 107, pp.18392-18397, 2010.

[146] Talasaz, A.H., Powell, A.A., Huber, D.E., Berbee, J.G., Roh, K.H., Yu, W., Xiao, W., Davis, M.M., Pease, R.F., Mindrinos, M.N. and Jeffrey, S.S. “Isolating highly enriched populations of circulating epithelial cells and other rare cells from blood using a magnetic sweeper device,” Proc. Natl. Acad. Sci. U. S. A., vol. 106, pp.3970-3975, 2009.

[147] Giordano, A., Gao, H., Anfossi, S., Cohen, E., Mego, M., Lee, B.N., Tin, S., De Laurentiis, M., Parker, C.A., Alvarez, R.H. and Valero, V. “Epithelial–mesenchymal transition and stem cell markers in patients with HER2-positive metastatic breast cancer,” Mol. Cancer Ther., vol. 11, pp.2526-2534, 2012.

[148] Lara, O., Tong, X., Zborowski, M. and Chalmers, J.J. “Enrichment of rare cancer cells through depletion of normal cells using density and flow-through, immunomagnetic cell separation,” Exp. Hematol, vol. 32, pp.891-904, 2004.

[149] Pantel, K., Brakenhoff, R.H. and Brandt, B. “Detection, clinical relevance and specific biological properties of disseminating tumour cells,” Nat. Rev. Cancer, vol. 8, pp.329-340, 2008.

[150] Riethdorf, S., Fritsche, H., Müller, V., Rau, T., Schindlbeck, C., Rack, B., Janni, W., Coith, C., Beck, K., Jänicke, F. and Jackson, S. “Detection of circulating tumor cells in peripheral blood of patients with metastatic breast cancer: a validation study of the CellSearch system,” Clin. Cancer Res., vol. 13, pp.920-928, 2007.

[151] Alix-Panabières, C. and Pantel, K. “Circulating tumor cells: liquid biopsy of cancer,” Clin. Chem., vol. 59, pp.110-118, 2013.

[152] Miltenyi, S., Müller, W., Weichel, W. and Radbruch, A. “High gradient magnetic cell separation with MACS,” Cytometry Part A, vol. 11, pp.231-238, 1990.

[153] Neurauter, A.A., Bonyhadi, M., Lien, E., Nøkleby, L., Ruud, E., Camacho, S. and Aarvak, T. “Cell isolation and expansion using Dynabeads®,” Cell Separation, pp.41-73, 2007.

[154] Lin, H., Balic, M., Zheng, S., Datar, R. and Cote, R.J. “Disseminated and circulating tumor cells: role in effective cancer management,” Crit. Rev. Oncol Hematol, vol. 77, pp.1-11, 2011.

[155] Nagrath, S., Sequist, L.V., Maheswaran, S., Bell, D.W., Irimia, D., Ulkus, L., Smith, M.R., Kwak, E.L., Digumarthy, S., Muzikansky, A. and Ryan, P. “Isolation of rare circulating tumour cells in cancer patients by microchip technology,” Nature, vol. 450, pp.1235-1239, 2007.

[156] Chen, G.D., Fachin, F., Fernandez-Suarez, M., Wardle, B.L. and Toner, M. “Nanoporous elements in microfluidics for multiscale manipulation of bioparticles,” Small, vol. 7, pp.1061-1067, 2011.

[157] Choi, H., Kim, K.B., Jeon, C.S., Hwang, I., Lee, S., Kim, H.K., Kim, H.C. and Chung, T.D. “A label-free DC impedance-based microcytometer for circulating rare cancer cell counting,” Lab Chip, vol. 13, pp.970-977, 2013.

[158] Davies, J., Dawkes, A.C., Haymes, A.G., Roberts, C.J., Sunderland, R.F., Wilkins, M.J., Davies, M.C., Tendler, S.J.B., Jackson, D.E. and Edwards, J.C. "A scanning tunneling microscopy comparison of passive antibody adsorption and biotinylated antibody linkage to streptavidin on microtiter wells," J. Immunolog. Meth, vol. 167, pp.263-269, 1994.

[159] Harb, W., Fan, A., Tran, T., Danila, D.C., Keys, D., Schwartz, M. and Ionescu-Zanetti, C. "Mutational analysis of circulating tumor cells using a novel microfluidic collection device and qPCR assay," Transl. Oncol, vol. 6, pp.528-IN1, 2013.

[160] Hughes, A.D. and King, M.R. "Use of naturally occurring halloysite nanotubes for enhanced capture of flowing cells," Langmuir, vol. 26, pp.12155-12164, 2010.

[161] Kim, Y.J., Koo, G.B., Lee, J.Y., Moon, H.S., Kim, D.G., Lee, D.G., Lee, J.Y., Oh, J.H., Park, J.M., Kim, M.S. and Woo, H.G. "A microchip filter device incorporating slit arrays and 3-D flow for detection of circulating tumor cells using CAV1-EpCAM conjugated microbeads," Biomaterials, vol. 35, pp.7501-7510, 2014.

[162] Lu, J., Fan, T., Zhao, Q., Zeng, W., Zaslavsky, E., Chen, J.J., Frohman, M.A., Golightly, M.G., Madajewicz, S. and Chen, W.T. "Isolation of circulating epithelial and tumor progenitor cells with an invasive phenotype from breast cancer patients," Int. J. Cancer, vol. 126, pp.669-683, 2010.

[163] Mittal, S., Wong, I.Y., Deen, W.M. and Toner, M. "Antibody-functionalized fluid-permeable surfaces for rolling cell capture at high flow rates," Biophys. J., vol. 102, pp.721-730, 2012.

[164] Ozkumur, E., Shah, A.M., Ciciliano, J.C., Emmink, B.L., Miyamoto, D.T., Brachtel, E., Yu, M., Chen, P.I., Morgan, B., Trautwein, J. and Kimura, A. "Inertial focusing for tumor antigen–dependent and–independent sorting of rare circulating tumor cells," Sci. Transl. Med., vol. 5, pp.179ra47-179ra47, 2013.

[165] Wang, S., Wang, H., Jiao, J., Chen, K.J., Owens, G.E., Kamei, K.I., Sun, J., Sherman, D.J., Behrenbruch, C.P., Wu, H. and Tseng, H.R. "Three-dimensional nanostructured substrates toward efficient capture of circulating tumor cells," Angew. Chem. Int. Ed., vol. 48, pp.8970-8973, 2009.

[166] Wang, S., Liu, K., Liu, J., Yu, Z.T.F., Xu, X., Zhao, L., Lee, T., Lee, E.K., Reiss, J., Lee, Y.K. and Chung, L.W. "Highly efficient capture of circulating tumor cells by using nanostructured silicon substrates with integrated chaotic micromixers," Angew. Chem. Int. Ed., vol. 123, pp.3140-3144, 2011.

[167] Stroock, A.D., Dertinger, S.K., Ajdari, A., Mezić, I., Stone, H.A. and Whitesides, G.M. “Chaotic mixer for microchannels,” Science, vol. 295, pp.647-651, 2002.

[168] Lu, Y.T., Zhao, L., Shen, Q., Garcia, M.A., Wu, D., Hou, S., Song, M., Xu, X., OuYang, W.H., OuYang, W.W.L. and Lichterman, J. “NanoVelcro Chip for CTC enumeration in prostate cancer patients,” Nat. Methods, vol. 64, pp.144-152, 2013.

[169] Adams, A.A., Okagbare, P.I., Feng, J., Hupert, M.L., Patterson, D., Göttert, J., McCarley, R.L., Nikitopoulos, D., Murphy, M.C. and Soper, S.A. “Highly efficient circulating tumor cell isolation from whole blood and label-free enumeration using polymer-based microfluidics with an integrated conductivity sensor,” J. Am. Chem, Soc., vol. 130, pp.8633-8641, 2008.

[170] Cheng, S.B., Xie, M., Xu, J.Q., Wang, J., Lv, S.W., Guo, S., Shu, Y., Wang, M., Dong, W.G. and Huang, W.H. “High-efficiency capture of individual and cluster of circulating tumor cells by a microchip embedded with three-dimensional poly (dimethylsiloxane) scaffold,” Anal. Chem., vol. 88, pp.6773-6780, 2016.

[171] Besant, J.D., Mohamadi, R.M., Aldridge, P.M., Li, Y., Sargent, E.H. and Kelley, S.O. “Velocity valleys enable efficient capture and spatial sorting of nanoparticle-bound cancer cells,” Nanoscale, vol. 7, pp.6278-6285, 2015.

[172] Jackson, J.M., Witek, M.A., Kamande, J.W. and Soper, S.A. “Materials and microfluidics: enabling the efficient isolation and analysis of circulating tumour cells,” Chem. Soc. Rev., vol. 46, pp.4245-4280, 2017.

[173] Phillips, J.A., Xu, Y., Xia, Z., Fan, Z.H. and Tan, W. “Enrichment of cancer cells using aptamers immobilized on a microfluidic channel,” Anal. Chem., vol. 81, pp.1033-1039, 2009.

[174] Zhou, J. and Rossi, J.J. “Cell-type-specific, aptamer-functionalized agents for targeted disease therapy,” Mol. Ther. Nucleic Acids, vol. 3, p.e169, 2014.

[175] Sun, H., Zhu, X., Lu, P.Y., Rosato, R.R., Tan, W. and Zu, Y. “Oligonucleotide aptamers: new tools for targeted cancer therapy,” Mol. Ther. Nucleic Acids, vol. 3, p.e182, 2014.

[176] Tuerk, C. and Gold, L. “Systematic evolution of ligands by exponential enrichment: RNA ligands to bacteriophage T4 DNA polymerase,” Science, vol. 249, pp.505-510, 1990.

[177] Zamay, G.S., Kolovskaya, O.S., Zamay, T.N., Glazyrin, Y.E., Krat, A.V., Zubkova, O., Spivak, E., Wehbe, M., Gargaun, A., Muharemagic, D. and Komarova, M. “Aptamers selected to postoperative lung adenocarcinoma detect circulating tumor cells in human blood,” Mol. Ther., vol. 23, pp.1486-1496, 2015.

[178] Bruno, J.G. “Predicting the uncertain future of aptamer-based diagnostics and therapeutics,” Molecules, vol. 20, pp.6866-6887, 2015.

[179] Bunka, D.H. and Stockley, P.G. “Aptamers come of age–at last,” Nature Rev. Microbiol., vol. 4, pp.588-596, 2006.

[180] Dickey, D.D. and Giangrande, P.H. “Oligonucleotide aptamers: A next-generation technology for the capture and detection of circulating tumor cells,” Nat. Methods, vol. 97, pp.94-103, 2016.

[181] Farokhzad, O.C., Jon, S., Khademhosseini, A., Tran, T.N.T., LaVan, D.A. and Langer, R. “Nanoparticle-aptamer bioconjugates: a new approach for targeting prostate cancer cells,” Cancer Res., vol. 64, pp.7668-7672, 2004.

[182] Song, K.M., Lee, S. and Ban, C. “Aptamers and their biological applications,” Sensors, vol. 12, pp.612-631, 2012.

[183] Dharmasiri, U., Balamurugan, S., Adams, A.A., Okagbare, P.I., Obubuafo, A. and Soper, S.A. “Highly efficient capture and enumeration of low abundance prostate cancer cells using prostate-specific membrane antigen aptamers immobilized to a polymeric microfluidic device,” Electrophoresis, vol. 30, pp.3289-3300, 2009.

[184] Qian, W., Zhang, Y. and Chen, W. “Capturing cancer: emerging microfluidic technologies for the capture and characterization of circulating tumor cells,” Small, vol. 11, pp.3850-3872, 2015.

[185] Poudineh, M., Labib, M., Ahmed, S., Nguyen, L.M., Kermanshah, L., Mohamadi, R.M., Sargent, E.H. and Kelley, S.O. “Profiling functional and biochemical phenotypes of circulating tumor cells using a two-dimensional sorting device,” Angew. Chem. Int. Ed., vol. 56, pp.163-168, 2017.

[186] Shen, Q., Xu, L., Zhao, L., Wu, D., Fan, Y., Zhou, Y., OuYang, W.H., Xu, X., Zhang, Z., Song, M. and Lee, T. “Specific capture and release of circulating tumor cells using aptamer-modified nanosubstrates,” Adv. Mater., vol. 25, pp.2368-2373, 2013.

[187] Ma, H., Liu, J., Ali, M.M., Mahmood, M.A.I., Labanieh, L., Lu, M., Iqbal, S.M., Zhang, Q., Zhao, W. and Wan, Y. “Nucleic acid aptamers in cancer research, diagnosis and therapy,” Chem. Soc. Rev., vol. 44, pp.1240-1256, 2015.

[188] Zhao, Y., Xu, D. and Tan, W. “Aptamer-functionalized nano/micro-materials for clinical diagnosis: isolation, release and bioanalysis of circulating tumor cells,” Integr. Biol., vol. 9, pp.188-205, 2017.

[189] Liu, G., Mao, X., Phillips, J.A., Xu, H., Tan, W. and Zeng, L. “Aptamer−nanoparticle strip biosensor for sensitive detection of cancer cells,” Anal. Chem., vol. 81, pp.10013-10018, 2009.

[190] Viraka Nellore, B.P., Kanchanapally, R., Pramanik, A., Sinha, S.S., Chavva, S.R., Hamme, A. and Ray, P.C. “Aptamer-conjugated graphene oxide membranes for highly efficient capture and accurate identification of multiple types of circulating tumor cells,” Bioconjug. Chem., vol. 26, pp.235-242, 2015.

[191] Myung, J.H. and Hong, S. “Microfluidic devices to enrich and isolate circulating tumor cells,” Lab Chip, vol. 15, pp.4500-4511, 2015.

[192] Phillips, J.A., Xu, Y., Xia, Z., Fan, Z.H. and Tan, W. “Enrichment of cancer cells using aptamers immobilized on a microfluidic channel,” Anal. Chem., vol. 81, pp.1033-1039, 2009.

[193] Xu, Y., Phillips, J.A., Yan, J., Li, Q., Fan, Z.H. and Tan, W. “Aptamer-based microfluidic device for enrichment, sorting, and detection of multiple cancer cells,” Anal. Chem., vol. 81, pp.7436-7442, 2009.

[194] Zhao, W., Ali, M.M., Brook, M.A. and Li, Y. “Rolling circle amplification: applications in nanotechnology and biodetection with functional nucleic acids,” Angew. Chem. Int. Ed., vol. 47, pp.6330-6337, 2008.

[195] Zhao, W., Cui, C.H., Bose, S., Guo, D., Shen, C., Wong, W.P., Halvorsen, K., Farokhzad, O.C., Teo, G.S.L., Phillips, J.A. and Dorfman, D.M. “Bioinspired multivalent DNA network for capture and release of cells,” Proc. Natl. Acad. Sci. U. S. A., vol. 109, pp.19626-19631, 2012.

[196] Sheng, W., Chen, T., Kamath, R., Xiong, X., Tan, W. and Fan, Z.H. “Aptamer-enabled efficient isolation of cancer cells from whole blood using a microfluidic device,” Anal Chem., vol. 84, pp.4199-4206, 2012.

[197] Wan, Y., Liu, Y., Allen, P.B., Asghar, W., Mahmood, M.A.I., Tan, J., Duhon, H., Kim, Y.T., Ellington, A.D. and Iqbal, S.M. “Capture, isolation and release of cancer cells with aptamer-functionalized glass bead array,” Lab Chip, vol. 12, pp.4693-4701, 2012.

[198] Wang, L., Zheng, Q., Zhang, Q.A., Xu, H., Tong, J., Zhu, C. and Wan, Y. “Detection of single tumor cell resistance with aptamer biochip,” Oncol. Lett., vol. 4, pp.935-940, 2012.

[199] Sheng, W., Chen, T., Kamath, R., Xiong, X., Tan, W. and Fan, Z.H. “Aptamer-enabled efficient isolation of cancer cells from whole blood using a microfluidic device,” Anal. Chem., vol. 84, pp.4199-4206, 2012.

[200] Zhao, L., Tang, C., Xu, L., Zhang, Z., Li, X., Hu, H., Cheng, S., Zhou, W., Huang, M., Fong, A. and Liu, B. “Enhanced and differential capture of circulating tumor cells from lung cancer patients by microfluidic assays using aptamer cocktail,” Small, vol. 12, pp.1072-1081, 2016.

[201] Labib, M., Green, B., Mohamadi, R.M., Mepham, A., Ahmed, S.U., Mahmoudian, L., Chang, I.H., Sargent, E.H. and Kelley, S.O. “Aptamer and antisense-mediated two-dimensional isolation of specific cancer cell subpopulations,” J. Am. Chem. Soc., vol. 138, pp.2476-2479, 2016.

[202] Ozkumur, E., Shah, A.M., Ciciliano, J.C., Emmink, B.L., Miyamoto, D.T., Brachtel, E., Yu, M., Chen, P.I., Morgan, B., Trautwein, J. and Kimura, A. “Inertial focusing for tumor antigen–dependent and–independent sorting of rare circulating tumor cells,” Sci. Transl. Med., vol. 5, pp.179ra47-179ra47, 2013.

[203] Karabacak, N.M., Spuhler, P.S., Fachin, F., Lim, E.J., Pai, V., Ozkumur, E., Martel, J.M., Kojic, N., Smith, K., Chen, P.I. and Yang, J. “Microfluidic, marker-free isolation of circulating tumor cells from blood samples,” Nat. Protoc., vol. 9, pp.694-710, 2014.

[204] Park, J.M., Lee, J.Y., Lee, J.G., Jeong, H., Oh, J.M., Kim, Y.J., Park, D., Kim, M.S., Lee, H.J., Oh, J.H. and Lee, S.S. “Highly efficient assay of circulating tumor cells by selective sedimentation with a density gradient medium and microfiltration from whole blood,” Anal. Chem., vol. 84, pp.7400-7407, 2012.

[205] Waheed, S., Cabot, J.M., Macdonald, N.P., Lewis, T., Guijt, R.M., Paull, B. and Breadmore, M.C. “3D printed microfluidic devices: enablers and barriers,” Lab Chip, vol. 16, pp.1993-2013, 2016.

[206] Waldbaur, A., Rapp, H., Länge, K. and Rapp, B.E. “Let there be chip—towards rapid prototyping of microfluidic devices: one-step manufacturing processes,” Anal. Methods, vol. 3, pp.2681-2716, 2011.

[207] Melchels, F.P., Feijen, J. and Grijpma, D.W. “A review on stereolithography and its applications in biomedical engineering,” Biomaterials, vol. 31, pp.6121-6130, 2010.

[208] Yin, P., Hu, B., Yi, L., Xiao, C., Cao, X., Zhao, L. and Shi, H. “Engineering of removing sacrificial materials in 3D-printed microfluidics,” Micromachines, vol. 9, p.327, 2018.

[209] Shallan, A.I., Smejkal, P., Corban, M., Guijt, R.M. and Breadmore, M.C. “Cost-effective three-dimensional printing of visibly transparent microchips within minutes,” Anal. Chem., vol. 86, pp.3124-3130, 2014.

[210] Castiaux, A.D., Pinger, C.W., Hayter, E.A., Bunn, M.E., Martin, R.S. and Spence, D.M. “PolyJet 3D-printed enclosed microfluidic channels without photocurable supports,” Anal. Chem., vol. 91, pp.6910-6917, 2019.

[211] Gonzalez, G., Chiappone, A., Dietliker, K., Pirri, C.F. and Roppolo, I. “Fabrication and Functionalization of 3D Printed Polydimethylsiloxane-Based Microfluidic Devices Obtained through Digital Light Processing,” Adv. Mater. Technol., vol. 5, p.2000374, 2020.

[212] Nielsen, A.V., Beauchamp, M.J., Nordin, G.P. and Woolley, A.T. “3D printed microfluidics,” Annu. Rev., 13, pp.45-65, 2020.

[213] Raoufi, M.A., Bazaz, S.R., Niazmand, H., Rouhi, O., Asadnia, M., Razmjou, A. and Warkiani, M.E. “Fabrication of unconventional inertial microfluidic channels using wax 3D printing,” Soft Matter, vol. 16, pp.2448-2459, 2020.

[214] Ching, T., Toh, Y.C. and Hashimoto, M. “Fabrication of complex 3D fluidic networks via modularized stereolithography,” Adv. Eng. Mater., vol. 22, p.1901109, 2020.

[215] Carrell, C.S., McCord, C.P., Wydallis, R.M. and Henry, C.S. “Sealing 3D-printed parts to poly (dimethylsiloxane) for simple fabrication of microfluidic devices,” Anal. Chim. Acta, 1124, pp.78-84, 2020.

[216] Zeraatkar, M., Filippini, D. and Percoco, G. “On the impact of the fabrication method on the performance of 3D printed mixers,” Micromachines, vol. 10, p.298, 2019.

[217] Bonyár, A., Sántha, H., Ring, B., Varga, M., Kovács, J.G. and Harsányi, G. “3D Rapid Prototyping Technology (RPT) as a powerful tool in microfluidic development,” Procedia Eng., vol. 5, pp.291-294, 2010.

[218] Comina, G., Suska, A. and Filippini, D. “Low cost lab-on-a-chip prototyping with a consumer grade 3D printer,” Lab Chip, vol. 14, pp.2978-2982, 2014.

[219] Moore, J.L., McCuiston, A., Mittendorf, I., Ottway, R. and Johnson, R.D. “Behavior of capillary valves in centrifugal microfluidic devices prepared by three-dimensional printing,” Microfluid. Nanofluidics, vol. 10, pp.877-888, 2011.

[220] Jones, A.M. and Knudsen, J.G. “Drag coefficients at low Reynolds numbers for flow past immersed bodies,” AIChE J., vol. 7, pp.20-25, 1961.

[221] Wong, C.C., Agarwal, A., Balasubramanian, N. and Kwong, D.L. “Fabrication of self-sealed circular nano/microfluidic channels in glass substrates,” Nanotechnology, vol. 18, p.135304, 2007.

[222] Gonzalez, G., Chiappone, A., Dietliker, K., Pirri, C.F. and Roppolo, I. “Fabrication and functionalization of 3D printed polydimethylsiloxane-based microfluidic devices obtained through digital light processing,” Adv. Mater. Technol., vol. 5, p.2000374, 2020.

[223] Wang, H., Chakraborty, A. and Luo, C. “Fabrication of Au micropatterns on vertical Si sidewalls using flexible PDMS shadow masks,” J. Micromech. Microeng., vol. 20, p.127001, 2010.

[224] Yong, J., Yang, Q., Chen, F., Zhang, D., Du, G., Si, J., Yun, F. and Hou, X. “A bioinspired planar superhydrophobic microboat,” J. Micromech. Microeng., vol. 24, p.035006, 2014.

[225] Diéguez, L., Winter, M.A., Pocock, K.J., Bremmell, K.E. and Thierry, B. “Efficient microfluidic negative enrichment of circulating tumor cells in blood using roughened PDMS,” Analyst, vol. 140, pp.3565-3572, 2015.

[226] Stott, S.L., Hsu, C.H., Tsukrov, D.I., Yu, M., Miyamoto, D.T., Waltman, B.A., Rothenberg, S.M., Shah, A.M., Smas, M.E., Korir, G.K. and Floyd, F.P. "Isolation of circulating tumor cells using a microvortex-generating herringbone-chip," Proc. Natl. Acad. Sci. U. S. A., vol. 107, pp.18392-18397, 2010.

[227] Meunier, A., Hernández-Castro, J.A., Turner, K., Li, K., Veres, T. and Juncker, D. "Combination of mechanical and molecular filtration for enhanced enrichment of circulating tumor cell," Anal. Chem., vol. 88, pp.8510-8517, 2016.

[228] Miyamoto, D.T., Lee, R.J., Stott, S.L., Ting, D.T., Wittner, B.S., Ulman, M., Smas, M.E., Lord, J.B., Brannigan, B.W., Trautwein, J. and Bander, N.H. "Androgen receptor signaling in circulating tumor cells as a marker of hormonally responsive prostate cancer," Cancer Discov., vol. 2, pp.995-1003, 2012.

[229] Renier, C., Pao, E., Che, J., Liu, H.E., Lemaire, C.A., Matsumoto, M., Triboulet, M., Srivinas, S., Jeffrey, S.S., Rettig, M. and Kulkarni, R.P. "Label-free isolation of prostate circulating tumor cells using Vortex microfluidic technology," NPJ Precis. Oncol., vol. 1, pp.1-11, 2017.

[230] Fachin, F., Spuhler, P., Martel-Foley, J.M., Edd, J.F., Barber, T.A., Walsh, J., Karabacak, M., Pai, V., Yu, M., Smith, K. and Hwang, H. "Monolithic chip for high-throughput blood cell depletion to sort rare circulating tumor cells," Sci. Rep., vol. 7, pp.1-11, 2017.

[231] Khoja, L., Backen, A., Sloane, R., Menasce, L., Ryder, D., Krebs, M., Board, R., Clack, G., Hughes, A., Blackhall, F. and Valle, J.W. "A pilot study to explore circulating tumour cells in pancreatic cancer as a novel biomarker," Br. J. Cancer, vol. 106, pp.508-516, 2012.

[232] Kamande, J.W., Hupert, M.L., Witek, M.A., Wang, H., Torphy, R.J., Dharmasiri, U., Njoroge, S.K., Jackson, J.M., Aufforth, R.D., Snavely, A. and Yeh, J.J. "Modular microsystem for the isolation, enumeration, and phenotyping of circulating tumor cells in patients with pancreatic cancer," Anal. Chem., vol. 85, pp.9092-9100, 2013.

[233] Varillas, J.I., Zhang, J., Chen, K., Barnes, I.I., Liu, C., George, T.J. and Fan, Z.H. "Microfluidic isolation of circulating tumor cells and cancer stem-like cells from patients with pancreatic ductal adenocarcinoma," Theranostics, vol. 9, p.1417, 2019.

[234] Cheung, K.J., Padmanaban, V., Silvestri, V., Schipper, K., Cohen, J.D., Fairchild, A.N., Gorin, M.A., Verdone, J.E., Pienta, K.J., Bader, J.S. and Ewald, A.J. "Polyclonal breast cancer metastases arise from collective dissemination of keratin

14-expressing tumor cell clusters," Proc. Natl. Acad. Sci. U. S. A., vol. 113, pp.E854-E863, 2016.

[235] Aceto, N., Bardia, A., Miyamoto, D.T., Donaldson, M.C., Wittner, B.S., Spencer, J.A., Yu, M., Pely, A., Engstrom, A., Zhu, H. and Brannigan, B.W. "Circulating tumor cell clusters are oligoclonal precursors of breast cancer metastasis," Cell, vol. 158, pp.1110-1122, 2014.